Inaugural dissertation

for

obtaining the doctoral degree

of the

Combined Faculty of Mathematics, Engineering and Natural Sciences

of the

Ruprecht – Karls – University

Heidelberg

Presented by
M. Sc. Alexandra Zakieva
born in Moscow, Russia
Oral examination: 8th July 2022

Quantitative analysis of plant radial growth in *Arabidopsis thaliana*

Referees:
Prof. Dr. Thomas Greb
Prof. Dr. Alexis Maizel

Abstract [German]

Höhere Pflanzen sind vielzellige Organismen, die den größten Teil der weltweiten Biomasse produzieren. Diese Produktion ist hauptsächlich auf das radiale Wachstum von Bäumen zurückzuführen - ein Prozess, der durch die Aktivität der Kambium-Stammzellen in den Stämmen angetrieben wird. Während des radialen Wachstums produziert das Kambium zwei Gefäßgewebe: Xylem und Phloem. In der Modellpflanze Arabidopsis thaliana werden innerhalb weniger Wochen Tausende von Zellen vom Kambium gebildet. Während der Zellproliferation, -expansion und -differenzierung nehmen die Zellen eine spezifische Morphologie an und formen so die Gefäßgewebe. Die Zell- und Gewebemorphogenese kann durch molekulare Signalübertragung und mechanische Stimuli reguliert werden. Die Zellwände spielen die Rolle einer Schnittstelle für diese mechanischen Reize sowie einer extrazellulären Matrix und eines Skeletts für die gesamte Pflanze. Ziel der aktuellen Studie ist es, die Zell- und Gewebemorphogenese zu quantifizieren und zu verstehen, wie sie durch verschiedene Faktoren der Pflanzenentwicklung beeinflusst wird. Die Rolle der Zellwand wurde mit Hilfe der induzierbaren gewebespezifischen Expression von zellwandbezogenen Genen untersucht. Die Zell- und Gewebemorphogenese wurde mit Hilfe eines quantitativen Histologieprotokolls analysiert, das in dieser Studie entwickelt wurde. Dieses Protokoll wurde an zwei verschiedenen Allelen von mit Xylem interkalierten Phloemmutanten (pxy) getestet. Das radiale Wachstum wurde beeinflusst von der Kambium- und Xylem-spezifische ektopische Expression der Zellwand-bezogenen Gene HAESA-INFLORESCENCE DEFICIENT IN ABCISSION, die für ein Rezeptor-Ligand-Modul kodieren, und VANGUARD 1, das für eine Pektin-Methylesterase kodiert. Quantitative histologische Untersuchungen ergaben bisher unbekannte Eigenschaften der Morphogenese des Gefäßgewebes und subtile Unterschiede zwischen den pxy-Allelen. Die Studie hat gezeigt, dass die Zellwand eine Schlüsselrolle bei der Morphogenese von Pflanzen während des Radialwachstums spielt, wie dies bereits bei anderen Pflanzenorganen gezeigt wurde. Die quantitative Histologie ist ein leistungsfähiges Instrument zur Phänotypisierung, das die Gewebetopologie als wichtigen Faktor in der Morphogenese aufzeigt. Es wurde eine mechanistische Theorie vorgestellt, wie PXY die Muster von Gefäßgeweben regulieren könnte. Insgesamt können die Erkenntnisse über das Radialwachstum in der Land- und Forstwirtschaft genutzt werden, um die Gefahren für die gesamte Menschheit, wie z. B. Nahrungsmittelknappheit oder Klimakrise, zu mindern.

Abstract (English)

Higher plants are multicellular organisms that produce the major volume of the world biomass. This production is mostly due to radial growth in trees – a process driven by cambium stem cell activity in trunks. During radial growth, cambium produces two vascular tissues: xylem and phloem. In Arabidopsis thaliana, the model plant species, thousands of cells are produced by cambium just in a couple of weeks. During cell proliferation, expansion and differentiation, cells acquire specific morphologies shaping thus vascular tissues. Cell and tissue morphogenesis can be regulated by molecular signalling and mechanical stimuli. Cell walls play the role of an interface for these mechanical stimuli, as well as an extracellular matrix and a skeleton for the whole plant. The current study aims to quantify cell and tissue morphogenesis and to understand how it is influenced by different factors of plant development. The role of the cell wall was tested with the help of inducible tissue-specific expression of cell wall-related genes. Cell and tissue morphogenesis was analysed by a quantitative histology protocol that was established in this study. This protocol was tested on two different alleles of phloem intercalated with xylem (pxy) mutants. Radial growth was affected by the cambium and xylem-specific ectopic expression of cell wall-related genes HAESA-INFLORESCENCE DEFICIENT IN ABCISSION coding for a receptor-ligand module and VANGUARD 1 coding for a pectin-methyl esterase. Quantitative histology revealed previously unseen properties of vascular tissue morphogenesis and subtle differences between pxy alleles. The study demonstrated that the cell wall is a key player in plant morphogenesis during radial growth, as it was previously shown in other plant organs. Quantitative histology is a powerful phenotyping tool that revealed tissue topology as an important factor in morphogenesis. A mechanistic theory on how PXY could regulate vascular tissues patterning was presented. Overall, the knowledge on radial growth can be used in agronomic and forestry applications to mitigate the dangers of the whole humanity like food shortages or climate crisis.

Key words

Plant biology, vasculature, stem cells, genetic engineering, machine learning

Acknowledgements

First of all, I would like to thank Thomas Greb for giving me such an amazing opportunity to do my Ph. D. in his research group on such an outstanding topic. Thomas always believed in me and my project despite scientific or personal challenges that I faces during last years. My thanks go to my Thesis Advisory Committee as well. Angela Hay always brought a positive vision into my project even during the lowest moments of it. Alexis Maizel taught me the culture of constant and constructive dought that pushed me outside of my comfort zone.

I was lucky to be part of FOR2581 “Plant Morphodynamics” consortium that broadened my curiosity horizons with its interdisciplinary approach making a smooth marriage of biology, physics and computer sciences. I am particularly grateful to Lorenzo Cerrone, a Ph. D. candidate supervised by Fred Hamprecht, who went through the most challenging and unpredictable parts of my work together with me: the images segmentation. Soeren Strauss, a post-doctoral fellow supervised by Richard Smith and then by Miltos Tsiantis, was of equal help and patience in helping me with morphometric analysis of my images. It was especially satisfying to see my fellow Ph. D. candidates of the consortium to develop into accomplished scientists during the funding period of our projects by FOR2581. The end of my Ph. D. period was funded by ERC H2020 which I am equally grateful for. I would like to thank HBIGS team and Graduate Academy for helping me to navigate through my Ph. D. curriculum.

I was lucky to realise my Ph. D. in Centre for Organismal Studies of Heidelberg University. This vibrant environment of constant scientific, cultural and social exchange supported me through thick and thin moments of my Ph. D. life. I am extremely grateful to the technological sharing within our community. The group of Annika Guse shared their confocal microscope with me to acquire the high quality images, so critical for quantitative histology. The group of Joachim Wittbrodt was also helpful to provide their vibratome for me. The group of Steffen Lemcke was patient to share precious laboratory space with me for working with this machine, while Steffen himself honoured me with examining my thesis and defense. The group of Jan Lohmann shared laboratory space and technical expertise with me and my colleagues before our group moved to the new building. The group of Alexis Maizel were always available to discuss plant science and share new ideas together, while Alexis himself kindly agreed to examine my doctoral thesis and defense. I was equally honoured to be examined by Karin Schumacher, our institute colleague as well as vice-rector of our University. I was happy to rely on our technical departments like the cleaning of the laboratory equipment, the workshop for the customed tools, the IT service – all these people working in the background helped me to forget about the basic needs of academic work and focus only on the scientific research. The

rest of our institute was always inspirational for me at our seminars, lectures, science communication and social events. Thank you!

My Ph. D. would have never been accomplished without my wonderful colleagues. Christina Godel and Angelika Wunderlich were so helpful in navigating in administrative documentation – an environment so alien to me because of the cultural and language barriers. Our technician Ilona Jung always provided me with a sense of security for our biological samples and chemical preparations, so I could focus better on my research. Our highly skilled post-doctoral fellows guided me through complicated research work: Jian Qi with her impeccable discipline, Vadir Lopez with his radical relativity views, Dongbo Shi with his metascale scientific vision, Theresa Schlamp with her optimistic stoicism, Pascal Hunziker with his interdisciplinary expertise and imagination for “cell roads” term, Hyunwoo Cho with his ambitious curiousity, Virginie Jouannet with her selfless perfectionnism, Sophie Wallner with her pragmatic efficiency, Nina Tonn always caring for the well-being of Ph. D. students, Ivan Lebovka with his interdisciplinary vision, Daria Navrotska with her bravery to study non-mainstream plant species, Changzheng Song with his focused goals, Yingqiang Xu with his ironic attitude towards scientific careers, Steffen Greiner with his absolute support of students. I would like to thank all these post-doctoral researchers for their courage to continue teaching Ph. D. students despite the challenging career paths that they chose. My doctoral studies were also enlightened by my fellow Ph. D. students who worked and studied with me in AG Greb: Jiaxin Zhong always supportive and protective of me, Aylin Haas with unbreakable critical spirit, Jiao Zhao with her expertise in multitasking, Kiara Kaeufer with her admirable leadership skills, Laura Luzzietti with her patience in the research of challenging topics, Xiaomin Liu with her unyielding strive for discovery, Min-Hao Chiang with his pragmatism. Thank you all for being beside me during all these years.

I was happy to discover other social activities in our University like representation of doctoral candidates. I was glad to represent Ph. D. students for half of a mandate in COS together with Zoe and Natalia. We went through difficult times together and managed to keep the internal communications alive despite the coronavirus pandemic. I am also grateful to my fellow doctoral candidates from the Executive Committee and the Working Group “Events and Workshops” of Doctoral Convention where I could represent for one mandate each. Together with you, we managed to organise so many events, help doctoral candidates in protecting their rights and take a wider look on academia, its beautiful and difficult sides. These activities held me through the lowest periods of my Ph. D. and inspired me for a political career.

This latest inspiration would not have been possible without my fellow activists of Russian, Belarusian, Kazahkstanian and Ukrainian Resistance against despotism. We all went and are still going through such tragic historical times that often affected my work, my life and my soul. Nevertheless

our common unity in this fight and hope for a brighter future helped me to carry out my personal and social goals to their fruition. Thank you!

My 10-years long studies in biology would have never been accomplished without my family and friends. I would like to give special thanks to my father Almaz and my aunt Nailya for being absolutely supportive of me despite anything, my friends Myriam, Marc and Zoe for helping me to forget sometimes work and life hurdles and to my boyfriend Alex for being with me through the hardest moments of my life and inspiring me with our philosophical discussions.

«Podrán cortar todas las flores, pero no podrán detener la primavera», Pablo Neruda

Table of contents

Abbreviations

2D – two-dimensional

3D – three-dimensional

ACT2 – ACTIN 2

APL – ALTERED PHLOEM DEVELOPMENT

BC – betweenness centrality

CLE41 – CLAVATA3/ESR-RELATED 41

CMTs – cortical microtubules

CNN – Convolutional Neural Networks

CSC – cellulose synthase complex

Dex – dexamethasone

DMSO – dimethyl sulfoxide

DNA – deoxyribonucleic acid

EDTA – Ethylenediamine tetraacetic acid

ER – ERECTA

EtBr – ethidium bromide

EtOH – ethanol

GR – glucocorticoid receptor

HAE – HAESA

HSL – HAESA-LIKE

IDA – INFLORESCENCE DEFICIENT IN ABSCISSION

KOR1 – KORRIGAN 1

LD – long day

LM – low melting temperature

LRP – lateral root primordium

LRR – Leucine-Rich-Repeats

MGX – MorphoGraphX

MS – Murashige and Skoog medium

MES – 4-Morpholineethansulfonic acid

NaCl – sodium chloride

NST3 – NAC SECONDARY WALL THICKENING PROMOTING 3

PBS – Phosphate-buffered saline

PCR – polymerase chain reaction

PFA – paraformaldehyde

PI – propidium iodide

PME – pectin methyl-esterase

PMEI – PME inhibitor

PXY – PHLOEM INTERCALATED WITH XYLEM

RLK – Receptor-like kinase

SAM – shoot apical meristem

SMXL5 – *SMAX1-LIKE 5*

SD – short day

SDS – sodium dodecyl sulfate

SERK – SOMATIC EMRYOGENESIS RECEPTOR-LIKE KINASE 1

SVM – Support Vector Machine

TAE – Tris acetic acid

TrisHCl – (hydroxymethyl) aminomethane (THAM) hydrochloride

VGD1 – VANGUARD 1

VND7 – VASCULAR RELATED NAC-DOMAIN PROTEIN 7

WOX4 – WUSCHEL-RELATED HOMEOBOX

wpg – weeks post-germination

WT – wild type

Introduction

Multicellular organisms have a hierarchical organisation where cells compose tissues, tissues compose organs and organs compose the whole organism. Contrary to unicellular species, multicellular ones have to fine-tune the development of every single cell, so it fulfils its role without compromising the functionality of the whole organism [1]. For example, in human body, a dysfunctionality of a tissue can lead to drastic consequences like paralysis or tumour [2]. These are examples of cell death or cell proliferation that cause a dysfunctionality of the whole organism. To avoid such defects, multicellular organisms developed a non-hierarchal signalling network between cells, tissues and different parts of the body. This means that a single molecule produced by one tissue can have a dramatic effect on the whole organism. For example, this is the case of insulin that regulates the sugar level in human body and assures its survival [3].

The multicellular organisms develop within the limits of their environment. For this, species build adaptive strategies driven by the natural selection. Higher plants are sessile organisms meaning that they cannot escape non-favourable environment. Plants have to build efficient defence strategies without compromising their survival or reproduction. For example, they keep toxic compounds in the vacuole organoids to release it on an eventual herbivore that destroys these cells [4]. It is fascinating how plants can use the challenges imposed to them by the environment for transforming their own development.

This is the case for trees that developed radial growth and wood production during evolution to grow taller and get more sunlight for photosynthesis. Thickening of stems and their transformation into trunks during a tree development allows the plant to mechanically support the tree crown. Radial growth was an evolutionary invention in seed plants. It was preserved in dicotyledonous species like trees or cacti but lost in monocotyledonous species like grasses [5]. Most of species lacking radial growth do not grow as tall as trees suggesting that radial growth provides an efficient vertical support to resist gravity.

During radial growth, vascular tissues are produced allowing transport of molecules throughout the whole organism. This growth is due to stem cell activity of cambium. The cambium is a bifacial plant meristem producing xylem in one direction and phloem in the other direction [6]. The resulting tissues morphology vary across species and provide them with special advantages [7]. For example, sequoias develop larger xylem that is efficient to keep a heavy body straight over the ground, while lianas develop multiple phloem fibers that serve them as “plant muscles” to climb other trees [8]. Sequoias and lianas can produce both xylem and phloem fibers but the balance between their productions is different comparing the two species. Radial growth is generally tightly regulated on the

level of tissue production to fulfil the needs of an organism in its development and adaptation to the environment.

Plant cell and tissue morphogenesis is a hierarchal and yet flexible process

The adjustment of the size and shape of a cell, tissue, organ or the whole organism during development is called morphogenesis. Contrary to animals, plant cells do not move. Therefore, their proliferation, expansion and differentiation directly impact the morphogenesis of a tissue that they compose. Tissue reshaping impacts the morphogenesis of the organ that this tissue is part of and affects the morphogenesis of the whole organism if one follows the hierarchal structure described above. Therefore, a plant can be viewed as a complex system where cells are the individual agents composing it and directly influencing the morphogenesis of the whole organism by their individual actions [9]. This angle inspired researchers for computational modelling of plant development with cells acting as basic elements.

Computational models help to visualise the effect of the action of combined agents on the complex system which is difficult to grasp with human mind [10]. For example, a computational model testing different mechanisms of cell division suggests that cell divisions according to the shortest path principle take place in SAM [11]. Other models estimate cell growth and how it contributes to tissue morphogenesis [12]. Cell division, growth and differentiation are three main steps of the cell cycle. These can be all visualised in the context of a stem cell niche like cambium [13]. Lebovka et al. developped a computational model questioning how molecular signalling regulating vascular tissues is integrated into tissue morphogenesis [14].

The main network regulating cambium stem cell niche consists of hormones, mobile peptides, receptors and transcription factors. *WUSCHEL-RELATED HOMEOBOX* (*WOX4*) encodes a transcription factor in cambium that activates its proliferation. *WOX4* expression is promoted by a receptor PHLOEM INTERCALATED WITH XYLEM (PXY) leucin-rich repeats (LRR)-Receptor-like kinase (RLK) that is located at the plasma membrane and activated by a small peptide CLAVATA3/ESR-RELATED 41 (CLE41) [15]. Interestingly PXY together with ERECTA (ER) regulate vascular tissues patterning [16]. *pxy* loss-of-function mutants presented a fragmented xylem and cambium. *PXY* is expressed in cambium while *CLE41* is expressed in phloem. CLE41 peptide travels to cambium to activate PXY [17]. This is a perfect example showing how molecules produced by neighbouring tissues can mutually affect their morphogenesis.

Cell, tissue and organ morphogenesis are also related to the function that these structures fulfil in an organism. For example, the role of leaf epidermal cells is to maximise the capture of sunlight.

Therefore, cell division in leaves is rarer than in cambium and the leaf morphogenesis is secured by cell anisotropic expansion and inhibition of this expansion in leaf indentations [18]. In the context of vascular tissues and radial growth, there is an extensive cell proliferation on cambium level, cell expansion and differentiation in xylem and phloem. The combination of all the steps of the cell cycle in one organ secures not only radial growth but also the transport role that vasculature fulfils for the whole organism [19].

Another factor that affects cell and tissue morphogenesis is mechanical signalling. It can originate from external source like the wind blowing against trees and inducing the production of the reaction wood [20]. The mechanical signalling can also come from within an organism. It is usually of two types of nature: cell turgor pressure or cell wall rigidity. The cell wall's biochemical composition and structure defines its mechanical properties. Previous studies showed that these properties vary between different cell types in neighbouring tissues depending on if cells divide, elongate or differentiate [9].

Cell wall is a multitask plant structure

Cell wall is plant extracellular matrix. Contrary to animals, it surrounds every single cell in plants, glues all the cells together in a connected network throughout the whole plant body. Cell wall is a barrier between cells maintaining their individuality [21]. But another peculiarity of plant cells is their interconnection via plasmodesmata. These are microscopic pores that allow transport of some molecules between neighbouring cells. This perforation is even more pronounced in xylem vessels and phloem sieve elements. In their final differentiation stage, these cells undergo a programmed cell death and serve as transport channels for respectively water and photosynthates. At this stage, xylem vessels and phloem sieve elements become only scaffolds of perforated cell walls almost without any cell content within [22] [23].

Another difference from animals, is that plants do not possess any specialised organs serving them as a skeleton. The combination of all cell walls mechanically supports the plant. This mechanical property results from biochemical composition of cell walls.

Cellulose is the main component which is a semi-rigid structure of cellulose microfibrils that are synthesized by Cellulose Synthase Complexes (CSCs) positioned on cortical microtubules (CMTs) just underneath the plasma membrane. Cellulose is rigid enough to resist to the turgor pressure of the cell, but also flexible to allow cell growth. Cellulose mechanical properties are defined by the orientation of microfibrils. When this orientation is random, the cell wall is softer. When cellulose microfibrils align in one direction, the cell wall becomes more resistant to the perpendicular direction of

mechanical stress. A polarised distribution of randomly aligned microfibrils on one side of a cell and of aligned microfibrils on another side of the cell results in anisotropic cell growth. For example, in young *Arabidopsis* hypocotyl, cells grow longitudinally. This is due to cellulose microfibrils aligned longitudinally in the side cell walls and non-aligned cellulose microfibrils in transversal cell walls. This way, cells grow in the longitudinal direction contributing to hypocotyl elongation and the maintenance of its cylindric shape [24]. Cellulose microfibrils are interconnected by hemi-cellulose polymers. Hemi-cellulose can be regulated by expansins that loosen the cell wall. For example, EXPANSIN A1 regulates lateral root emergence by modifying pericycle cell walls [25].

Another component of the cell wall is pectin which is a polymer of homogalacturonan. Pectin is synthesized within the cell and transported to the cell wall via Golgi secretory pathway. Once in the cell wall, pectin scaffolds are integrated between cellulose microfibrils reinforcing the whole structure. Pectin can form a large diversity of branching structures, as well as undergo chemical modifications. For example, pectin methyl-esterases (PMEs) demethylesterify pectin. This can lead to a loss of pectin protection against polygalacturonases that digest pectin leading to a subsequent loosening of the cell wall. The other possibility is that calcium bonds are formed between branches of demethylesterified pectin resulting in an “egg-box” structure that increases the stiffness of the cell wall. This ambivalence of the pectin degree of methylesterification was demonstrated in two different tissues. In the shoot apical meristem (SAM), at the emerging primordia sites, pectin is demethylesterified which leads to a loosening of cell walls and subsequent expansion of cells. However, when pectin is demethylesterified at the sides of a pollen tube, it rigidifies the cell wall and allows the growth of the pollen tube tip [26]. PMEs activity is influenced by the presence of PME inhibitors (PMEIs). PMEs are also part of a large family of enzymes having different activity depending on the pH [27]. All these factors make the research on pectin challenging. However, some PMEs stand out with a major cell wall modifying potency. This is the case of VANGUARD 1 (VGD1). When it was ubiquitously expressed in *Arabidopsis*, plants were rigid and had a stunt growth. It becomes interesting then to investigate VGD1 further. Other pectin modifications exist and were previously reviewed [27].

Lignin is another key component of the cell wall in land plants. Lignin is an evolutionary invention that allowed plants to colonise earth by providing rigidity to the cell wall. Secreted in the secondary cell wall, it forms a rigid structure. Once a cell is lignified, it cannot grow anymore and reaches its final stage of differentiation [28]. Lignified xylem and phloem provide the rigidity to the tree trunks allowing to carry this huge amount of biomass tall over the ground.

The secondary cell wall has a different proportion of the components described above [28]. The main property of the secondary cell wall is its lignification. But in some cells, additional layers of crystalline cellulose are added. This is the case of the reaction wood appearing after bending of tree

trunks. Xylem and phloem fibers synthesise several layers of crystalline cellulose interspersed by layers of lignin. This structure provides a muscle function to resist bending and eventually grow in the opposite direction [29]. In *Arabidopsis* hypocotyl, phloem fibers also exist but rarely studied.

Sometimes, plants need to disrupt a cell wall at a single cell resolution. For example, after flowers are pollinated, sepals and petals detach. When seeds come to maturation, silique valves open and the seeds are released on the ground. When lateral root emerges from the main root, endodermis, cortex and epidermis open letting the new root grow through them. In all these processes a specific molecular signalling is involved. A small 9.8 kDa INFLORESCENCE DEFICIENT IN ABSCISSION (IDA) peptide is produced by neighbouring tissues and recognised by HAESA (HAE) receptor. Next, HAE activates a MAP kinases cascade that on its turn activates the expression of cell wall loosening genes. Among them are polygalacturonases that depolymerise pectin [30].

Cell wall biochemical composition and structure shows a huge diversity across tissues and species. This extracellular matrix can be regulated by molecular signalling in a very subtle manner. Cell wall biochemical changes lead to the changes in its mechanical properties which in its turn, send mechanical feedback to the cell, the whole tissue or to the neighbouring tissues. This feedback is worth investigating in the context of morphogenesis.

Cambium stem cell niche as a model to study plant morphogenesis

In this thesis, I studied the cell and tissue morphogenesis in the context of radial growth of *Arabidopsis thaliana* – a model plant with easy genetics where radial growth occurs. As a model organ I use the hypocotyl which is at the intersection between shoots and roots and undergoes radial growth exclusively at the adult stage. In the hypocotyl, cambium produces xylem towards inside and phloem towards outside [31]. In young plants, vascular tissues are surrounded by the endodermis, cortex and epidermis, but these tissues disappear in adult plants and are replaced by the periderm – the most outer layer of the hypocotyl (Figure 1A) [32]. As the hypocotyl grows exclusively radially in adult plants, transversal sections are sufficient to visualize its anatomy in a first approximation. Thus, the *Arabidopsis* hypocotyl is a perfect model to investigate plant morphogenesis in two dimensions.

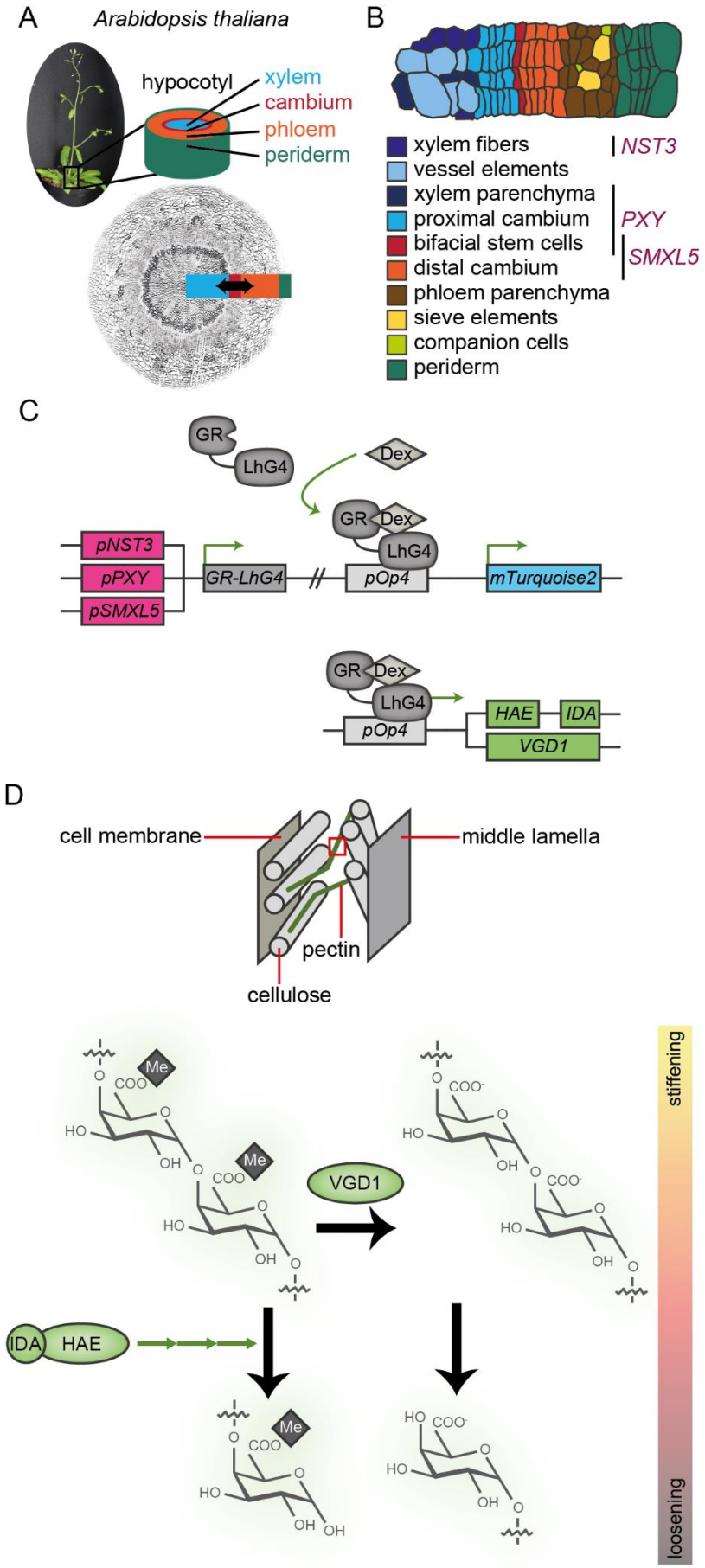
A
Arabidopsis thaliana
hypocotyl
xylem
cambium
phloem
periderm
B
xylem fibers
vessel elements
xylem parenchyma
proximal cambium
bifacial stem cells
distal cambium
phloem parenchyma
sieve elements
companion cells
periderm
NST3
PXY
SMXL5
C
GR
LhG4
Dex
pNST3
pPXY
pSMXL5
GR-LhG4
pOp4
mTurquoise2
HAE
IDA
VGD1
D
cell membrane
middle lamella
pectin
cellulose
Me
COO
HO
OH
VGD1
IDA
HAE
stiffening
loosening

Figure 1. Radial growth and genetic tools to modify cell wall mechanical properties in hypocotyl tissues. A. Radial growth and hypocotyl tissues. On the bottom, a hypocotyl transversal section stained with DirectRed23. The double-arrow represents cambium bifacial stem cell activity. **B.** A more detailed view on hypocotyl tissues. On the right, expression zone of vascular genes. **C.** Dexamethasone inducible system. Promoters used for driver constructs are in pink. Coding sequences for cell wall modifying proteins used for effector constructs are in green. Drivers are used as WT-like controls in induction experiments. Driver and effector plants are crossed between each other to generate a plant line to investigate. **D.** Cell wall modifying proteins effect on the cell wall. HAE-IDA has a cell wall loosening effect. VGD1 decreases the degree of methylesterification (Me) of pectin and has a cell wall stiffening or loosening effect.

However how plant cell walls affect vascular tissue morphogenesis is still unknown. In my project, I investigate this aspect. In the first part of my thesis, I address the following question:

How do cell wall mechanical properties regulate hypocotyl morphogenesis?

I used a dexamethasone (Dex) inducible system to ectopically express cell wall-related genes in a tissue-specific and timely-resolved manner (Figure 1C) [33]. I chose three drivers whose expression was shown to be specific to vascular tissues: *pNST3>>* (*NAC SECONDARY WALL THICKENING PROMOTING 3*), *pPXY>>* and *pSMXL5>>* (*SMAX1-LIKE 5*) (Figure 1B). *NST3* is specific to xylem fibers but is also expressed in xylem parenchyma cells that are on a way of differentiation into xylem fibers. *PXY* is specific to proximal cambium in stems and to xylem parenchyma together with proximal cambium in hypocotyls. *SMXL5* is specific to distal cambium and developing phloem. The overlap of *PXY* and *SMXL5* expression zones corresponds to cambium bifacial stem cells [34]. I aim to choose cell wall modifying proteins as effectors to loosen the cell wall or to stiffen it. For this, I use previously discovered molecular cascades regulating pectin – one of cell wall components defining its mechanical properties (Figure 1D). I chose HAE-IDA and VGD1 as the main cell modifying effectors as they appeared the most promising candidates for an ectopic cell wall modification (Figure 1C). PME3, PME5, PMEI3 and PMEI5 were used as cell wall modifying tools in previous studies, so I tried them as potential effectors in the context of hypocotyl tissues too.

Complex tissues require a quantitative analysis of every single cell

While investigating morphogenesis, one should consider how to quantify cell and tissue shapes. Novel computational methods have recently been developed to realize this quantification on microscopy images. These methods allow an automated segmentation of tissues into single cells and a quantification of their morphological descriptors [35].

But the segmentation becomes challenging for noisy confocal images. When a computational process fulfils a task less successfully than a human expert, machine learning algorithms can come in hand. Machine learning consists in improving automated processes by training a machine model by a

human expert. This way, the model takes into account not only absolute values but also the image interpretations of a human specialist. Machines identify gradients of intensities better than humans, while humans identify shapes better than machines. Therefore, the combination of both "expertises" substantially improves image segmentations [36]. Convolutional Neural Networks (CNNs) are used in the context of deep learning – one of the advanced methods of machine learning. The difference between CNNs deep learning algorithm and traditional machine learning algorithms like Random Forest or Support Vector Machine (SVM), is that the training parameters are not adjustable in the case of CNNs. The hyperparameter space is still accessible to the user but the detailed functioning of CNNs becomes like a "black box". CNNs were recently used on 3D confocal images of *Arabidopsis* SAM, lateral root primordia (LRP) and ovules with stained cell walls. By providing ground truths (segmentations corrected by a human expert) to a boundary prediction model, improved segmentations of these organs were obtained. The trained models were also published in a user-friendly interface "PlantSeg". After boundary prediction with trained CNNs, PlantSeg supports different graph partitioning algorithms like Watershed, MultiCut or MutexWS. These algorithms transform a pixelized boundary prediction map into a superpixelled segmentation where every superpixel corresponds to a label or a cell [37]. Hypocotyl sections were always the most challenging samples to segment and previous studies were usually limited to xylem tissues or cumbersome manual cell boundary annotation [38]. PlantSeg is a promising tool for segmentation of noisy confocal images of hypocotyl sections.

The next step of image analysis is to analyse every single cell of the acquired segmentation. A couple of publicly available computational tools were developed for this purpose like CellSeT [39] or MorphoGraphX (MGX) [35]. I opted for using MGX because it offers an SVM-based cell type classification and the widest range of cell descriptors – the quantitative fluorescent signal, morphometric and topological measures. Moreover, MGX was previously used for SAM, LRP, ovules and young hypocotyl [40].

The image analysis comprising cell segmentation of an image of an organ, extraction of cell descriptors and cell type classification was recently called "quantitative histology" [41]. Quantitative histology previously revealed that ovule development is uniform within the same pistil, that there are asymmetric cell divisions in LRP, that *bce* mutant shows an increased cell volume in SAM compared to WT [37]. Vascular tissues of hypocotyl haven't been thoroughly investigated yet in a similar way, nor has it been carried out in different genotypes. In the second part of my thesis, I address the following question:

How to establish a quantitative histology protocol with modern computational tools?

I used “PlantSeg” for cell segmentation and MGX for the analysis of cell and tissue morphological, cell wall composition and topological properties. MGX transforms a super-pixeled image obtained from PlantSeg to a vectorised image and extracts cell and tissue descriptors in a quantitative manner. MGX also provides heatmaps to visualise the distribution of these descriptors over hypocotyl tissues. Together with these novel tools as well as traditional image and data analysis programs like FIJI and R, I analysed hypocotyl sections with a quantitative histology protocol (Figure 2).

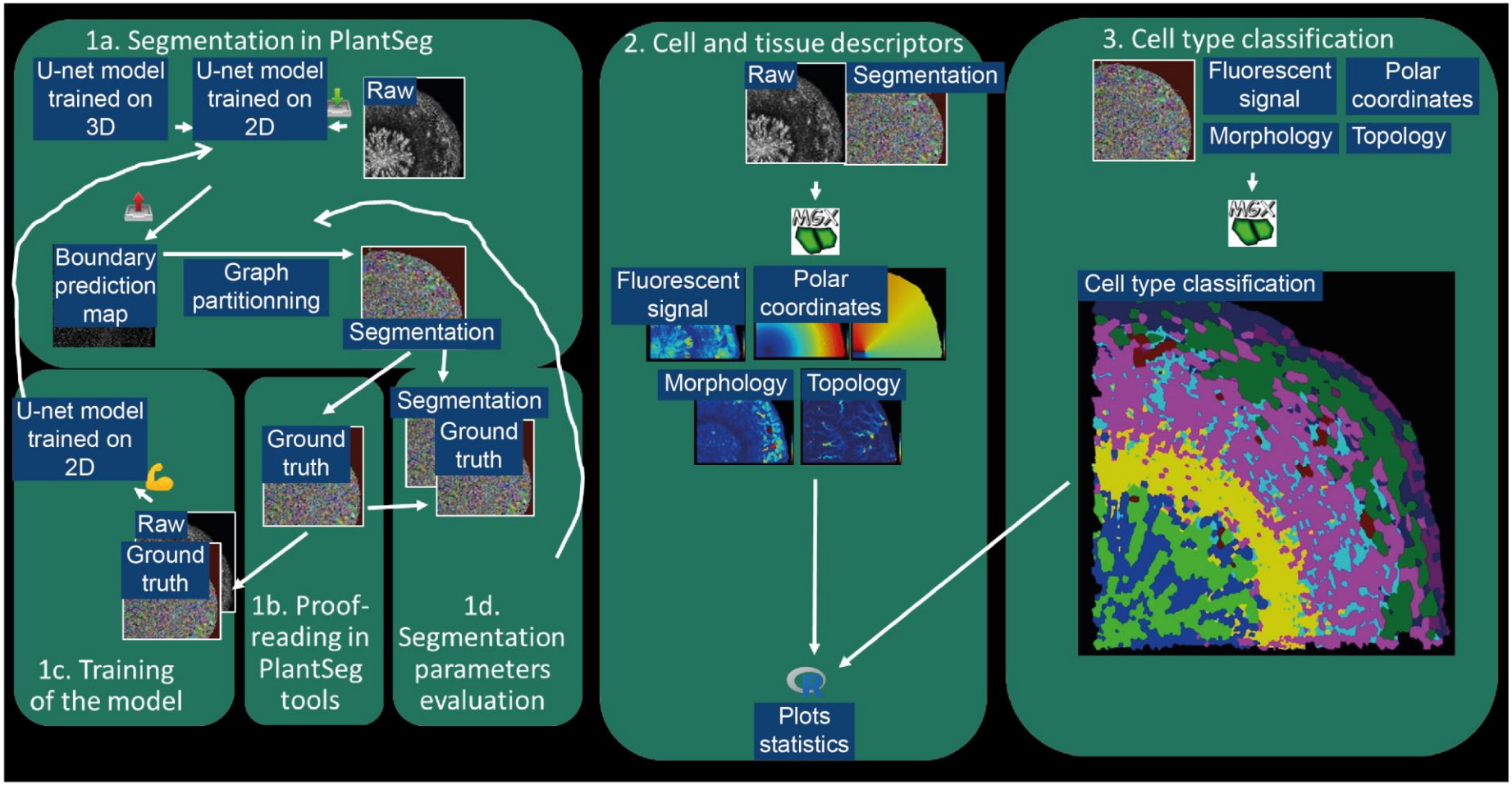

Figure 2. <u>Quantitative histology protocol</u>. The first part of this image analysis consists in cell segmentation. A CNN U-net boundary prediction model trained on three-dimensional confocal images of ovules and shoot apical meristem was adapted to two-dimensional images. A confocal image with cell boundary fluorescent staining was submitted to U-net 2D to generate a boundary prediction map. After graph partitionning, a segmentation is generated (**1a**). It is then proofread to get a ground truth (**1b**) that serves for the training of the model (**1c**) and segmentation parameters evaluation (**1d**). The second part consists in extracting cell descriptors for quantitative analysis (**2**). The third part is cell type classification based on the information acquired in the previous steps. Cell types serve for the quantitative analysis too (**3**).

PXY regulates vascular tissues patterning

Hypocotyl tissues present a more or less stereotypical patterning. Across radial axis, xylem takes the shape of a central disk surrounded by cambium, phloem and periderm in a shape of subsequent rings [15]. Such a clear stereotypical organisation is disrupted in vascular mutants. PXY-CLE41 receptor-ligand module regulates cambium meristematic activity and vascular tissues patterning. When *CLE41* is misexpressed in xylem, hypocotyl radial symmetry is disrupted: vascular tissues are not organised in concentric rings but in randomly distributed patches. When *PXY* is lost, xylem and cambium are circumferentially fragmented [42]. *PXY* role in radial patterning of hypocotyl tissues was therefore understood and even computationally modelled [14], but how *PXY* regulates circumferential patterning of hypocotyl tissues is still mechanistically unknown.

To shed light on this mystery and test the performance of the quantitative histology, three genotypes (WT, *pxy-2* and *pxy-4*) were analysed at four developmental stages. In the third part of my thesis, I addressed the question:

What are the dynamics of cell and tissue morphogenesis during radial growth?

pxy-2 and *pxy-4* previously showed to have a gradation of phenotype in the stem but until now, they were not compared quantitatively at hypocotyl level. I chose these two mutation alleles because the T-DNA insertion in *pxy-2* mutant disrupted only the intracellular kinase domain of PXY receptor leaving the extracellular LRR domain intact. While the T-DNA insertion in *pxy-4* mutant disrupted the LRR domain too [43]. Therefore, I expect to visualise a phenotype resulting from a non-functional but still receptive PXY in *pxy-2* mutant and a phenotype resulting from a non-functional and non-receptive PXY in *pxy-4*. I also analysed plants at four developmental stages covering radial growth. This way, I could learn not only the power of the quantitative histology to distinguish fine differences between mutant alleles but also the dynamics of radial growth and hypocotyl tissues ontology.

The three questions addressed above were challenged with experiments and computational analysis. In the following Material and Methods section, I described the biological material and the tools used in this study. The results are presented in the order of questions in the Results section followed by Discussion and Conclusion.

Materials and Methods

Plant material

Arabidopsis thaliana of Columbia-0 ecotype was used throughout this whole study. *pxy-2* (SALK_108191) and *pxy-4* (SALK_009542) T-DNA insertion lines were provided by Nottingham Arabidopsis Stock Centre.

Dex-inducible driver *pNST3::LhG4-GR;pOp4::mTurquoise2*, *pPXY::LhG4-GR;pOp4::mTurquoise2*, *pSMXL5::LhG4-GR;pOp4::mTurquoise2* and effector *pOp4::HAE;pOp4::IDA*, lines were developed previously and available in the hosting research group (Table 1). *pOp4::PME3*, *pOp4::PME5*, *pOp4::PMEI3*, *pOp4::PMEI5*, *pOp4::VGD1* lines were kindly provided by Sebastian Wolf. *LhG4* codes for a transcription factor that is sequestered in the cytoplasm by a HEAT-SHOCK PROTEIN 90. *GR* codes for glucocorticoid receptor. When Dex is added to the growth medium, it binds to GR which allows LhG4 transport into nucleus where it activates *pOp4* promoter [33]. Genetic crosses between drivers and effectors were used for Dex-induction experiments.

All mutants were genotyped with the primers listed in the Table 1. Plant material for genotyping was collected in a two mL safe-lock tube with one 2.85-3.45 mm glass bead and two 1.7-2.1 mm glass beads. Then, the material was grinded with Tissue Lyser II at 30 s^{-1} frequency for 1.5 minute. Then, tubes were scratched against a tube holder to mix the material, and the samples were grinded for the second time with the same settings. After a short spin down, 400 µL of the extraction buffer (200 mM TrisHCl pH 7.5, 250 mM NaCl, 0.5 % v/v SDS) were added. Tubes were inverted five times and centrifuged at 14 000 g for five minutes. 350 µL of the supernatant were transferred to a 1.5 tube. 350 µL of isopropanol were added. The tubes were inverted five times, incubated at room temperature for 15 minutes and centrifuged at maximal speed for 10 minutes. The supernatant was removed and 350 µL of 70 % EtOH were added. Tubes were shaken for one minute then, centrifuged at maximal speed for five minutes. The supernatant was removed, and the pellets were dried at 65°C for 30 minutes. 50 µL of the TE buffer (10 mM TrisHCl pH 7.5, 1 mM EDTA) were added. The tubes were then homogenised at 65°C for 10 minutes. The polymerase chain reaction (PCR) was realised with REDTaq polymerase (Sigma-Aldrich, R2523) according to the manufacturer's protocol with a modification of dividing all the volumes by half. After the PCR, the samples and a DNA ladder were loaded in a gel (1 g agarose + 4 drops of 0.025% w/v EtBr per 100 mL of TAE buffer). The gel was subjected to 100 mV of electrophoresis for the time needed for the DNA fragments of interest to migrate at a sufficient resolution. The gel was imaged under a UV lamp with a standard digital camera at three different exposure times.

Table 1. Genetic constructs and primers used for their genotyping. *ACTIN 2* (*ACT2*) was used as an internal control. Plasmids were used as PCR controls for transgenes.

Genetic construct	**Plasmid/gene**	**Forward primer (5'-3')**	**Reverse primer (5'-3')**
pxy-2	AT5G61480	GTTTCGGAGTCAAAACAATCG	AATCTCGATTCGTGCAACATC
pxy-4	AT5G61480	TCCTGTGGAAGAAATTGGTTG	GGAAGGTTCGTTTCCAACTTC
pNST3::LHG4-GR;pOp4::mTurquoise2	pVL43	CTCGTCGAGTCCTACCACCATTAT	CGCCCACCTAACATATTGAGTGTGGTCATAATTCTCCATGC
pPXY::LHG4-GR;pOp4::mTurquoise2	pVL45	CATTAGACGCACTCCACAATCATC	CGCCCACCTAACATATTGAGTGTGGTCATAATTCTCCATGC
pSMXL5::LHG4-GR;pOp4::mTurquoise2	pVL41	cttcagtcttcaaacataagaaaggaag	CGCCCACCTAACATATTGAGTGTGGTCATAATTCTCCATGC
pOp4::HAE	pVL104	GTCTCTGGTGCTGTTCCTT	ACTTAGAAGATTCAAGATTCAGAAAACAC
pOp4::IDA	pVL104	AgtATTCAGTCGACTggtacc	CGCCTTTAGGTAAGTAAC
pOp4::PME3	pAZ1	AgtATTCAGTCGACTggtacc	CCTCCACCACCAATAAACTGA
pOp4::PME5	pAZ2	AgtATTCAGTCGACTggtacc	TCGAGGAGCGATCCAATGTC
pOp4::PMEI3	pAZ3	AgtATTCAGTCGACTggtacc	TGGGGTTTGCCACGTGTC
pOp4::PMEI5	pAZ4	AgtATTCAGTCGACTggtacc	TTAGGTCACAAGCTTGTTGA
pOp4::VGD1	pAZ5	AgtATTCAGTCGACTggtacc	AGCGTGACGGGAACATTGGC
ACT2	AT3G18780	ATTCAGATGCCCAGAAGTCTTGTTC	GCAAGTGCTGTGATTTCTTTGCTCA

Plant growth conditions

Seeds were surface sterilised using 70 % v/v EtOH 0.1 % v/v Triton X-100 for 10 minutes and washed with 95 % v/v EtOH for five minutes. Then, the maximum of ethanol was removed, and seeds were dried in a sterile hood. Sterilised seeds were then sown in Petri dishes with autoclaved medium (½ MS 0.5 g/L MES 10 g/L sucrose 8 g/L Phytoagar pH 5.8). For selective media, 5 µg/mL sulfadiazine or/and 10 µg/mL Basta final concentrations were added to the medium at < 60°C. For Dex inductions starting from germination, Dex dissolved in DMSO was added to the medium at < 60°C at 50 µM final concentration. The Petri dishes with seeds were then stratified in darkness at 4°C for at least three days.

For genetic crosses of drivers with effectors, seeds were surface sterilised as described above and sown on selective medium. Driver lines were selected on sulfadiazine, while effector lines were selected on BASTA. When plants flowered, one inflorescence of a mother plant per cross was chosen and all its siliques and open flowers were removed. Three most mature flower buds were opened with

fine forceps and all the flower organs except the pistil were removed. Open young flowers were collected from the father plant. Their anthers were brushed against the stigma of the three dissected mother flowers under a binocular. The resulting inflorescence was attached to a tutor with a tape while avoiding any damage to the stem. The procedure was repeated for two more inflorescences from different mother plants. The pollinated mother plants were then placed at a 10 cm distance from other plants to avoid pollen contamination. Around two weeks later, the mature, yellow-coloured siliques with brown seeds identifiable by transparency were collected in tubes. The closed tubes with siliques were than scratched against the Eppendorf tube holder to release the seeds. The silique valves were then removed. The genetic combinations crossed for this study are listed in Table 2. F1 plants were then propagated to F2 and F3 on double sulfadiazine and BASTA selective medium. Homozygous F2 plants were identified by F3 segregation on double-selective medium and used for Dex inductions. For some preliminary experiments, F2 seeds were used for Dex inductions and genotyped for the presence of transgene before the analysis of hypocotyls.

Table 2. Genetic crosses.

Mother plant	**Father plant**
pPXY::LHG4-GR;pOp4::mTurquoise2	*pOp4::HAE;pOp4::IDA*
	pOp4::PME3
	pOp4::PME5
	pOp4::PMEI3
	pOp4::PMEI5
	pOp4::VGD1
pSMXL5::LHG4-GR;pOp4::mTurquoise2	*pOp4::HAE;pOp4::IDA*
	pOp4::PME3
pNST3::LHG4-GR;pOp4::mTurquoise2	*pOp4::VGD1*

For the Dex inductions starting from germination until adult stage, plants were grown in short day (SD) conditions as previously described for two weeks [34]. Then, plants were transferred to soil and watered twice per week with tap water supplemented with Dex dissolved in DMSO at 15 µM final concentration. After three weeks post-germination, plants were transferred to long day (LD) conditions as previously described [34] and were watered in the same way.

For the analysis of *pxy* mutants, seeds were transferred to soil after stratification. Plants were grown for three weeks at SD then, transferred to LD conditions.

Sample preparation for imaging

For the analysis of radial growth after Dex induction, plants were collected from soil and washed in tap water to get access to hypocotyls. Hypocotyls were collected with a scalpel while leaving references for the longitudinal axis. Hypocotyls were fixed in 500 µL of 4 % w/v PFA dissolved in PBS pH 7.0 in darkness at 4°C over-night. Then, hypocotyls were incubated for 20 minutes in 10 % sucrose 1 % w/v PFA dissolved in PBS pH 7.0 then, for 20 minutes in the same solution but with 20 % sucrose then, for 30 minutes in the same solution but with 30 % sucrose. Afterwards, hypocotyls were embedded in 7 % low temperature-melting agarose and sectioned transversally to the longitudinal axis using the vibratome Leica VT1000 S and Wilcoxon blades (one blade per three samples) at the speed set to 10 units and the frequency set to 70 Hz. Hypocotyls were immerged in PBS pH 7.0 buffer and cut from stem to root direction. After two first sections, four to 10 sections of 75 µm thickness were collected with a fine brush in 500 µL of ClearSee (10 % w/v xylitol, 15 % w/v sodium deoxycholate, 25 % w/v urea). Afterwards, the samples were cleared and stained as described previously [44] but with some following modifications.

Hypocotyl sections collected after Dex inductions were stained for 60 minutes with 0.1 % w/v DirectRed23 diluted in ClearSee, washed three times with ClearSee and mounted in ClearSee, on microscopic slides. For some early experiments, ClearSee was replaced by PBS pH 7.0. In this case, samples were kept at 4°C in darkness and imaged in less than a week. While ClearSee cleared and mounted samples were kept at room temperature in darkness for undetermined period without losing their quality.

Hypocotyl sections collected for the phenotyping of *pxy* mutants were first stained overnight with 0.2 % w/v Basic Fuchsin diluted in ClearSee. After washing three times with ClearSee, sections were stained with 0.1 % DirectYellow96 diluted in ClearSee the same way as indicated higher for DirectRed23. The mounting was done in ClearSee on microscopic slides.

Imaging of plants

Seedlings grown in Petri dishes were scanned with a paper scanner at 800 dpi resolution.

Adult plants were imaged with digital photography camera in close mode with medium resolution.

Hypocotyl sections were imaged with Leica SP8 confocal microscope. 20x glycerol-immerged objective was used to match the refractive index of ClearSee which is higher than the reflective index of water. Fluorescent channels were acquired sequentially. The laser excitation and detector window

wavelength settings are indicated in Table 3. Transmission light images were acquired in parallel to assess the transparency of samples. Tile scans of 2 x 2, 3 x 3 or 4 x 4 were performed to capture a full section. Every tile was captured with bidirectional scan direction X, 1.5 AU pinhole, 3 times line averaging, at 2048 x 2048 image resolution, 400 Hz scan speed.

Table 3. Fluorescent excitation and emission settings for confocal microscopy.

Channel	**Excitation, nm**	**Emission, nm**	**Experiment**
mTurquoise2	458	480-515	Dex induction of driver-effector lines
DirectRed23	561	590-660	
DirectYellow96	488	500-540	Phenotyping of *pxy* mutants
Basic Fuchsin	561	600-650	

Image and data analysis

The scans of seedlings were processed in FIJI (Macro 1, available at https://github.com/thomasgreb/Zakieva-et-al-hypoQuant.git).

The tile scans of hypocotyl images were processed in FIJI (Macro 2, available at https://github.com/thomasgreb/Zakieva-et-al-hypoQuant.git).

Semi-quantitative measurement of the surface of hypocotyl sections (Figure 6) was realised in FIJI with the free zone selection tool.

Radial profile plot was realised on the mTurquoise2 fluorescence micrograph map according to the published documentation found at https://imagej.nih.gov/ij/plugins/radial-profile.html. The signal intensities were exported in .csv format. The distance from the section's centre was transformed from µm to %. The mean and standard deviation for every point were calculated out of 10 biological replicates. The graphs were generated in GraphPad Prism 5.

The quantitative histology protocol is outlined in Figure 2. The confocal images of hypocotyl sections were processed in PlantSeg according to the documentation published at https://github.com/hci-unihd/plant-seg. The ground truth was generated with the proofreading tool of PlantSeg according to the documentation published at https://github.com/hci-unihd/plant-seg-tools. Confocal images of hypocotyl sections stained with cell wall specific dye were submitted to a CNN U-net model for cell boundary prediction trained on three-dimensional (3D) confocal images of *Arabidopsis* ovules [37]. This model was additionally trained with 3D confocal images of shoot apical meristem by Lorenzo Cerrone (Heidelberg Collaboratory for Image Processing, Heidelberg University,

Heidelberg, Germany). 25 ground truths in total of wild type (WT), *pxy-2* and *pxy-4* at 3, 4, 4.5 and 5 weeks post-germination (wpg) were used for the training of CNN U-net two-dimensional (2D) boundary prediction model. 10 ground truths were used for the first round of training, 10 – for the second and five – for the third. The segmentation parameters were manually adjusted (Table 4). The performance of segmentation parameters sets and boundary prediction models was evaluated according to the documentation published at https://github.com/hci-unihd/plant-seg/tree/master/evaluation. The segmentation scores obtained from this evaluation were processed in R (Script 2, available at https://github.com/thomasgreb/Zakieva-et-al-hypoQuant.git). After processing in PlantSeg, the resulting segmentations and raw confocal images were submitted to MGX (Figure 2). A vectorised cell mesh was generated from the superpixel segmentation. Basic Fuchsin and DirectYellow96 confocal images were projected on the mesh. 15 cell descriptors were computed as described previously [45] [41] [46] [12]: Basic Fuchsin signal, DirectYellow96 signal, area, perimeter, major axis, minor axis, aspect ratio, circularity, rectangularity, lobeyness, incline angle, cell degree, betweenness centrality, radial coordinate, circumferential coordinate. Heatmaps of the first 13 descriptors were generated. Cell type classification was realised as described previously [47]. The resulting data were extracted as .csv files and processed in R (Script 3, available at https://github.com/thomasgreb/Zakieva-et-al-hypoQuant.git).

Table 4. Segmentation parameters (non-default) for PlantSeg.

Segmentation parameter	**Value**
Model Name	model_20210910
Patch Size	0 128 128
Stride	Accurate
Device Type	cuda
Algorithm	MutexWS
Under-/Over-segmentation factor	0.45
CNN Prediction Threshold	0.06
Watershed Seeds Sigma	4.2
Watershed Boundary Sigma	4.2

All figures were generated with Adobe Illustrator CS6. The text and intermediate data were generated and processed in Microsoft Office.

Results

In my project, I studied morphogenesis in the context of the *Arabidopsis* vascular system. First, I investigated how tissue-specific cell wall modifications can affect cell, tissue, organ and whole plant morphogenesis. Secondly, I established a protocol to perform quantitative histology. Finally, I used the quantitative histology to analyse *pxy* mutants and showed the robustness of this method to distinguish the effect of different mutant alleles.

1. Cell wall role in tissue morphogenesis

To understand the role of the cell wall in vascular tissues morphogenesis I induced tissue-specific expression of cell wall modifying proteins. The tissue specificity was provided by the genetic construct called “driver”, while the expression of the transgene coding for the cell wall-modifying protein was provided by the genetic construct called “effector”. I looked at the plant phenotype at macro- and microscopic levels.

1.1. Ectopic vascular tissues-specific expression of transgenes coding for cell wall modifying proteins in whole plants

I got interested in how the cell wall modifying effectors would affect hypocotyl tissues morphogenesis. I continuously induced the expression of *HAE-IDA* and *VGD1* under cambium and xylem-specific drivers starting from the seed’s germination. I analysed the resulting phenotype of plants and hypocotyl tissues at different developmental stages.

1.1.1. Plant morphology

After 2 weeks post-germination and induction, differences in plant phenotypes were observed. When *HAE-IDA* was expressed under the control of the *pSMXL5>>* driver, rosette size was reduced, and root architecture was disturbed (Figure 3A). *HAE-IDA* expression under the control of the *pPXY>>* driver induced even a more drastic effect: rosettes were drastically smaller and lateral roots were rare or totally absent (Figure 4A). However, when *VGD1* was expressed under the control of the *pPXY>>* driver, no flagrant phenotype was observed (Figure 5A).

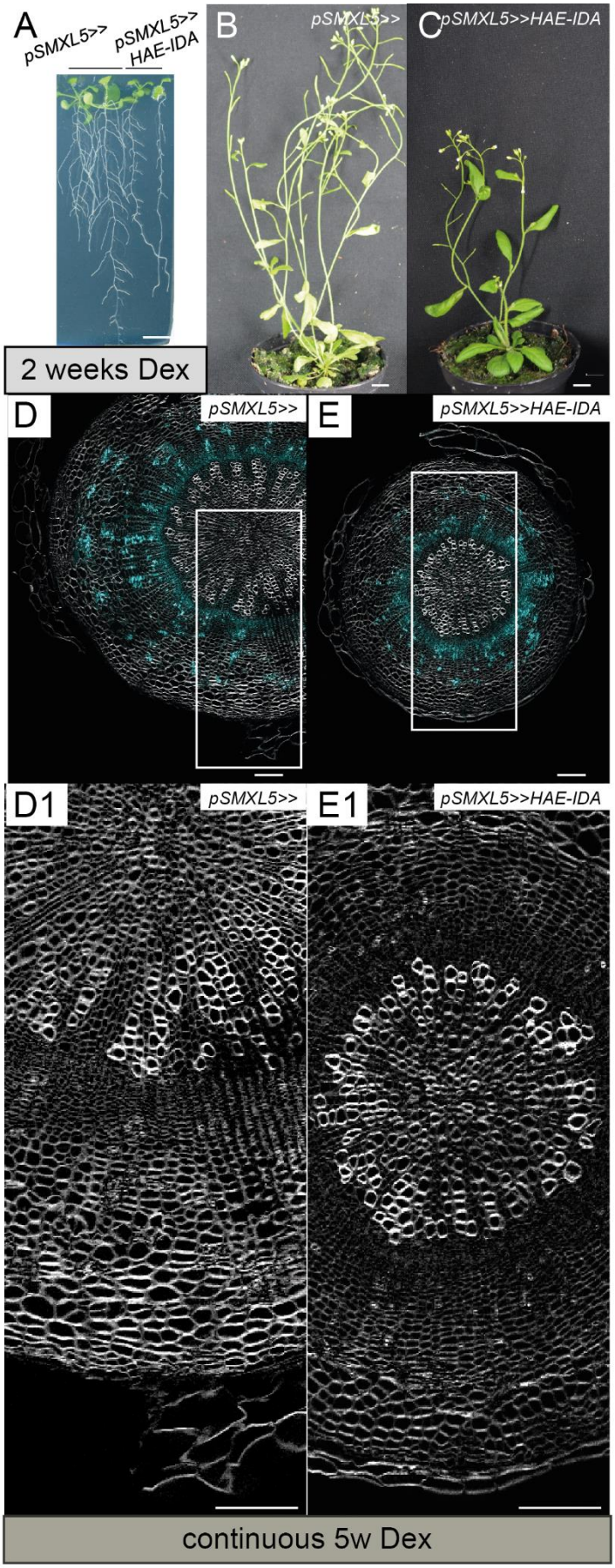

Figure 3. <u>Ectopic expression of *pSMXL5>>HAE-IDA*</u>. Plant phenotype after continuous Dex induction for 2 weeks (**A**) with *pSMXL5>>* on the left and *pSMXL5>>HAE-IDA* on the right, after continuous Dex induction for 5 weeks (**B**, **C**). **D-E**. Hypocotyl anatomy after continuous Dex induction for 5 weeks. **D1** and **E1** are magnifications of the zones indicated by a white rectangle respectively in **D** and **E**. Plant genotypes are indicated in insets at top-right. Scale bars in **A-C** correspond to 1 cm, in **D-E** - to 100 µm.

After plants were transferred to soil and grown for 3 more weeks (5 wpg and induction), more drastic phenotypic alterations were observed. *pPXY>>VGD1* lines showed decreased growth and dark green leaves compared to *pPXY>>* driver line. Interestingly, these small plants still managed to flower (Figure 5B, C). Ectopic *HAE-IDA* expression also induced developmental defects in adult plants. When driven by *pSMXL5>>*, this effector induced a dwarf phenotype: rosette and shoot decreased in size (Figure 3B, C). *HAE-IDA* had even a more dramatic effect when its expression was driven by *pPXY>>*: rosette and shoot were drastically smaller (Figure 4B, C).

No significant phenotype at plant morphology level was observed for other induction experiments: *pSMXL5>>PME3*, *pPXY>>PME5*, *pPXY>>PMEI3*, *pPXY>>PMEI5*.

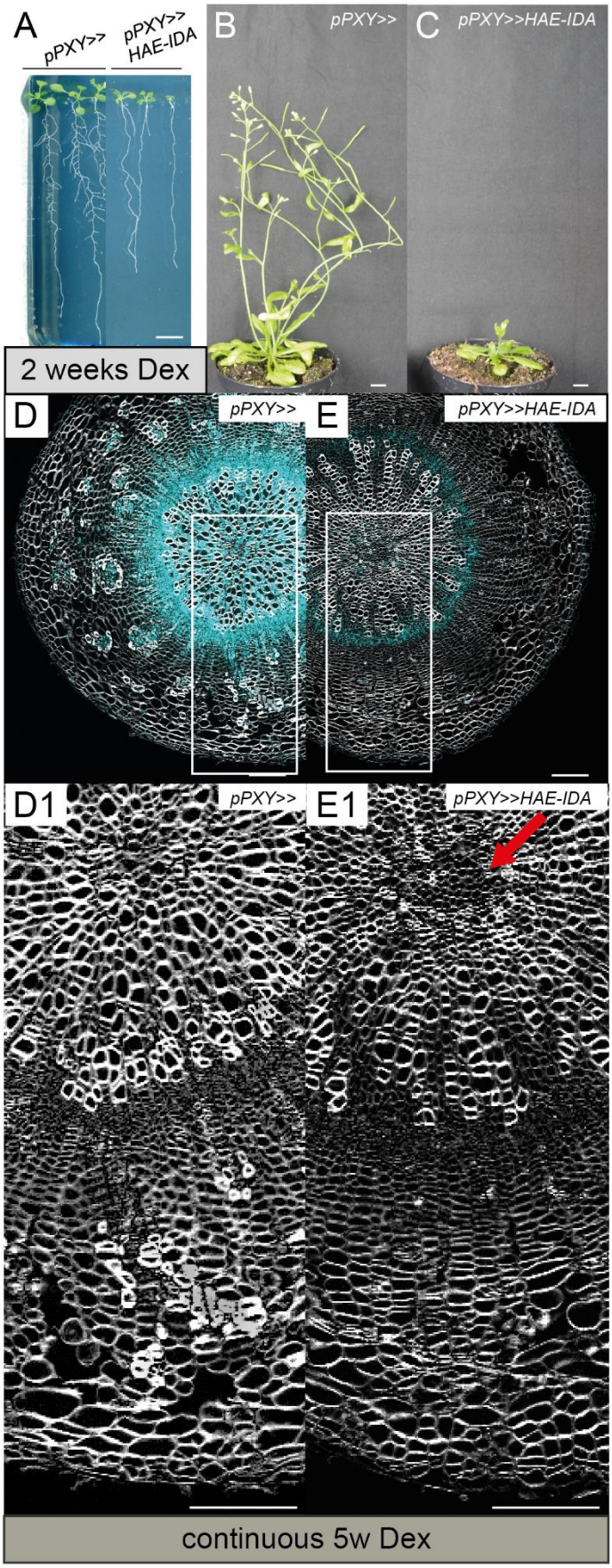

Figure 4. <u>Ectopic expression of *pPXY>>HAE-IDA*</u>. Plant phenotype after continuous Dex induction for 2 weeks (**A**) with *pPXY>>* on the left and *pPXY>>VGD1* on the right, for 5 weeks (**B**, **C**). **D-E**. Hypocotyl anatomy after continuous Dex induction for 5 weeks. **D1** and **E1** are magnifications of the zones indicated by a white rectangle respectively in **D** and **E**. Plant genotypes are indicated in insets at top-right. Red arrow in **E1** indicates numerous small cells in xylem. Scale bars in **A-C** correspond to 1 cm, in **D-E** - to 100 µm.

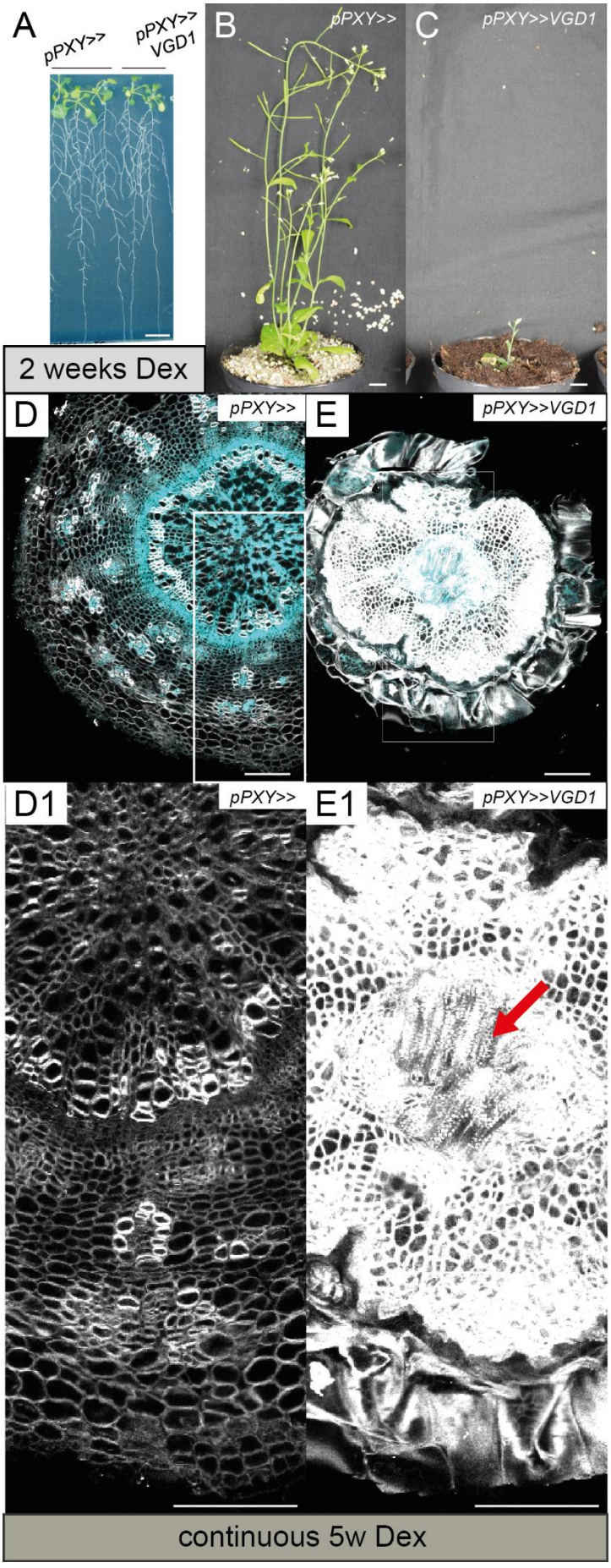

Figure 5. <u>Ectopic expression of *pPXY>>VGD1*</u>. Plant phenotype after continuous Dex induction for 2 weeks (**A**) with *pPXY*>> on the left and *pPXY>>VGD1* on the right, for 5 weeks (**B**, **C**). **D-E**. Hypocotyl anatomy after continuous Dex induction for 5 weeks. **D1** and **E1** are magnifications of the zones indicated by a white rectangle respectively in **D** and **E**. Plant genotypes are indicated in insets at top-right. Red arrow in **E1** indicates stripes typical for transversal optical section of a xylem vessel. Scale bars in **A-C** correspond to 1 cm, in **D-E** - to 100 µm.

1.1.2. Hypocotyl anatomy

After 5 weeks post-germination and induction, hypocotyls were collected, fixed, sectioned and stained with DirectRed23 to visualize cell boundaries.

VGD1 expression under the control of the *pPXY>>* driver induced a dramatic effect on hypocotyl organization. Hypocotyl diameter was reduced (Figure 6). Its radial symmetry was broken, cortex cells were present and attached to the periderm, cell wall staining was enhanced (Figure 5D, E). All tissues looked disorganized and difficult to distinguish one from each other. Especially xylem parenchyma was not visible at all. A stripe-like structure observed in xylem could correspond to xylem vessels positioned perpendicularly to hypocotyl rotational axis instead of parallel to it as in WT-like situation (Figure 5D1, E1, red arrow).

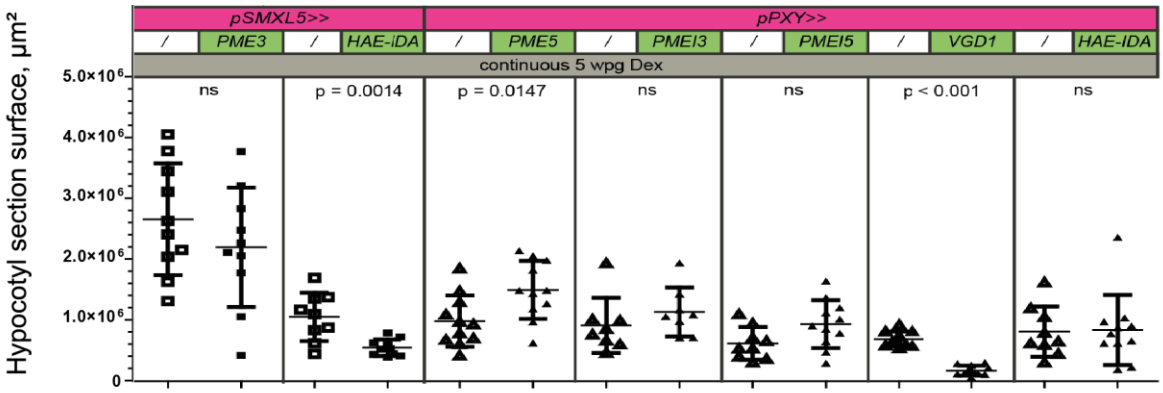

Figure 6. Summary of the continuous induction experiments and quantification of hypocotyl tissues. A. Hypocotyl section surface in µm². As hypocotyls have radial symmetry, surface of a hypocotyl section can directly correspond to hypocotyl diameter. Plant genotypes are indicated by the first pink bars for the driver component and by the second green bars for the effector component if applicable. Middle bars of graphs correspond to the mean. Upper and lower bars of graphs correspond to standard deviation. Vertical lines delimit independent experiments. Two-tailed Student t-test was performed between driver and driver-effector line in each experiment. No significant difference at 95 % confidence interval is indicated by ns.

HAE-IDA expression under the control of the *pSMXL5>>* driver induced hypocotyl diameter decrease (Figure 6). However no obvious alteration was observed at tissue or cell morphology levels (Figure 3D, D1, E, E1). An opposite trend appeared when *HAE-IDA* was expressed under the control of the *pPXY>>* driver. Hypocotyl diameter was not affected (Figure 6). However, xylem cells appeared smaller and more numerous in *pPXY>>HAE-IDA* lines compared to *pPXY>>* lines (Figure 4D, D1, E, E1, red arrow).

Induced *pPXY>>PME5* lines showed an increased hypocotyl diameter (Figure 6). No significant phenotype at cell morphology level was observed in *pSMXL5>>PME3*, *pPXY>>PMEI3* or *pPXY>>PMEI5*. Both *pSMXL5>>* and *pSMXL5>>PME3* showed high intra-sample variation for hypocotyl diameter. Both

values are also at least twice higher compared to other experiments, suggesting that *pSMXL5>>PME3* hypocotyls were not collected at the same developmental stage as other driver-effector lines (Figure 6).

In summary, continuous expression of *VGD1* or *HAE-IDA* under the control of cambium specific drivers induced organ, tissue and cell morphology defects. Continuous expression of *PME5* under *pPXY* driver induced a mild hypocotyl tissues phenotype. This suggests that alteration of cell wall properties in vascular tissues affects radial growth and vascular tissues morphogenesis, but only some cell wall modifying proteins are capable of ectopically induce these alterations.

1.2. Ectopic vascular tissues-specific expression of transgenes coding for cell wall modifying proteins during radial growth

After identifying the two most potent morphogenetic effectors in vascular tissues – *VGD1* and *HAE-IDA* – I treated driver-effector lines with Dex after 3 wpg. This temporal restriction allowed me to avoid all morphogenetic effects which might occur before the onset of radial growth.

1.2.1. Plant morphology

After 3 wpg followed by 2 weeks of Dex induction, *pPXY>>HAE-IDA* plants did not show any obvious alteration compared to *pPXY>>* driver lines. Rosettes seemed slightly smaller according to a qualitative estimation (Figure 7A, B). However, after 4.5 weeks induction, *pPXY>>HAE-IDA* plants had shorter stems, decreased inflorescence internodes and faster siliques maturation compared to *pPXY>>* driver (Figure 7C, D, red arrow).

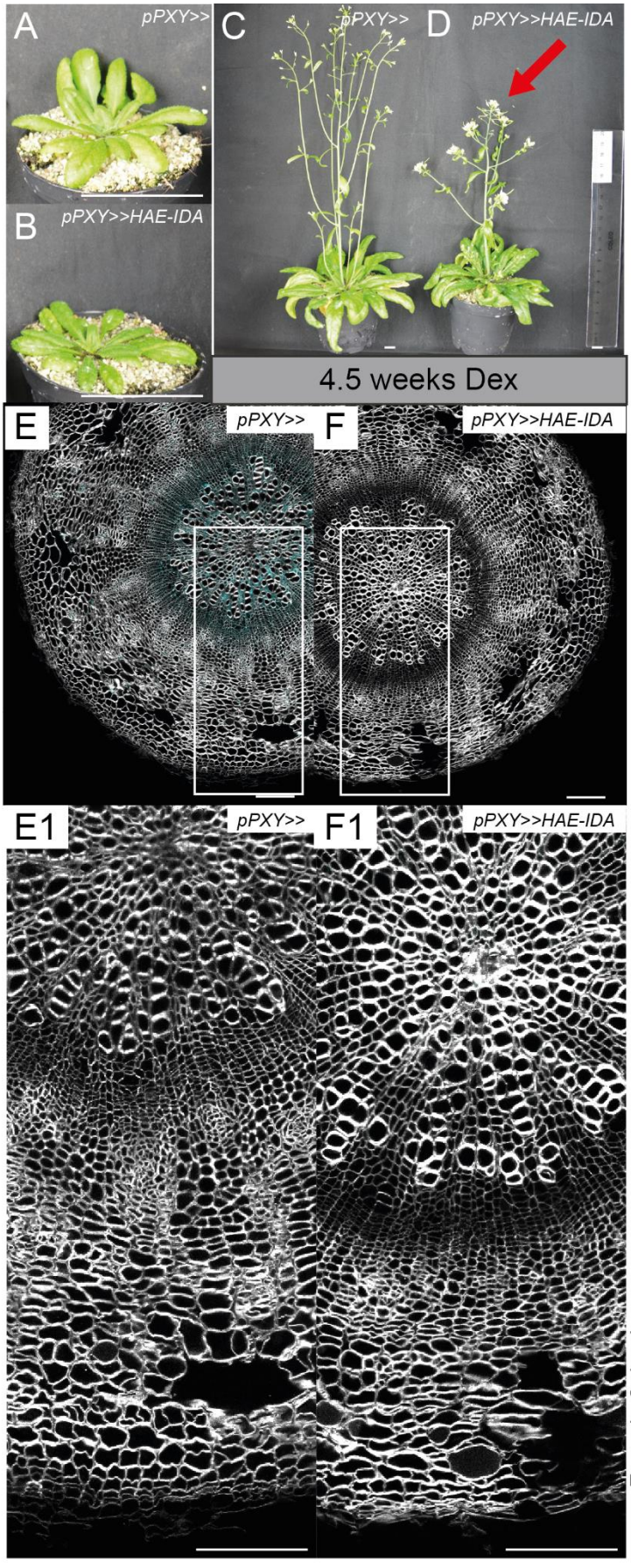

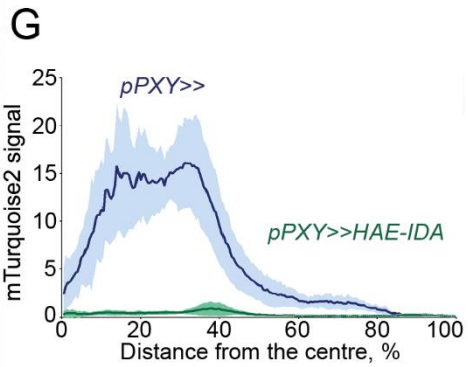

Figure 7. <u>Ectopic expression of *pPXY>>HAE-IDA* during radial growth</u>. Plant phenotype after Dex induction from 3 to 5 wpg (**A**, **B**), from 3 to 7.5 wpg (**C**, **D**). **E-F**. Hypocotyl anatomy after Dex induction from 3 to 5 wpg. **E1** and **F1** are magnifications of the zones indicated by a white rectangle respectively in **E** and **F**. Plant genotypes are indicated in insets at top-right. **G**. Radial profile plot of *pPXY>>* (**E**, blue) and *pPXY>>HAE-IDA* (**F**, green). Scale bars in **A-B** correspond to 1 cm, in **E-F** - to 100 µm.

1.2.2. Hypocotyl anatomy

After 2 weeks of Dex induction, *pPXY>>HAE-IDA* lines did not show any significant phenotype at tissue organization or cell morphology level (Figure 7E, E1, F, F1). However, mTurquoise2 signal (Figure 7E, F, cyan, G) significantly decreased.

The expression of *VGD1* in the same domain resulted in a different phenotype. mTurquoise2 level did not change (Figure 8C, D, E), but the cell morphology did. Xylem parenchyma cells appeared smaller and of a more triangular shape (Figure 8D2) compared to *pPXY>>* (Figure 8C1). On the whole plant level, *pPXY>>VGD1* driver-effector rosettes seem smaller (Figure 8B) compared to the *pPXY>>* driver ones (Figure 8A).

When *VGD1* is expressed in the *NST3* zone, corresponding to xylem parenchyma, I saw a different phenotype again. Cells with thick cell walls appeared in the distal xylem (Figure 9C, C1, D, D1). They looked very similar to xylem fibers of xylem-II formed during plant transition to flowering [reference-TBD]. However, neither *pNST3>>VGD1* driver-effector, nor *pNST3>>* driver were flowering at that moment (Figure 9A, B). These xylem fibers and their neighbours seemed having a higher mTurquoise2 signal (Figure 9C, D, cyan), however it was not confirmed by the quantification with radial plot profile (Figure 9E). The cambium zone seems to be larger in *pNST3>>VGD1* driver-effector compared to *pNST3>>* driver (Figure 9C, D, red arrows). However, it is difficult to confirm without a quantification.

In summary, ectopic vascular tissues-specific expression of *HAE-IDA* and *VGD1* during radial growth affected vascular tissue's identity that was observed at the *PXY* level of expression, tissue size and cell morphology levels. Some of these properties could be quantified with semi-quantitative histology like hypocotyl section surface or fluorescent marker intensity. I identified cell wall-related effectors whose expression alter organ and tissue anatomy that can be induced on demand in distinct domains.

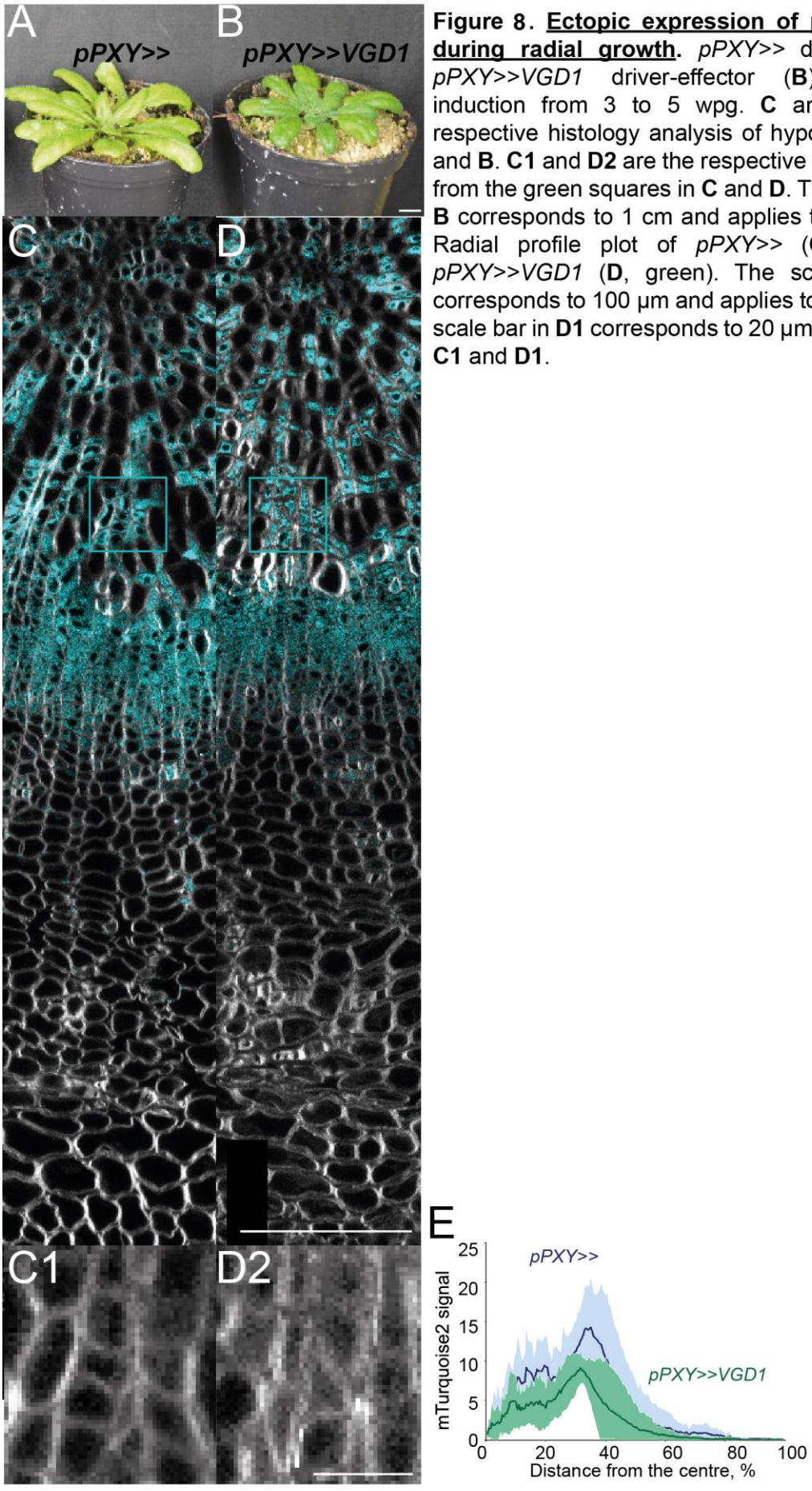

Figure 8. <u>Ectopic expression of pPXY>>VGD1 during radial growth</u>. *pPXY>>* driver (**A**) and *pPXY>>VGD1* driver-effector (**B**) after Dex induction from 3 to 5 wpg. **C** and **D** are the respective histology analysis of hypocotyls from **A** and **B**. **C1** and **D2** are the respective magnifications from the green squares in **C** and **D**. The scale bar in **B** corresponds to 1 cm and applies to **A** and **B**. **E**. Radial profile plot of *pPXY>>* (**C**, blue) and *pPXY>>VGD1* (**D**, green). The scale bar in **D** corresponds to 100 µm and applies to **C** and **D**. The scale bar in **D1** corresponds to 20 µm and applies to **C1** and **D1**.

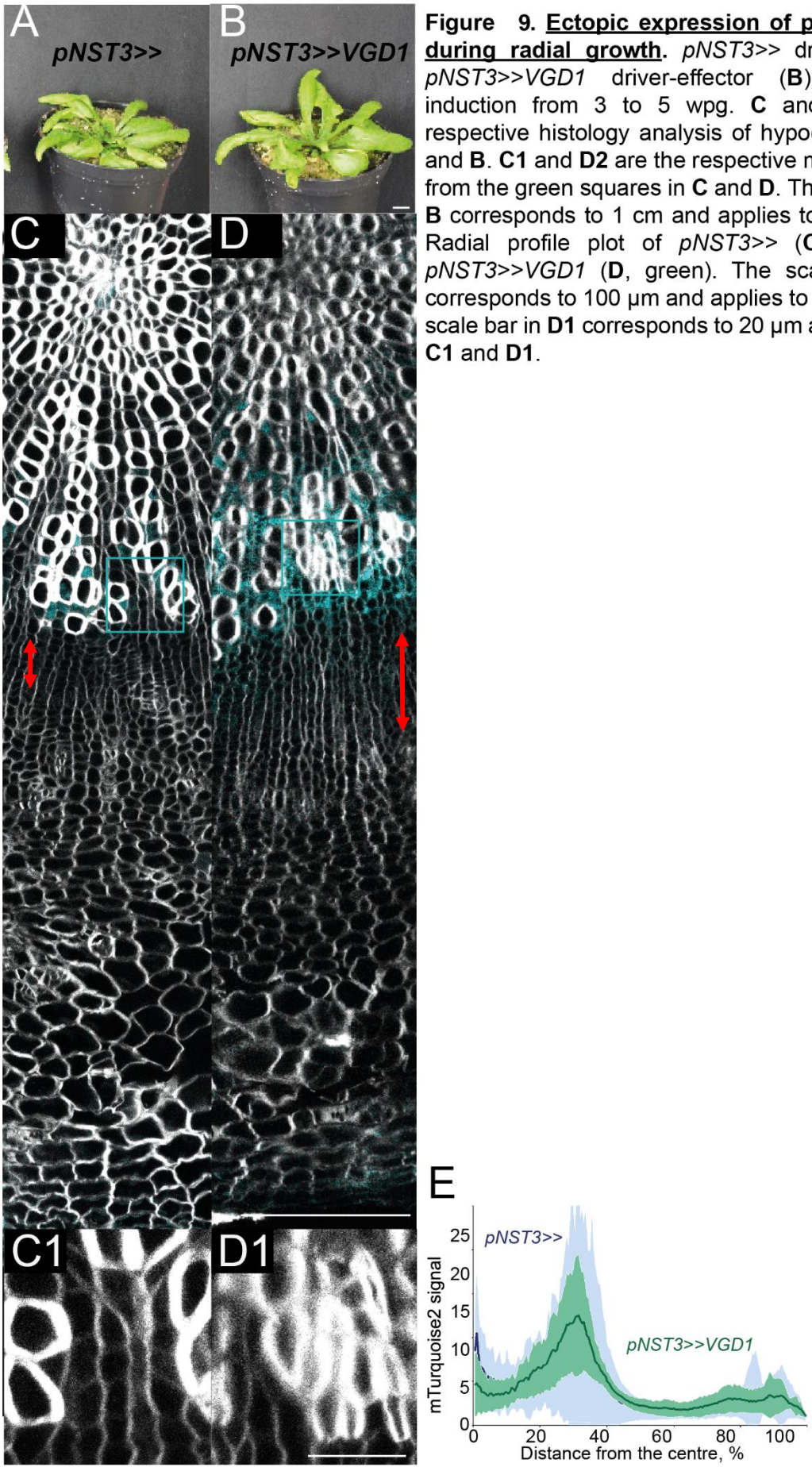

Figure 9. <u>Ectopic expression of pPXY>>VGD1 during radial growth</u>. *pNST3>>* driver (**A**) and *pNST3>>VGD1* driver-effector (**B**) after Dex induction from 3 to 5 wpg. **C** and **D** are the respective histology analysis of hypocotyls from **A** and **B**. **C1** and **D2** are the respective magnifications from the green squares in **C** and **D**. The scale bar in **B** corresponds to 1 cm and applies to **A** and **B**. **E**. Radial profile plot of *pNST3>>* (**C**, blue) and *pNST3>>VGD1* (**D**, green). The scale bar in **D** corresponds to 100 µm and applies to **C** and **D**. The scale bar in **D1** corresponds to 20 µm and applies to **C1** and **D1**.

2. Establishment of the quantitative histology protocol

The semi-quantitative analysis of hypocotyl tissues is only one step in analysing the data that can be extracted from hypocotyl tissues. A general approach analysing every single cell of an image can bring a fuller and unbiased picture. Therefore, I established a quantitative histology protocol standardized to all confocal images with cell boundary staining. It consists of identifying cell and tissues signal, morphological and topological properties based on the quantitative data acquired from every single cell. This method consists of three major steps: image segmentation, cell and tissue descriptors extraction and cell type classification (Figure 2).

2.1. Segmentation and boundary prediction model training

Confocal images of hypocotyl sections were segmented in "PlantSeg" and proofread in "Proofreading tool of PlantSeg" to get 25 ground truths. The images came from different time points and genotypes to train the boundary prediction model not only to standard conditions but also to challenging images. Indeed, at different developmental stages, more diversity of cell wall morphologies were observed (Figure 12A1-D1), while *pxy* mutants showed challenging cases of compressed cells or noisy signal (Figure 13A1-D1, 14A1-D1). The ground truths were used for the training of the U-net model for three iterations (Figure 2, part 1). Confocal microscopy image of wild type at 3.5 wpg (Figure 10A) was segmented with boundary prediction models at different stages of training (Figure 10C, D, F-H). The training iterations were evaluated on ground truths (Figure 10B) qualitatively (Figure 10A-D) and quantitatively (Figure 10E-H).

When comparing the boundary predictions maps before (Figure 10C) and after the training (Figure 10D), we can appreciate a reduction in the thickness of cell boundaries approaching the precision of the ground truth (Figure 10B). For some cell boundaries, the model remains uncertain though (Figure 10D, violet zones inside cells) suggesting that the model can be trained further.

We can also see this uncertainty when analysing segmentations quantitatively by looking at the resulting cell descriptors. I compared the cell area of all the cells from wild type, *pxy-2* and *pxy-4* quarter of hypocotyls segmented by the trained model with or without proofreading (Figure 10E). I chose 5 wpg to have a bigger cell number for comparison. There is a significant decrease in cell size after proofreading (Figure 10E, ***) suggesting that the current model cannot produce a perfect segmentation yet. As there are fewer small cells according to the model than to the ground truth, it means that the model undersegments images.

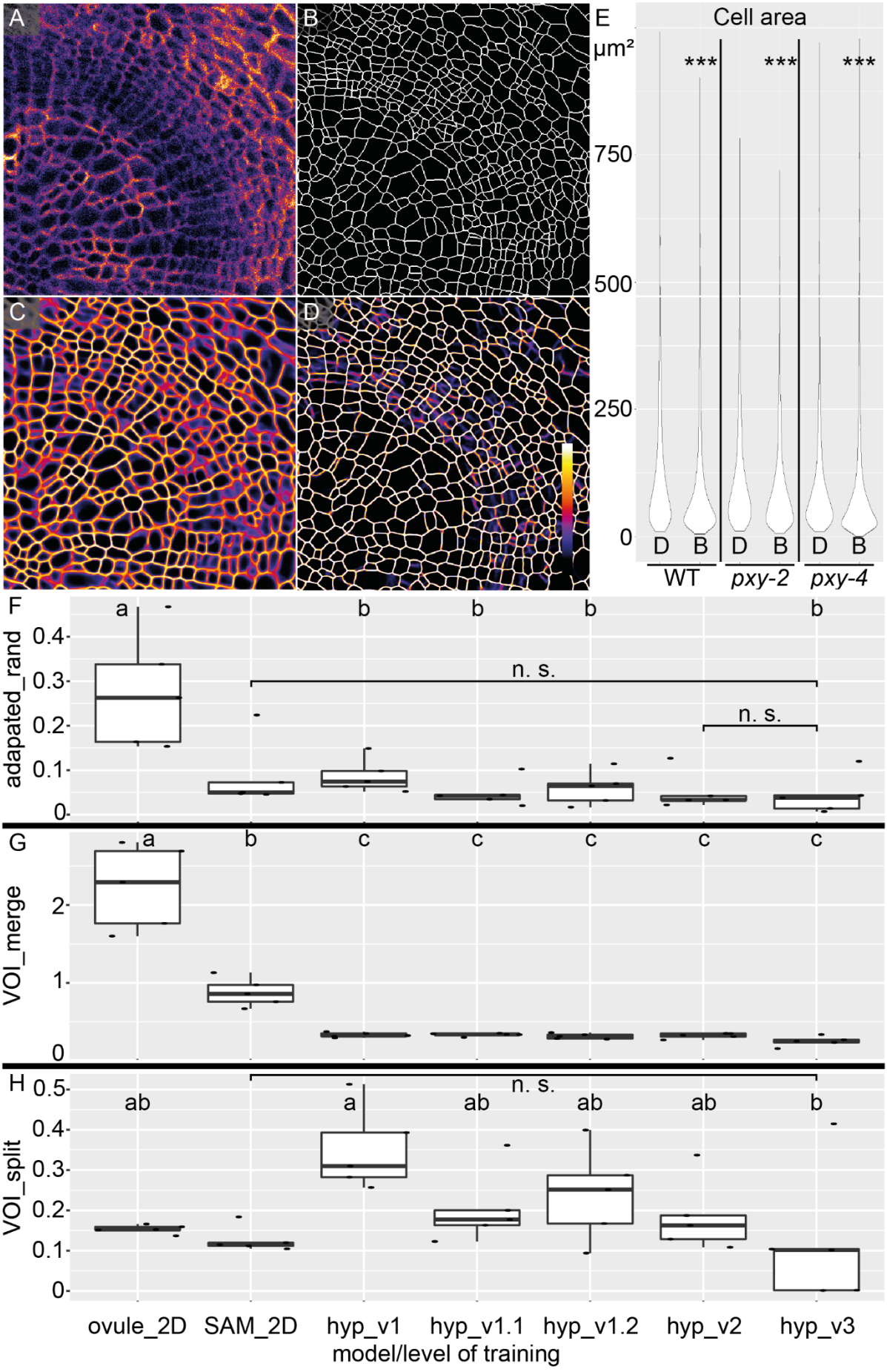
A
B
C
D
E
Cell area
µm²
750
500
250
0
***
***
***
D
B
D
B
D
B
WT
pxy-2
pxy-4
F
adapated_rand
0.4
0.3
0.2
0.1
0
a
b
b
b
b
n. s.
n. s.
G
VOI_merge
2
1
0
a
b
c
c
c
c
c
H
VOI_split
0.5
0.4
0.3
0.2
0.1
0
ab
a
ab
ab
ab
b
n. s.
ovule_2D
SAM_2D
hyp_v1
hyp_v1.1
hyp_v1.2
hyp_v2
hyp_v3
model/level of training

Figure 10. Training of the boundary prediction model. A. Crop of a wild type hypocotyl section at 3.5 wpg stained with DirectYellow96. **B**. Ground truth of **A**. **C-D.** Boundary prediction maps of **A** where the highest value (see the calibration bar in **D**) corresponds to 100 % of probability for the pixel to be a cell boundary, while the lowest value corresponds to 0 % of this probability. **C**. Boundary prediction map by the default PlantSeg model "confocal_2D_unet_bce_dice_ds2x" (ovule_2D in **F-H**). **D**. Boundary prediction map by the model after training (hyp_v2 in **F-H**). **E**. Cell area of cells in a quarter of a hypocotyl section of three indicated genotypes at 5 wpg. D corresponds to the values extracted from a non-proofread segmentation like in **D**. B corresponds to the values extracted from the ground truth like in **B**. **F-H**. Segmentation evaluation scores with 0 value corresponding to the perfect match of a segmentation graph-partitioned from the boundary prediction map with the one graph-partitioned from the ground truth. Every model on the x-axis corresponds to the iterations of training where ovule_2D is the default PlantSeg model "confocal_2D_unet_bce_dice_ds2x", SAM_2D is ovule_2D trained on shoot apical meristem, hyp_v1 is SAM_2D trained on 10 hypocotyl sections, hyp_v1.1 and hyp_v1.2 are hyp_v1 trained on 10 hypocotyl sections with parallelisation of hyperparameters adjustment, hyp_v2 is hyp_v1 trained on the same 10 hypocotyl sections as hyp_v1.1 and hyp_1.2 but without the parallelisation, hyp_v3 is hyp_v2 trained on 5 hypocotyl sections. **F**. Adapted rand score measuring how much superpixels from the evaluated segmentation match to the ones graph partitioned from the ground truth. Under- (**G**) and oversegmentation (**H**) scores. Violin plots in **E** represent the distribution. *** indicate $p < 0.001$ after pairwise Wilcoxon test between D and B. Boxplots with wiskers in **F-H** represent standard values. Letters correspond to statistically different groups after one-way ANOVA test and post-hoc pairwise t-test with p-value < 0.05. Samples without letters showed a non normal distribution and were compared to hyp_v3 with pairwise Wilcoxon test resulting in non significant (n. s.) difference (p-value > 0.05).

Another quantitative way of model evaluation is calculating the segmentation scores. Adapted rand estimates how much the superpixels or cells generated by the model fit to the superpixels of the ground truth. This is the most general score used in segmentation evaluation. Adapted rand decreased significantly after the first training with the images of SAM and remained stable for the rest of the training (Figure 10F). VOI_merge showing the degree of undersegmentation decreased after the first round of training with the images of SAM and dropped even more after the second round of training with images of hypocotyl sections after which, it remained stable over the training (Figure 10G). VOI_split estimating the oversegmentation increased after the first hypocotyl images were introduced into the training, but gradually dropped with the following rounds of training (Figure 10H). Such variations of the three scores during the training suggests that the boundary prediction model learned from the first training on SAM recognising and splitting hypocotyl cells more accurately. At the second training, the model started to oversplit hypocotyl cells probably because it learned for the very first time from hypocotyl images about the challenging noisy zones. But gradually with next steps of training on hypocotyl sections, the model corrected the VOI_split (Figure 10H) score without compromising neither the adapted rand (Figure 10F), nor the VOI_merge (Figure 10G). It looks like VOI_merge could be reduced more according to the comparison of superpixels mean area between the segmentation by the model and the ground truth (Figure 10E, G).

The proofreading time depends on how much the user is familiar with the proofreading tool and how thorough should be the segmentation. After the training, I spent roughly two to four hours on correcting the segmentation coming from a quarter of a 3.5 wpg old hypocotyl section. 15 to 20 hours were spent on correcting the segmentation coming from a quarter of a 5 wpg old hypocotyl section. This correction time was reduced by half compared to the correction time spent on segmentations generated by default models.

In summary, the training of CNN U-net cell boundary prediction model substantially improved its accuracy and reduced the correction time of the resulting segmentations. The resulting machine learning model did not reach the segmentation level of a human expert but it is still possible to be trained further.

2.2. Cell type classification

Next, the segmentations and raw microscopy images were uploaded to MGX. Cell descriptors were extracted (Figure 2, part 2) and used for SVM cell type classification (Figure 2, part 3). For every cell type, I selected cell descriptors useful for the classification and annotated a few cells. With this information, an SVM classifier was trained allowing it to attribute all the rest of the cells to the corresponding cell types based on the values of the provided cell descriptors.

I wanted to test if cell type classification is prone to human bias or to the level of expertise. Therefore, my four colleagues annotated cell types of their choice for the same image (Figure 11A). I annotated the same images with the maximum cell types I knew from the literature (Figure 1B). Then, SVM-trained cell type classification was realised with the same settings but with annotations from my colleagues (Figure 11B-E) or myself (Figure 11F). At least 10 cells per cell type were annotated. The users chose the cell types by themselves. The annotation and classification of xylem and cambium was consistent between different experts. However, for phloem and periderm, there were some disagreements. Some experts consider phloem as a continuous tissue spreading radially from cambium to periderm (Figure 11B, F), others subdivide it on distal and proximal (Figure 11C-E). Sometimes phloem poles are indicated, scattered within phloem parenchyma (Figure 11C-F). Phloem fibers and subdivision of periderm was indicated only by myself (Figure 11F). Even so the SVM model struggled to classify these too specific phloem and periderm subgroups. Indeed phloem could be automatically subdivided into proximal and distal if a sufficient annotation was provided (Figure 11D, magenta and cyan), but the resulting automated classification of phloem poles (Figure 11C-F) did not correspond to the pattern often seen with tissue-specific promoter-reporter markers like pAPL::GFP [47]. Phloem fibers were annotated only by myself and the classifier struggled to identify them (Figure

11F). Basic Fuchsin staining caused some damage on the borders of hypocotyl sections making periderm cell type sub-classification difficult. After considering these different expert visions and technical limitations, I decided to use the cell type annotation method of the Expert1 (Figure 11B) and manually identify phloem fibers after the automated classification.

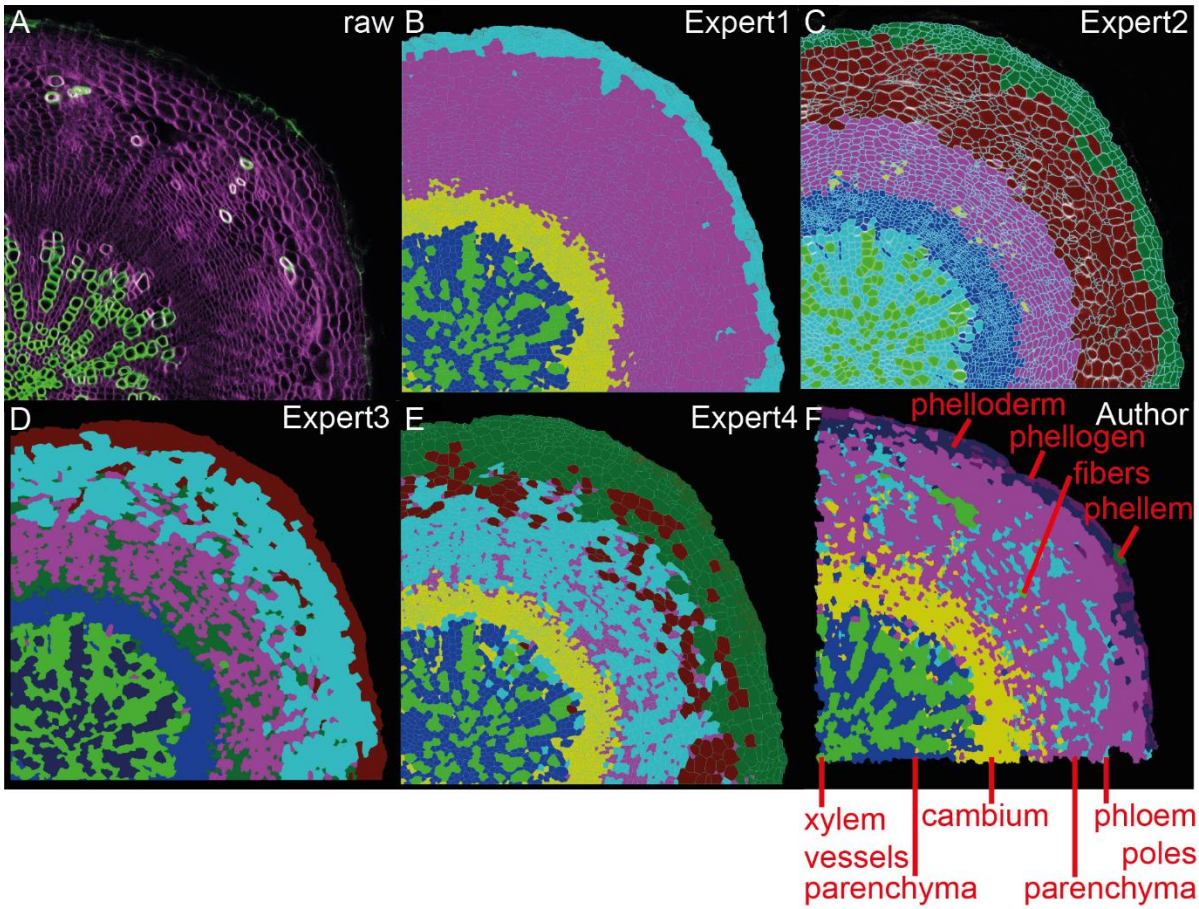

Figure 11. Cell type classification by different experts. A. Confocal microscopy image of hypocotyl section collected from wild type at 5 wpg and stained with Basic Fuchsin (green, lignin), and DirectYellow96 (magenta, cellulose). **B.** Cell type classification after training by the Expert1 who identified 5 cell types: xylem vessels (green), xylem parenchyma (blue), cambium (yellow), phloem (magenta) and periderm (cyan). **C.** Cell type classification after training by the Expert2 who identified 7 cell types: xylem vessels (green), xylem parenchyma (cyan), cambium (blue), proximal phloem (magenta), phloem poles (yellow), distal phloem (brown), periderm (dark green). **D.** Cell type classification after training by the Expert3 who identified the same cell types as the Expert2 but annotated different cells. **E.** Cell type classification after training by the Expert4 who identified 7 cell types: xylem vessels (green), xylem parenchyma (blue), cambium (yellow), phloem parenchyma (cyan), phloem poles (yellow), distal phloem (brown), periderm (dark green). **F.** Cell type classification after training by the Author who identified 9 indicated cell types.

All the 15 cell descriptors were used for the SVM trained cell type classification. I tested on three different images of wild type at 5 wpg which descriptors were more or less important by removing

one descriptor by one and qualitatively analysing the resulting classification. The results were too heterogeneous. Therefore, I decided to keep all the descriptors for the classification.

I also checked how the number of annotated cells influenced the quality of the classification. 5, 10 or 20 cells were annotated per cell type for 3 different images of wild type at 5 wpg. For all of them, the annotation of 20 cells per cell type resulted in the most optimal classification. More cells would not be possible to annotate for some tissues like xylem vessels, especially at earlier developmental stages when their cell number is too low.

The SVM models trained on one image were tested for the accuracy of classification on other images of wild type at 5 wpg. These models were also trained stepwise on these 3 images. The resulting classifications were of lower quality: the boundaries between tissues were more blurred, and a lot of obvious misclassifications happened. Therefore, SVM models trained on one image can be applied only to the very same image.

In the end of this optimisation, I successfully managed to classify six cell types of hypocotyl tissues: xylem vessels and parenchyma, cambium, phloem fibers and parenchyma, periderm.

In summary, with the help of "PlantSeg" and MGX, I established a quantitative histology protocol for the analysis of hypocotyl sections. Next, I wanted to challenge it with time-course mutant analysis.

3. Time-course analysis of radial growth in WT and *pxy* mutants using quantitative histology

To quantitatively characterize vascular cells and tissues morphogenesis, plants were grown in parallel, and their hypocotyls were collected at 3.5, 4, 4.5 and 5 wpg. WT was used for describing the dynamics of radial growth. *pxy-2* and *pxy-4* mutants were analysed in parallel too to test the advantages and limits of quantitative histology in detecting subtle differences in phenotypes. Hypocotyls were fixed and sectioned using a vibratome. Sections were cleared by ClearSee and double-stained by DirectYellow96 and Basic Fuchsin to reveal cell boundaries as well as cellulose and lignin content respectively [44]. First, different cell types were identified using qualitative characteristics of cell morphology and cell wall composition. Secondly, I automatically classified cells and quantified their production during radial growth. Thirdly, hypocotyl cells were analysed for their cell wall properties, morphology, and connectivity in a quantitative manner. Finally, I estimated tissue production during radial growth applying quantitative histology.

3.1. Qualitative analysis of WT hypocotyl tissues

WT hypocotyls grew radially for at least double of their radius between the first and the last time point of analysis (Figure 12I-L). At 3.5 wpg (Figure 12A, E, I), continuous cambium cylinder was already established and started to produce xylem in the proximal direction and phloem in the distal direction (Figure 12A) [47] [48]. Cambium cells were organised in cell files aligned to the radial axis (Figure 12A1). It was still possible to observe metaxylem that had formed before the initiation of radial growth (Figure 12E, E1). A high content in lignin allowed to distinguish xylem vessels from xylem parenchyma (Figure 12I, I1).

At 4 wpg, more vascular tissues were produced (Figure 12B, F, J). Phloem parenchyma cells had expanded, while phloem sieve elements and companion cells organised themselves in phloem poles. The latter could be distinguished by their smaller cell size and agglomeration in islands (Figure 12B, B1). Cortex and epidermis detached (* in Figure 12B) leaving place for periderm growth. Also called cork cambium, it is composed of the phellogen, a stem cell niche producing phelloderm proximally and phellem distally [32]. Phellem is lignified and interestingly, Basich Fuchsin staining showed that the lignification starts in anticlinal cell walls (Figure 12F1). DirectYellow96 staining was only visible in the phelloderm and the phellogen but not in the phellem (Figure 12J1), although phellem is supposed to contain cellulose [32]. This peculiarity indicates an artefact of the double-staining, because the single-staining controls with DirectYellow96 showed cellulose staining in phellem cells (data not shown here).

At 4.5 wpg (Figure 12C, G, K), more vascular tissues were produced. This is the time when tissue gaps at the phloem periphery appeared (Figure 12C1). These gaps are also characteristic of paraffin- [49] and plastic-embedded [32] hypocotyls sectioned with microtome, but the gaps in all three techniques take different shapes suggesting that this is a technical artefact and not an anatomical characteristic of *Arabidopsis* hypocotyls. At this developmental stage, phloem fibres started to differentiate and acquire their characteristic lignified cell walls (Figure 12G1). Two stem cell niches are active at this time-point: the vascular cambium positioned at the half-way along the radial axis from organ periphery to the hypocotyl centre and the cork cambium positioned at the periphery [32]. Therefore, phloem and phelloderm met somewhere at the inner border of periderm (Figure 12K1). So far, an observer could distinguish this border between two stem cell niches by looking at the cell size. Indeed, vascular phloem parenchyma expands towards the periphery of the section, therefore the boundary between phloem and phelloderm can be set where cells reach their maximum size before decreasing in size again when moving distally.

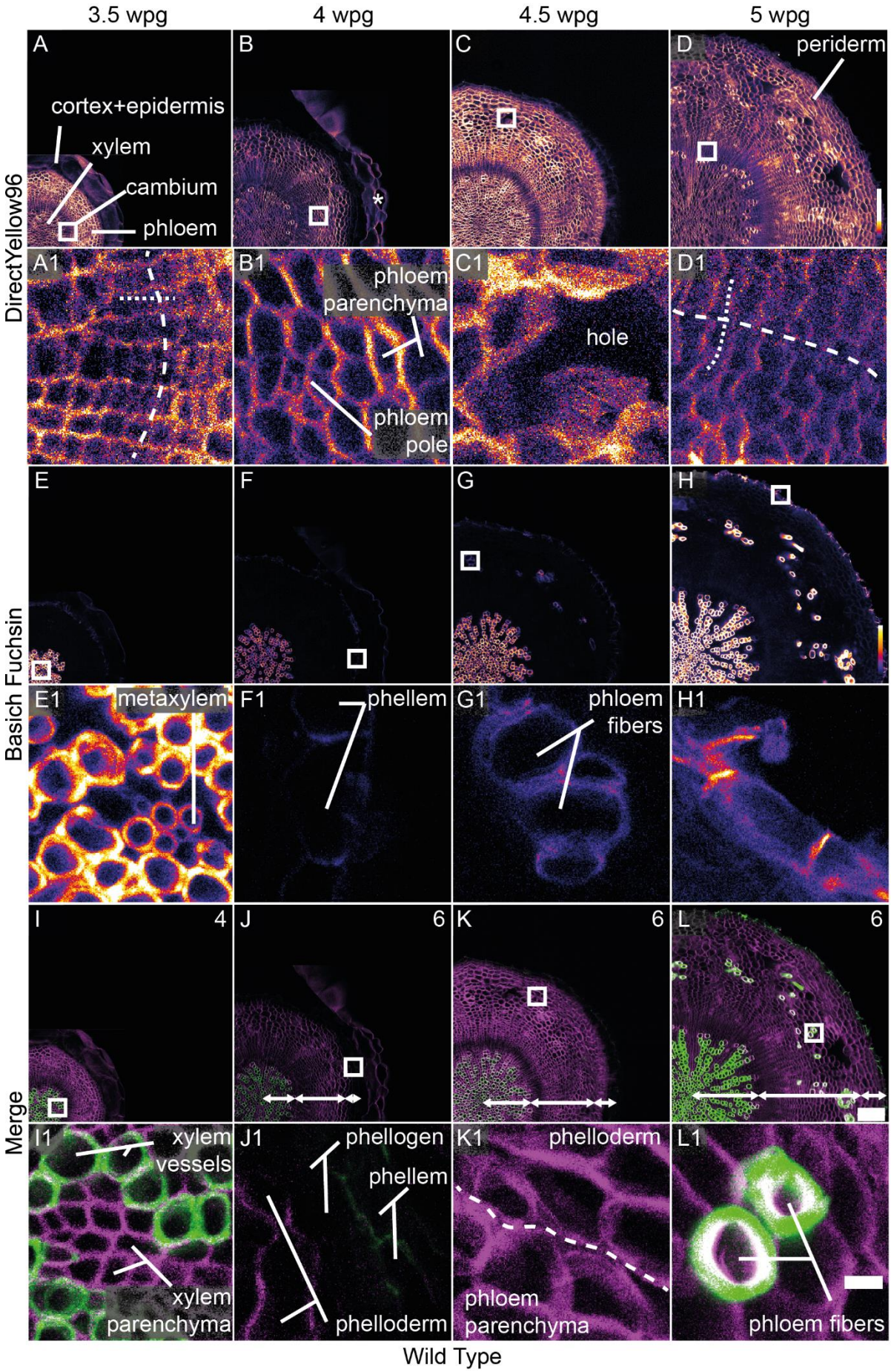
3.5 wpg
4 wpg
4.5 wpg
5 wpg
DirectYellow96
Basich Fuchsin
Merge
A
cortex+epidermis
xylem
cambium
phloem
B
C
D
periderm
A1
B1
phloem parenchyma
phloem pole
C1
hole
D1
E
F
G
H
E1
metaxylem
F1
phellem
G1
phloem fibers
H1
I
4
J
6
K
6
L
6
I1
xylem vessels
xylem parenchyma
J1
phellogen
phellem
phelloderm
K1
phelloderm
phloem parenchyma
L1
phloem fibers
Wild Type

Figure 12. Cell and tissue morphogenesis during radial growth. Hypocotyl transversal sections at 3.5 weeks post-germination (wpg) (**A, E, I**), 4 wpg (**B, F, J**), 4.5 wpg (**C, G, K**) and 5 wpg (**D, H, L**) stained with DirectYellow96 (cellulose) (**A-D**) and Basic Fuchsin (lignin) (**E-H**). **I-L**. **I-L**. Merge of **A** and **E** (**I**), **B** and **F** (**J**), **C** and **G** (**K**), **D** and **H** (**L**) with DirectYellow96 in magenta and Basic Fuchsin in green. In the upper right corner, the number of analysed plants is indicated. The double-arrows indicate xylem, cambium with phloem and periderm from the section centre to the periphery respectively. **A1-L1.** Magnifications of the white squares respectively in **A-L**. **A1**, **D1**. Cambium cells are organised in radial cell files (dotted line). Cambium is circumferentially symmetrical (dashed line). **B1**. Phloem cells. **C1**. A hole in phloem tissue. **E1**. Central xylem. Small cells are metaxylem. **F1**. Lignification of anticlinal cell walls of phellem. **G1**. Lignification of future phloem fibers. **H1**. One cell layer of phellem with residuals of the second second cell layer. **I1**. Xylem parenchyma in magenta and xylem vessels in green and white. **J1**. Periderm with phelloderm and phellogen in magenta and phellem in green. **K1**. The supposed boundary between distal phloem and phelloderm (dashed line). **L1**. Mature phloem fibers in green, white and magenta. * in **B** indicates the detaching cortex and epidermis. The scalebar in **L** corresponds to 100 µm and is applicable for **A-L**. The scalebar in **L1** corresponds to 10 µm and is applicable for **A1-L1**. The calibration bar in **D** is applicable for **A-D** and **A1-D1**. The calibration bar in **H** is applicable for **E-H** and **E1-H1**.

At 5 wpg (Figure 12D, H, L), radial growth reached the final stage before bolting and xylem-II formation (Figure 3B) [47]. Cambium maintained its radial and circumferential symmetry throughout all time-points (Figure 12A1, D1). In other words, cambium is a ring-like structure composed of radially aligned cell files. At 5 wpg, phloem fibers reached maturity by forming crystalline cellulose in the secondary cell wall (Figure 12L1) [29]. Moreover, phloem fibers formed a more irregular pattern compared to other tissues (Figure 12H). The phellem got lignified at all its cell walls, however only one of its cell layers could be visualised with the current histology technique (Figure 12H1) [32].

In summary, except for a few cell layers of the periderm, I managed to identify all known cell types of the hypocotyl during radial growth. The double cellulose-lignin staining combined with ClearSee and confocal microscopy provided a high resolution anatomical map at the cellular level and allowed to distinguish subtypes of lignified cells.

3.2. Qualitative analysis of hypocotyl tissues in *pxy-2* and *pxy-4*

I was interested in comparing the WT situation with two *pxy* alleles in a timely resolved manner. *pxy* mutants presented similar overall radial growth compared to WT (Figure 12I-L, Figure 13I-L, Figure 14I-L). However, cortex and epidermis were detached only partially at 4 wpg (Figure 12B, Figure 13B, C, Figure 14B, C). The cambium maintained its radial symmetry but lost its circumferential symmetry in *pxy* mutants (Figure 12A1, D1, Figure 13A1, D1, K1, Figure 14A1, D1, K1). The xylem pattern was affected in the mutants (Figure 12E-H, Figure 13E-H, Figure 14E-H). The radial and circumferential distances between xylem vessels were larger in *pxy* mutants compared to WT (Figure 12I1, Figure 13-F1, G1, Figure 14F1, G1). Metaxylem showed a similar morphology of small, round, lignified cells in

the middle of xylem for all genotypes (Figure 12E1, Figure 13E1, Figure 14E1). However, xylem vessels and parenchyma had different and irregular morphologies in *pxy* mutants (Figure 12I1, Figure 13I1, J1, Figure 14I1, J1). Xylem seemed to occupy a bigger relative space while phloem occupied a smaller one in *pxy* mutants compared to WT (Figure 12I-L, Figure 13I-L, Figure 14I-L). Phloem poles and parenchyma had a similar morphology in all genotypes at 4 wpg (Figure 12B, B1, Figure 13B, B1, Figure 14B, B1), but phloem got disorganized in *pxy* mutants at later stages (Figure 12D, Figure 13D, Figure 14D). The boundary between phloem and phelloderm became difficult to identify in *pxy-2* and *pxy-4* (Figure 12K1, Figure 13C1, Figure 14C1). Phloem fibres were successfully formed in the mutants but started to differentiate at 5 wpg instead of 4.5 (Figure 12G1, L1, Figure 13G, L1, Figure 14G, L1). Moreover, the periderm appeared larger in *pxy* mutants compared to WT (Figure 12L, Figure 13L, Figure 14L). At 5 wpg, phellem lignification was disrupted unequally over radial axis in the mutants: sometimes in a cell file, sometimes by patches (Figure 12H1, L, Figure 13H1, L, Figure 14H1, L).

In summary, I observed major differences in cell differentiation rate and tissue production, in cell and tissue morphogenesis comparing *pxy* mutants with WT, but no prominent qualitative differences comparing *pxy-2* with *pxy-4*. Moreover, the identified characteristics should be quantified to support these results statistically.

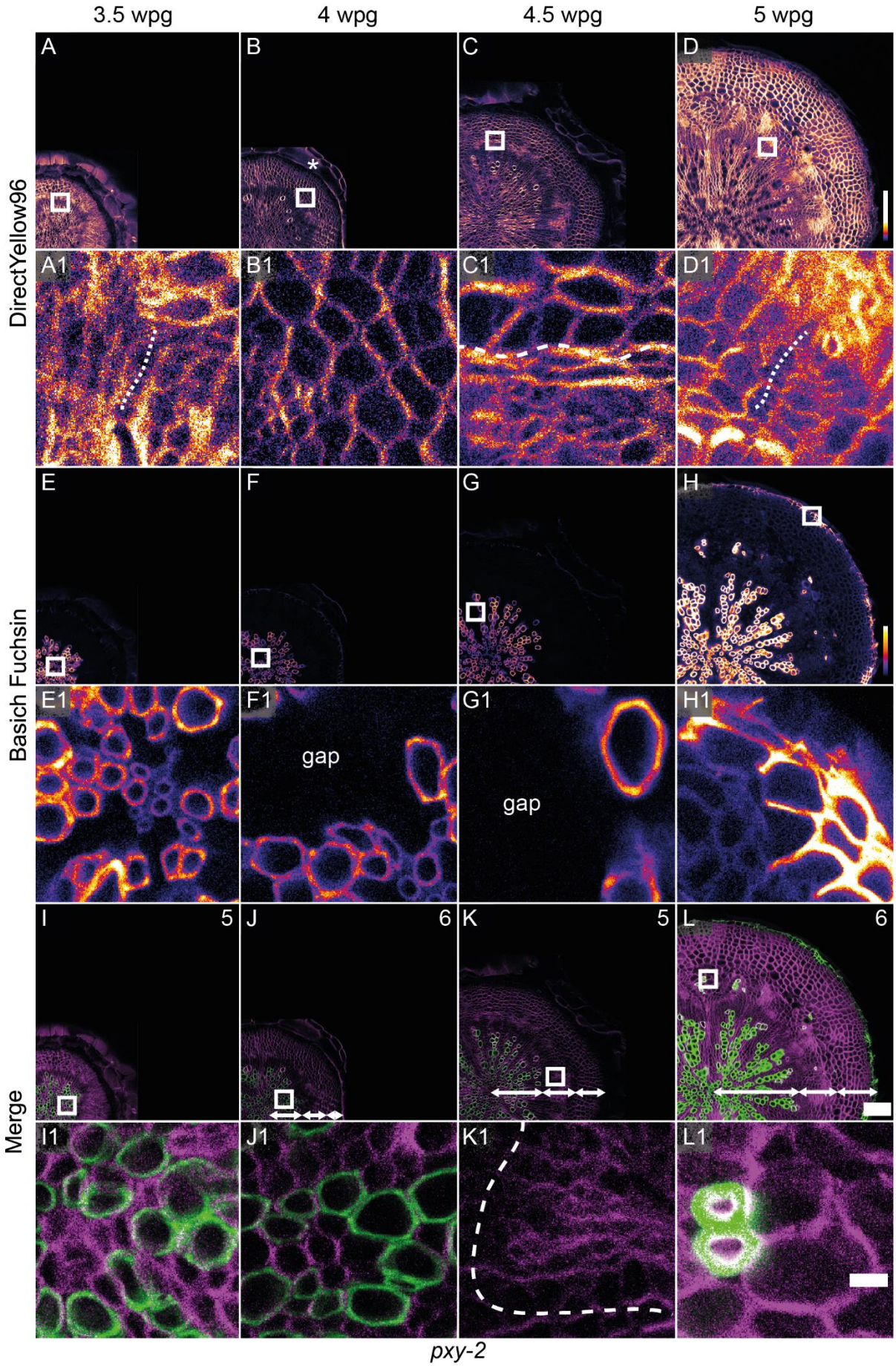
3.5 wpg
4 wpg
4.5 wpg
5 wpg
DirectYellow96
Basich Fuchsin
Merge
A
B
C
D
A1
B1
C1
D1
E
F
G
H
E1
F1
G1
H1
gap
gap
I
J
K
L
5
6
5
6
I1
J1
K1
L1
pxy-2

Figure 13. <u>Cell and tissue morphogenesis during radial growth in *pxy-2*</u>. *pxy-2* hypocotyl transversal sections at 3.5 weeks post-germination (wpg) (**A, E, I**), 4 wpg (**B, F, J**), 4.5 wpg (**C, G, K**) and 5 wpg (**D, H, L**) stained with DirectYellow96 (cellulose) (**A-D**) and Basic Fuchsin (lignin) (**E-H**). **I-L**. Merge of **A** and **E** (**I**), **B** and **F** (**J**), **C** and **G** (**K**), **D** and **H** (**L**) with DirectYellow96 in magenta and Basic Fuchsin in green. In the upper right corner, number of analysed plants. **A1-L1.** Magnifications of respective white squares in **A-L**. **A1**, **D1**. Cambium cells are organised in radial cell files (dotted line). **B1**. Phloem cells. **C1**. The supposed boundary between phloem and phelloderm (dashed line). **E1**. Central xylem. Small cells are metaxylem. **F1**. Gaps between xylem vessels along the radial axis. **G1**. Gaps between xylem vessels along circumferential axis. **H1**. Disorganised lignification of phellem. **I1**, **J1**. Xylem parenchyma in magenta and xylem vessels in green white and magenta. **K1**. Loss of the circumferential symmetry in cambium. **L1**. Mature phloem fibers in green, white and magenta on the left. Supposed boundary between phloem phelloderm on the right. * in **B** indicates the non-detached cortex and epidermis. The double-arrows in **L** indicate xylem, cambium with phloem and periderm from the section centre to the periphery respectively. The scalebar in **J-L** corresponds to 100 µm and is applicable for **A-L**. The scalebar in **L1** corresponds to 10 µm and is applicable for **A1-L1**. The calibration bar in **D** is applicable for **A-D** and **A1-D1**. The calibration bar in **H** is applicable for **E-H** and **E1-H1**.

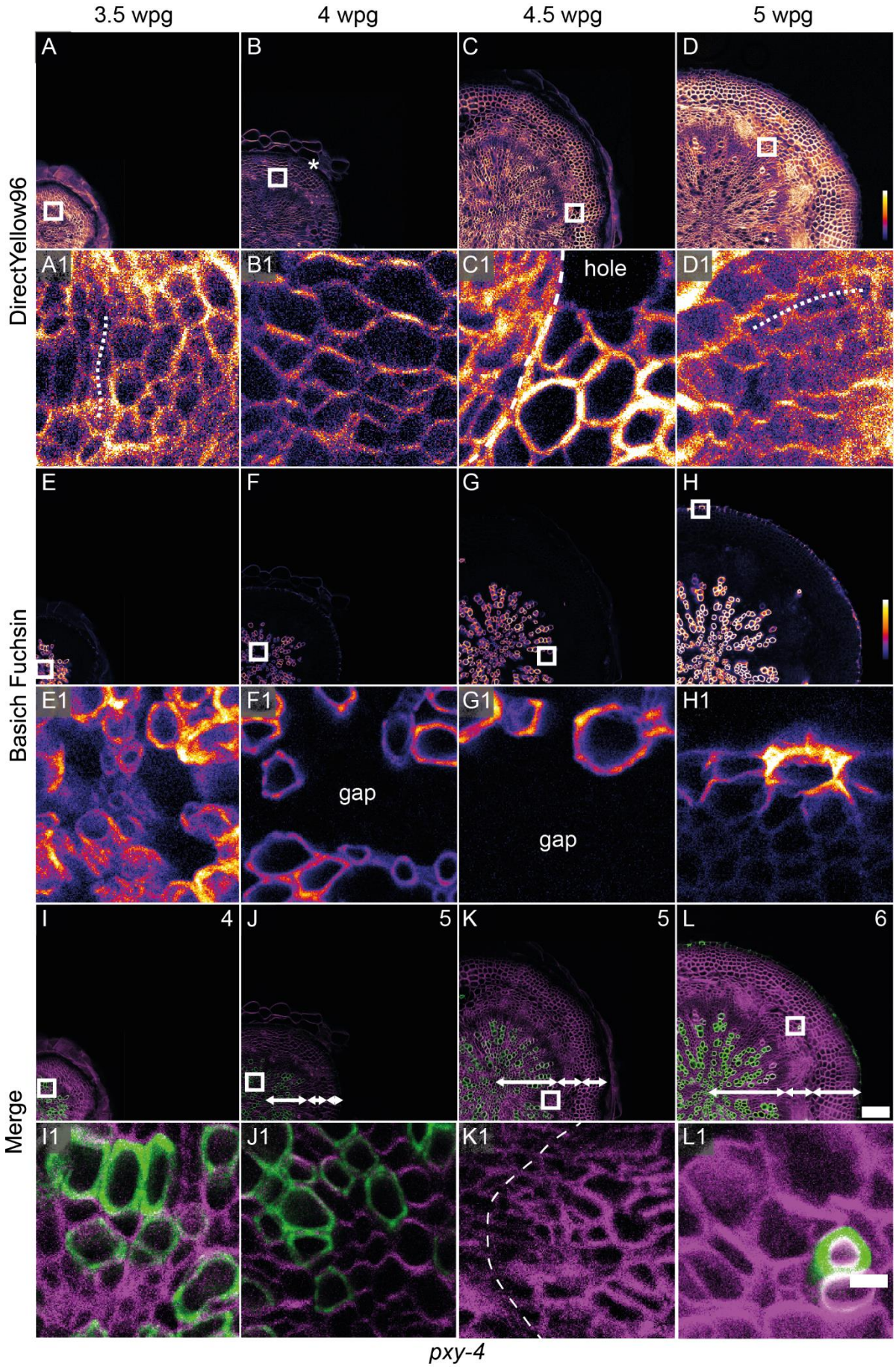
3.5 wpg
4 wpg
4.5 wpg
5 wpg
DirectYellow96
Basich Fuchsin
Merge
A
B
C
D
A1
B1
C1
D1
hole
E
F
G
H
E1
F1
G1
H1
gap
gap
I
J
K
L
4
5
5
6
I1
J1
K1
L1

pxy-4

Figure 14. Cell and tissue morphogenesis during radial growth in *pxy-4*. *pxy-4* hypocotyl transversal sections at 3.5 weeks post-germination (wpg) (**A, E, I**), 4 wpg (**B, F, J**), 4.5 wpg (**C, G, K**) and 5 wpg (**D, H, L**) stained with DirectYellow96 (cellulose) (**A-D**) and Basic Fuchsin (lignin) (**E-H**). **I-L**. Merge of **A** and **E** (**I**), **B** and **F** (**J**), **C** and **G** (**K**), **D** and **H** (**L**) with DirectYellow96 in magenta and Basic Fuchsin in green. In the upper right corner, number of analysed plants. **A1-L1.** Magnifications of respective white squares in **A-L**. **A1**, **D1**. Cambium cells are organised in radial cell files (dotted line). **B1**. Phloem cells. **C1**. Supposed boundary between phloem and phelloderm. A hole in phloem tissue. **E1**. Central xylem. Small cells are metaxylem. **F1**. Gaps between xylem vessels along the radial axis. **G1**. Gaps between xylem vessels along circumferential axis. **H1**. Disorganised lignification of phellem. **I1**, **J1**. Xylem parenchyma in magenta and xylem vessels in green and white. **K1**. Loss of the circumferential symmetry in cambium. **L1**. Mature phloem fibers in green, white and magenta on the right. * in **B** indicates the non-detached cortex and epidermis. The double-arrows in **J-L** indicate xylem, cambium with phloem and periderm from the section centre to the periphery respectively. The scalebar in **L** corresponds to 100 µm and is applicable for **A-L**. The scalebar in **L1** corresponds to 10 µm and is applicable for **A1-L1**. The calibration bar in **D** is applicable for **A-D** and **A1-D1**. The calibration bar in **H** is applicable for **E-H** and **E1-H1**.

3.3. Quantification of cell production during radial growth

WT and *pxy* mutants were analysed qualitatively so far. A quantitative and unbiased analysis of hypocotyl tissues will help to reveal subtle differences between radial growth dynamics of these genotypes. The acquired images were analysed applying the quantitative histology protocol. Cell types were mapped (Figure 15A-L) and the cell number per tissue was determined (Figure 15M). In overall, SVM cell type classification (Figure 15A-L) reproduced the qualitative tissue classification by an expert eye (Figure 12A, D, I-L, 13I-L, 14I-L). Xylem vessels tissue was organised less stereotypically along circumferential axis in *pxy* mutants (Figure 15E-L, green) compared to WT (Figure 15A-D, green). At the final stage of development, cambium got more mixed with xylem vessels and parenchyma in *pxy* mutants compared to wild type (Figure 15D, H, L, green, blue, yellow). Actually, I had difficulties to properly distinguish xylem parenchyma, cambium and phloem parenchyma from each other in *pxy* mutants based on cell morphology and position in the tissues. Nevertheless cambium "wavy" circumferential pattern could be noticed in *pxy* mutants qualitatively (Figure 13K1, Figure 14K1) and quantitatively after cell type classification (Figure 15H, L, yellow). Therefore, cell type classification SVM model looked like efficient enough to classify cell types in WT and *pxy* mutants. Although there were some contaminations between neighbouring tissues.

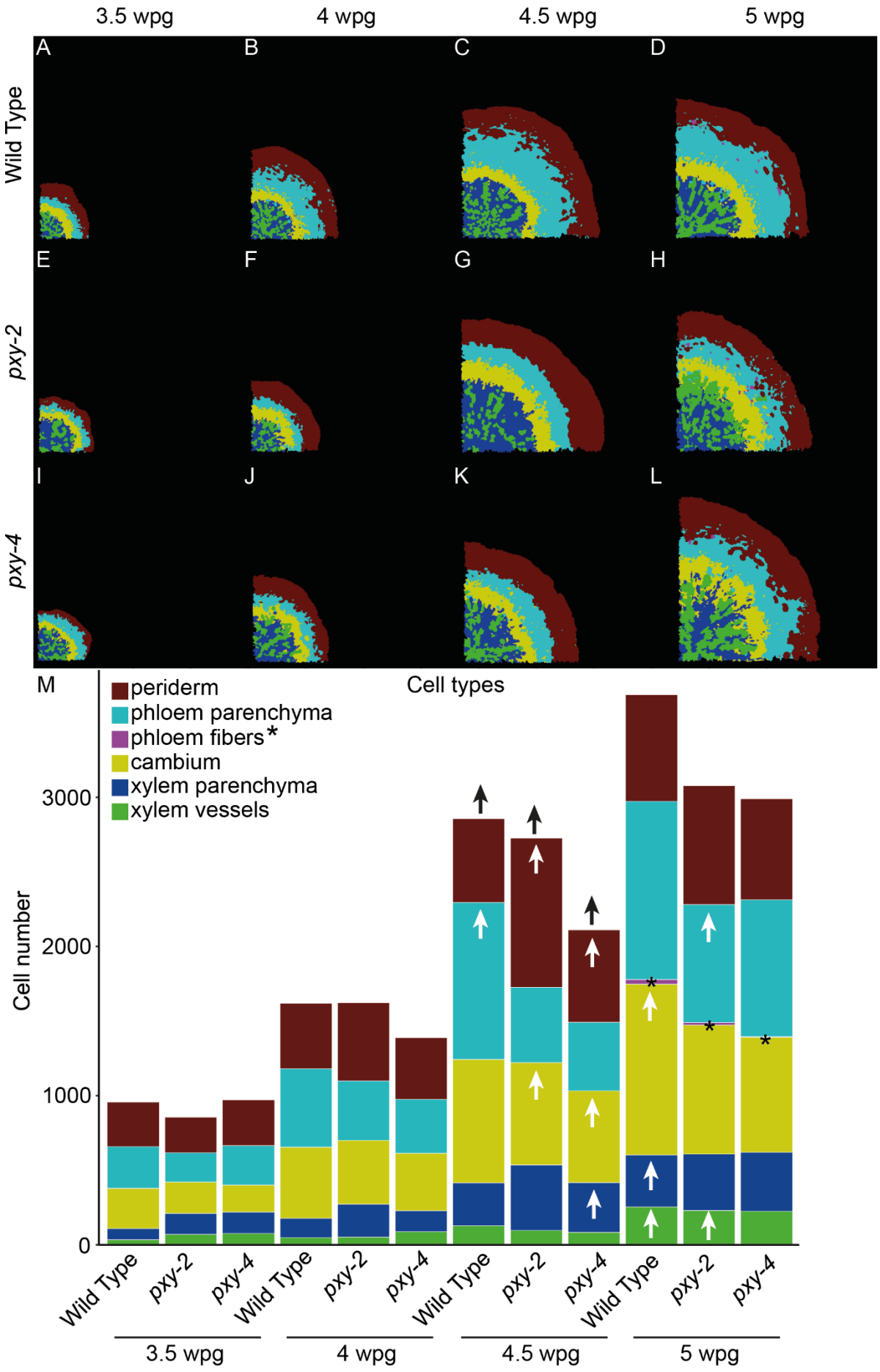
3.5 wpg
4 wpg
4.5 wpg
5 wpg
A
B
C
D
Wild Type
E
F
G
H
pxy-2
I
J
K
L
pxy-4
M
periderm
phloem parenchyma
phloem fibers*
cambium
xylem parenchyma
xylem vessels
Cell types
Cell number
3000
2000
1000
0
Wild Type
pxy-2
pxy-4
3.5 wpg
4 wpg
4.5 wpg
5 wpg

Figure 15. Cell type classification in wild type and *pxy* mutants hypocotyls during radial growth. A-D. Wild type. **E-H.** *pxy-2*. **I-L.** *pxy-4*. **A, E, I.** 3.5 weeks post-germination (wpg). **B, F, J.** 4 wpg. **C, G, K.** 4.5 wpg. **D, H, L.** 5 wpg. **M.** Cell number per time point, genotype and cell type with n = 3 plants for each. "*" corresponds to the first appearance of phloem fibers. Arrows indicate the first significant increase ($p < 0.05$ after Kruskal-Wallis test) compared to 3.5 wpg. The colour code legend in M applies to A-L too.

Object alignments can be easier visualised in Cartesian coordinates than in polar ones. To do this for hypocotyl cells one needs to plot their radial coordinates against the circumferential ones. Therefore, the polar tissue organization was transformed to a Cartesian one thus facilitating tissue pattern identification (Figure 16). Here, radial growth as a result of cell proliferation was observed in the increase of cell density in both radial and circumferential directions. Density variation over time appeared tightly correlated comparing cambium and phloem cells (Figure 16A-D, yellow and cyan respectively), while xylem cell density increased much slower (Figure 16A-D, green and blue). At 3.5 wpg, the periderm showed a similar cell density compared to cambium and phloem (Figure 16A, brown) but, later, it increased at its periphery while remaining less dense proximally (Figure 16B-D, brown). At late stages of development, phloem parenchyma organized partially in cell files and partially in clusters (Figure 16C, D, cyan). These clusters would correspond to phloem poles, where additional cell proliferation takes place [reference]. *pxy* mutants presented a similar radial organization of hypocotyl tissues (Figure 16E-L) as WT (Figure 16A-D). Although there were some differences in terms of tissue proportions, boundaries, and cell alignment. Phloem appeared to lose in relative thickness to periderm in *pxy* mutants starting from 4 wpg (Figure 16-B-D, F-H, J-L, cyan and brown respectively). Cambium was not organized as a circular band like in wild-type (Figure 16-A-D, yellow) but reached into xylem starting from 4 wpg (Figure 16-F-H, J-L, yellow). Neither xylem, nor phloem organized in cell files (Figure 16F-H, J-L, green, blue and cyan) as seen in WT (Figure 16B-D, green, blue and cyan). Therefore, coordinate transformation of hypocotyl cells brought another qualitative perspective into tissue topology. It revealed the dynamics in cell density variation across different tissues during radial growth. The coordinate transformation also revealed cell alignment patterns – the analysis often used for vascular mutants phenotyping.

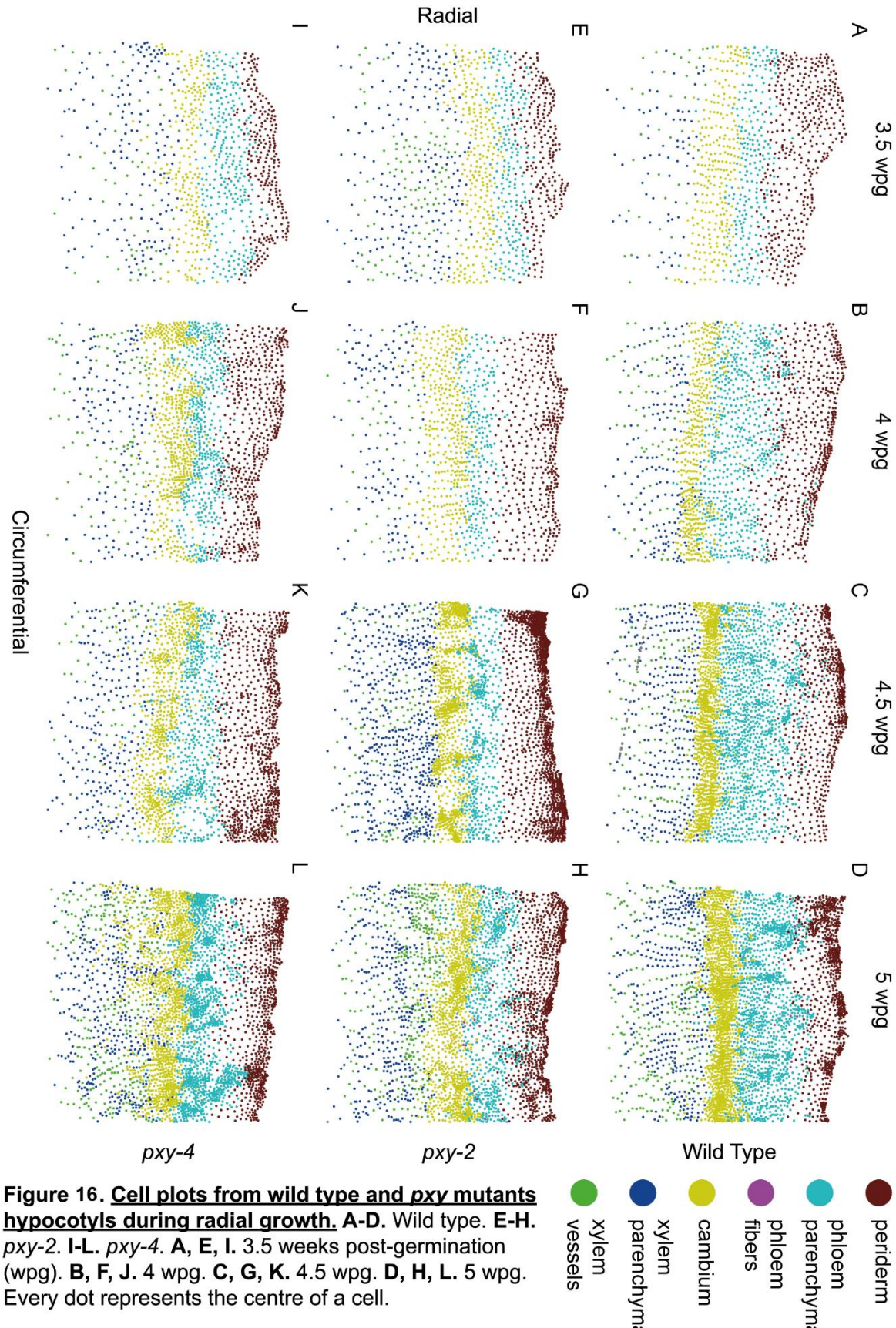

Figure 16. <u>Cell plots from wild type and *pxy* mutants hypocotyls during radial growth.</u> A-D. Wild type. **E-H.** *pxy-2*. **I-L.** *pxy-4*. **A, E, I.** 3.5 weeks post-germination (wpg). **B, F, J.** 4 wpg. **C, G, K.** 4.5 wpg. **D, H, L.** 5 wpg. Every dot represents the centre of a cell.

When analysing radial growth, one usually questions how many cells were produced at different time points. Quantitative histology allows to make this estimation. I took the number of cells per cell type of every analysed hypocotyl and calculated the mean between three plants for every genotype and time-point (Figure 15M). Looking at the dynamics of radial growth, there was a significant increase in the total cell number at 4.5 wpg for all genotypes (Figure 15M, black arrows). Phloem parenchyma cell number significantly increased in wild type at the same developmental stage, however the cell number in other tissues increased only at the last time point like for the cambium, the phloem, and the xylem or not at all like for the periderm (Figure 15M, white arrows for wild type). Phloem fibres appeared for the first time only at the last time point of development in all genotypes (Figure 15M, asterisks). Cambium and periderm cell number increased earlier in *pxy* mutants compared to WT (Figure 15M, white arrows at 4.5 and 5 wpg, yellow and brown). *pxy-2* mutants were retarded for a phloem parenchyma cell number increase, while *pxy-4* failed in additional phloem parenchyma cells production (Figure 15M, white arrows for 4.5 and 5 wpg, cyan). These last two observations are in line with the qualitative assessment of cell number and density using Cartesian cell plots (Figure 16). Indeed, *pxy* mutants produced phloem cells slower while periderm cells – faster. Xylem cell production appeared also to be affected in *pxy* mutants but in a less prominent manner (Figure 15M, white arrows for 4.5 and 5 wpg, green and blue). Importantly, no significant difference was found comparing cell numbers from different genotypes at any given time point.

In summary, quantitative histology allowed automatic cell type classification and considered every single cell without ignoring the tissue context. However still no substantial differences were observed comparing two *pxy* mutant alleles by a qualitative assessment of tissue shapes or looking at the cell number.

3.4. Quantitative analysis of hypocotyl cells

The quantitative histology can be pushed further by looking at the properties of every single cell and reveal more quantitative differences unseen by a naked eye. Thanks to double cell wall staining, I was able to roughly estimate relative cellulose and lignin content. Cell morphology can be estimated by area, perimeter, major axis, minor axis, aspect ratio, circularity, rectangularity and lobeyness. Tissue topology can be estimated by cell incline angle, degree and betweenness centrality. I looked at these thirteen cell descriptors for every tissue type and compared them between different time points and genotypes. As all these descriptors were used for cell type classification, I did not compare them quantitatively within the same plants. However, I estimated their variation within the

same plants qualitatively by looking at their heat maps generated for the corresponding hypocotyl sections.

3.4.1. Cell wall properties

Hypocotyl sections were double stained with DirectYellow96 and Basic Fuchsin which are specific to cellulose and lignin respectively. The resulting fluorescence signal from DirectYellow96 was used to identify cell boundaries. However, both DirectYellow96 and Basic Fuchsin can also be used to assess cellulose and lignin content respectively (Figure 17, Figure 18). Although, the signal-content correlation is debatable and prone to microscopic artefacts due to technical differences in sectioning and staining. Indeed, I saw a high variation in staining between sections of the same time points and genotypes. Therefore, only relative cell wall properties could be considered within a single image. I analysed cell wall staining differences within the same sections but not between different samples.

Over the whole analysed plant life, xylem and phloem showed a higher cellulose staining than cambium or periderm. There were also hotspots of cells with high cellulose staining in proximal xylem and distal phloem (Figure 17A-D). In *pxy* mutants, this polarity was disrupted. High cellulose staining and hotspots were observed almost everywhere in the section. The only tissue that maintained consistently low cellulose staining in *pxy* mutants was the periderm (Figure 17E-L). At 3.5 wpg, *pxy* mutants formed a high cellulose staining front at distal phloem, as in WT however the xylem and cambium cellulose staining patterns were different (Figure 17A, E, I). At 4 and 4.5 wpg, a low cellulose staining band characteristic of the WT cambium (Figure 17B, C) was established in *pxy* mutants (Figure 17F, G, J, K). But it acquired its wavy pattern and/or fragmented pattern towards 5 wpg (Figure 17H, L). At this stage, xylem and cambium of *pxy* mutants were composed of circumferentially aligned sectors of high and low cellulose content (Figure 17H, L), while these sectors could be distinguished in a less pronounced way in WT (Figure 17D).

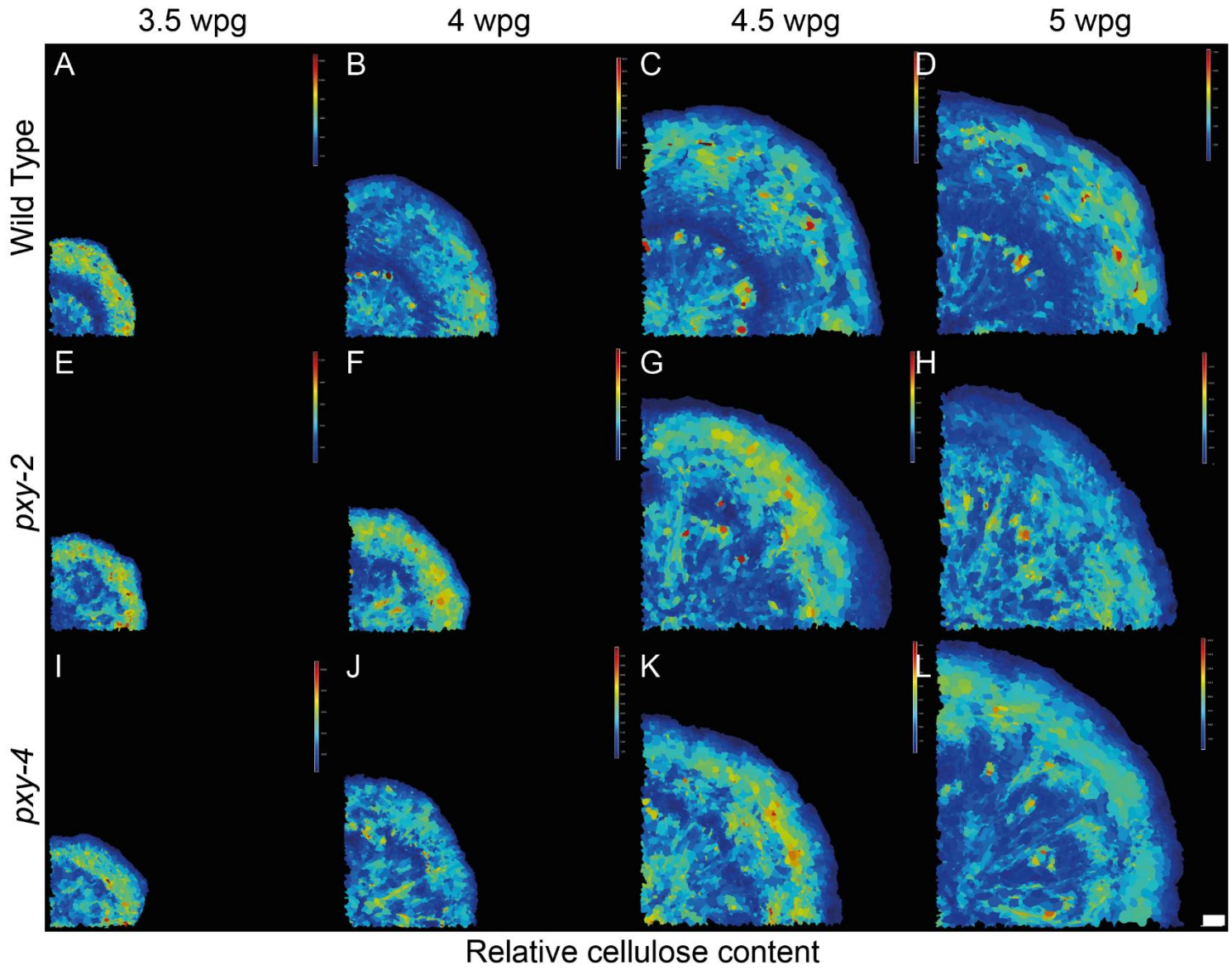

Figure 17 . <u>Relative cellulose content per cell in wild type and *pxy* mutants hypocotyls during radial growth</u>. A-D. Wild type. **E-H.** *pxy-2*. **I-L.** *pxy-4*. **A, E, I.** 3.5 weeks post-germination (wpg). **B, F, J.** 4 wpg. **C, G, K.** 4.5 wpg. **D, H, L.** 5 wpg. The values in the calibration bar correspond to the total signal normalised by cell area. The intensity ranges are different for every image. The scale bar in **L** corresponds to 50 µm and applies to the whole figure.

The intensity of lignin staining projected on cells (Figure 18) recapitulated the observations of raw microscopy images (Figure 12E-H, Figure 13E-H, Figure 14E-H). Contrary to cellulose staining projection (Figure 17), lignin staining projection did not seem to bring any new information on tissue lignification pattern. However, the heat maps allowed to identify more hotspots in *pxy* xylem and periderm (Figure 18-E-L, red cells) than in WT (Figure 18A-D). Lignin content was a valuable cell descriptor for automated cell type classification. Indeed, when it was removed from the SVM classifier, xylem vessels were confused with xylem parenchyma. At the same time, there was never any confusion when lignin staining remained in the classifier while other descriptors were removed. This suggests that lignin staining is critical to robustly distinguish xylem vessels from xylem parenchyma.

In summary, fluorescence intensity from cellulose and lignin staining was successfully projected on single cells and provided a new perspective on the tissue patterning and hotspots of extreme staining intensities.

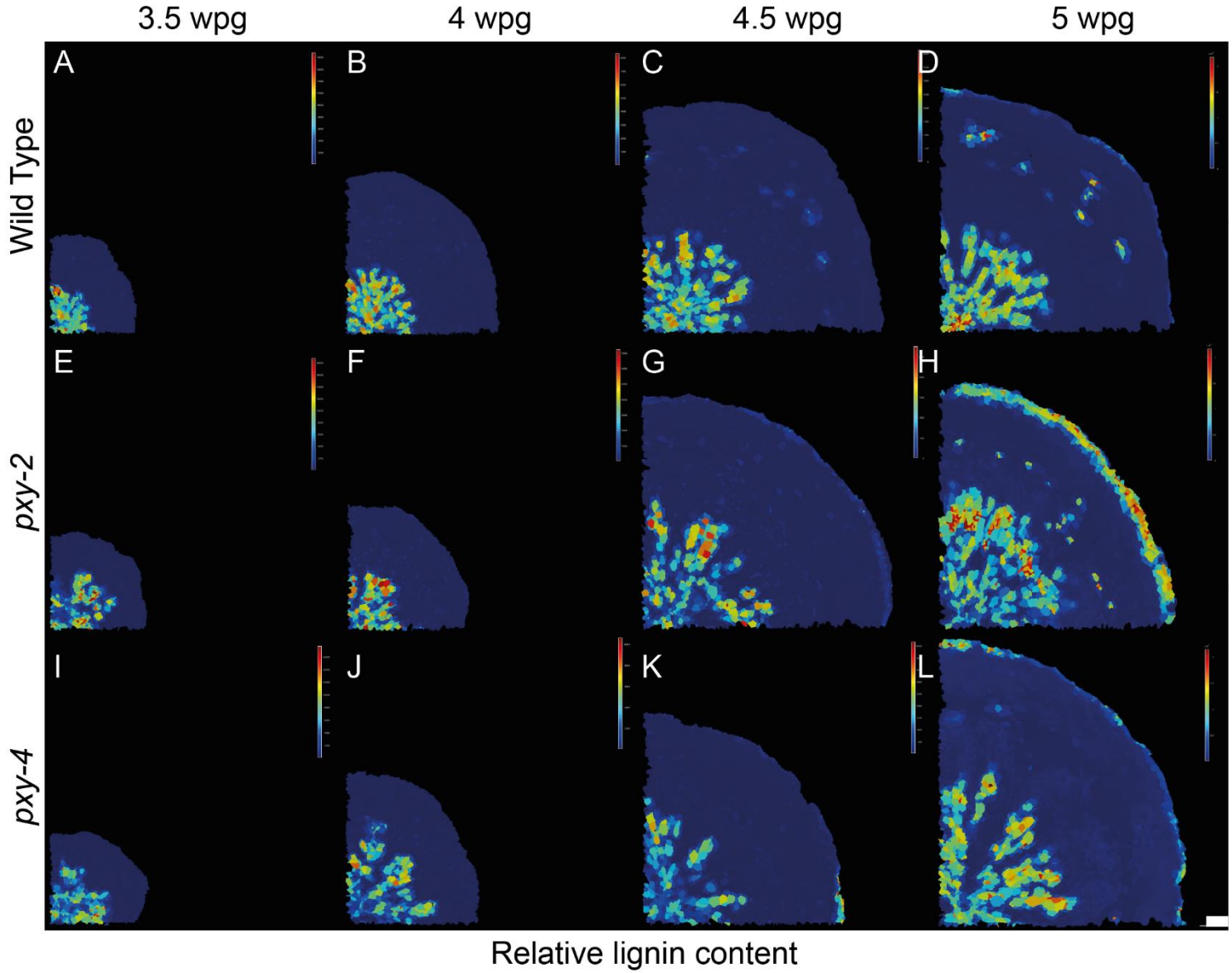

Figure 18. <u>Relative lignin content per cell in wild type and *pxy* mutants hypocotyls during radial growth</u>. A-D. Wild type. **E-H.** *pxy-2*. **I-L.** *pxy-4*. **A, E, I.** 3.5 weeks post-germination (wpg). **B, F, J.** 4 wpg. **C, G, K.** 4.5 wpg. **D, H, L.** 5 wpg. The values in the calibration bar correspond to the total signal normalised by cell area. The intensity ranges are different for every image. The scale bar in **L** corresponds to 50 µm and applies to all the figure.

3.4.2. Cell morphology

I quantified hypocotyl cell morphology by using primary geometrical measures like cell area, perimeter, major and minor axes. They also served me to calculate secondary geometrical measures like aspect ratio, circularity, rectangularity and lobeyness.

3.4.2.1. Cell area

The first and most common direct morphological measure is cell area. As I work with two-dimensional images, cell area represents the horizontal extension of hypocotyl cells (Figure 19, Figure 20).

During radial growth, there is a high level of cell production by stem cells but also an intense cell expansion in differentiating tissues. Indeed, cambium cell area fluctuated around the value of 30 μm^2 over time (Figure 20C). This can be observed in the heat maps where cambium was identified by a net band of the lowest area values (Figure 19B-D). Meanwhile xylem parenchyma cells increased by a factor of 1.5 in size from 3.5 to 4.5 wpg (Figure 20B), phloem parenchyma cell area gradually doubled from 3.5 to 5 wpg (Figure 20E) and periderm cells doubled in size from 3.5 to 4 wpg and then, tripled from 3.5 to 4.5 wpg (Figure 20F). Interestingly xylem vessels fluctuated around a value of 100 μm^2 (Figure 20A). The quantile of the highest values of the area of phloem parenchyma and periderm cells grew over time (Figure 20E, F). This is due to cell expansion of distal phloem and phelloderm cells. Indeed, I observed a high cell size band at the distal phloem-phelloderm boundary (Figure 19B-D). The quantile of high values of the area of phloem parenchyma (Figure 20E) would correspond to the distal phloem while the same quantile of the periderm area (Figure 20F) would correspond to the phellogen (Figure 19B-D).

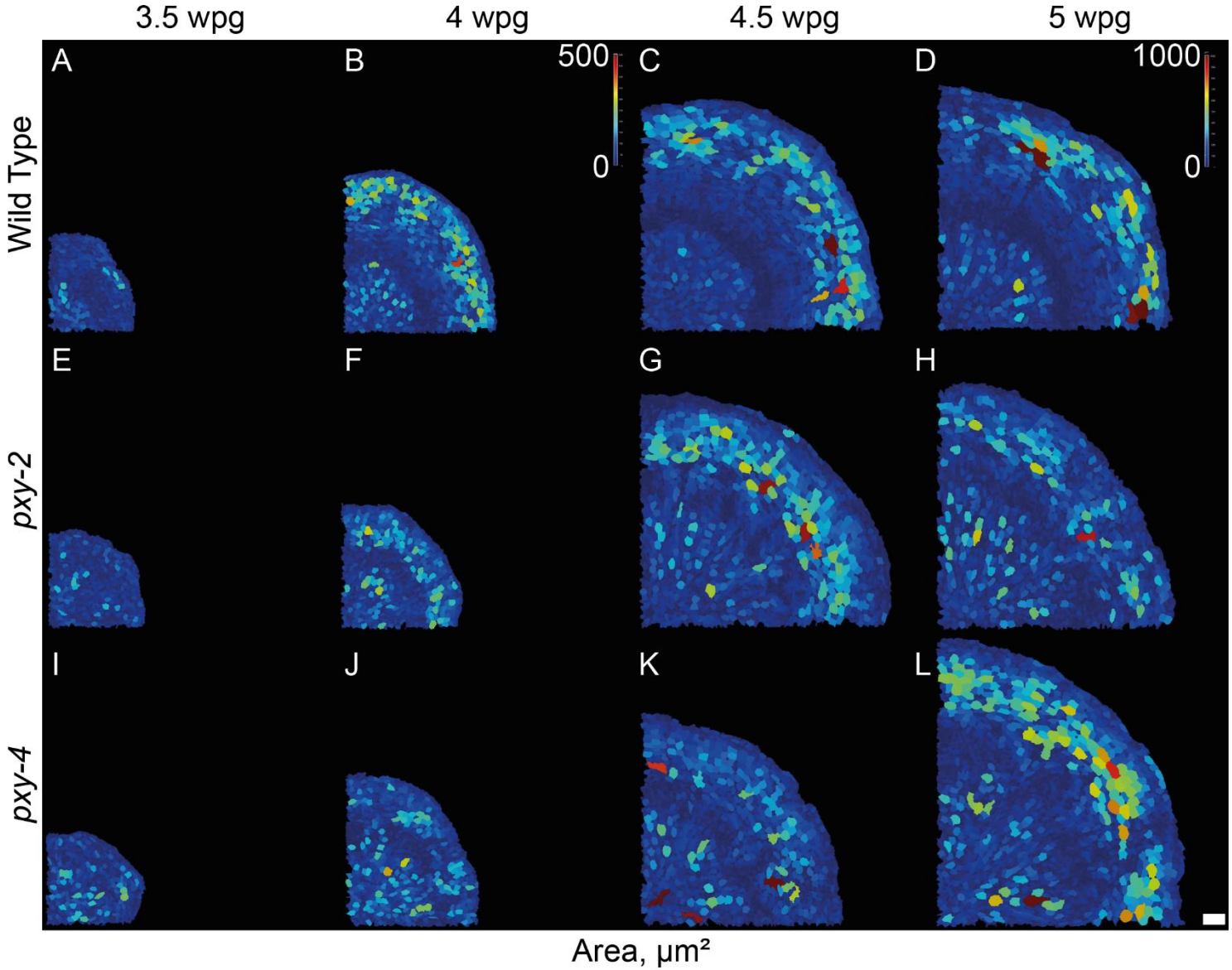

Figure 19 . <u>Cell area in wild type and *pxy* mutants hypocotyls during radial growth</u>. **A-D.** Wild type. **E-H.** *pxy-2*. **I-L.** *pxy-4*. **A, E, I.** 3.5 weeks post-germination (wpg). **B, F, J.** 4 wpg. **C, G, K.** 4.5 wpg. **D, H, L.** 5 wpg. The calibration bar in **B** gives the color code for **A, B, E, F, I** and **J**. The calibration bar in **D** gives the color code for **C, D, G, H, K** and **L**. The values of the calibration bars are indicated in µm². The scale bar in **L** corresponds to 50 µm and applies to the whole figure.

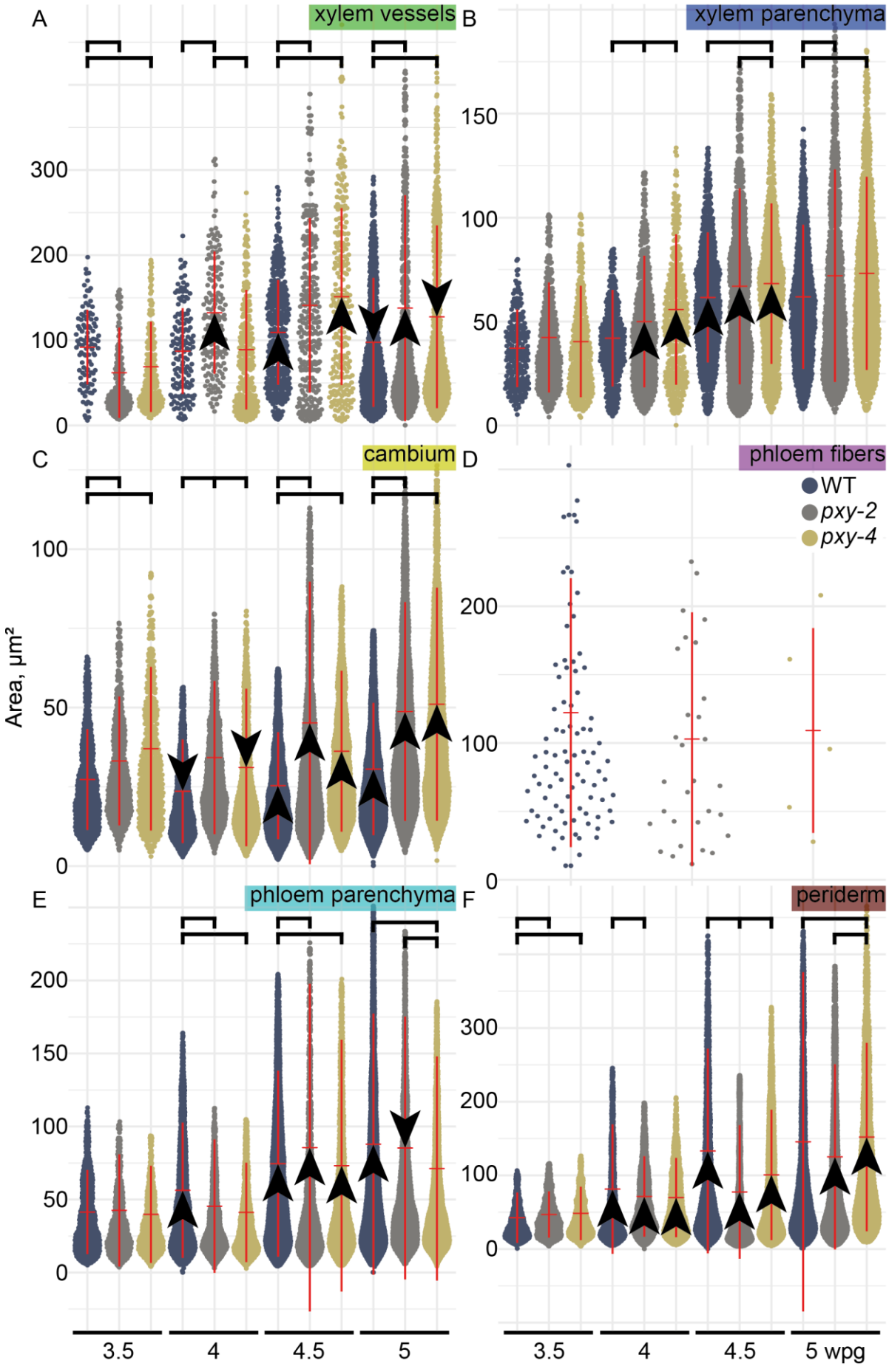
A
xylem vessels
B
xylem parenchyma
C
cambium
D
phloem fibers
WT
pxy-2
pxy-4
E
phloem parenchyma
F
periderm
Area, µm²
0
50
100
150
200
300
3.5
4
4.5
5
5 wpg

Figure 20. <u>Quantification of cell area</u>. Xylem vessels (**A**), xylem parenchyma cells (**B**), cambium cells (**C**), phloem fibers (**D**), phloem parenchyma cells (**E**) and periderm cells (**F**) were extracted from image segmentations and the area was measured. The time points are indicated in the lower part of the image. The y-axa correspond to area in µm² as indicated in the left part of the Figure. The genotypes are colour-coded and the legend is in the upper-left part of the Figure. Cell types are indicated in the upper-right corners of every graph. Red horizontal bar in the middle of a violin-shaped dot plot indicates the mean, the vertical red bar indicates +/- standard deviation from the mean. The outliers were removed from the dotplot but were included into the calculation of the mean and the standard deviation. Arrows pointing up or down indicate a significant increase or decrease respectively in mean area for the corresponding genotype compared to the previous time point (p.value < 0.05 after Kruskal-Wallis test on a single genotype group followed by a post-hoc pairwise Dunn test with Bonferroni correction and p.value < 0.05). Square brakets indicate a significant difference after a Kruskal-Wallis test on the single time point group followed by a post-hoc pairwise Dunn test with Bonferroni correction and p-value < 0.05. In the absence of arrows or square brakets, the difference is not significant with p-value > 0.05 after a Kruskal-Wallis test.

Cambium cells in *pxy* mutants were larger than cambium cells in WT (Figure 20C). The low cell size band was not continuous in *pxy* mutants, had a variable thickness and showed a wavy pattern (Figure 19F-H, J-L). This wavy pattern was only partially reproduced by SVM cell type classifier (Figure 15F-H, J-L) suggesting that *pxy* cells classified as cambium are contaminated by neighbouring cell types. This is supported by a bigger quantile of the high area values in *pxy* mutants than in WT (Figure 20C). Xylem parenchyma cells followed the same growth pattern in *pxy* mutants as in WT (Figure 20B). Indeed, nothing peculiar could be observed in *pxy* xylem parenchyma when looking at the area heat maps except for some hotspots of huge cells (Figure 19F-H, J-L). However, *pxy* xylem parenchyma cells were larger than in WT starting from 4 wpg. Between 4 and 4.5 wpg, they were larger in *pxy-4* than in *pxy-2* but reached the same size at 5 wpg (Figure 20B). Phloem parenchyma cells grew slower in *pxy-2* than in WT and even more slower in *pxy-4*. By 5 wpg, *pxy-2* phloem parenchyma cells reached WT size even after a decrease compared to the previous time point, while phloem parenchyma cells in *pxy-4* remained smaller than phloem parenchyma cells in WT (Figure 20E). Indeed, as it had been shown with the cell dot plots, phloem was squeezed in *pxy* mutants during radial growth (Figure 13C, C1, Figure 14C, C1, Figure 16F-H, J-L, cyan) while maintaining the same cell number compared to WT (Figure 15M, cyan). Periderm cells of *pxy* mutants followed a similar growth trend as in WT except for the last time point when they continued growing while WT ones had stopped. These cells were bigger in *pxy* mutants than in WT at 3.5 wpg. Moreover, *pxy-2* periderm cells were smaller than in WT at 4 and 4.5 wpg but reached WT level at 5 wpg, while *pxy-4* periderm cells had WT size at 4 wpg. After that, they were smaller at 4.5 then, bigger at 5 wpg (Figure 20F). *pxy-2* xylem vessels spiked in size at 4 wpg, while *pxy-4* – at 4.5 wpg catching up the *pxy-2* level. At 5 wpg, xylem vessels size increased in *pxy-2* and decreased in *pxy-4* compared to the previous time point. These cells were smaller in *pxy* mutants than in WT at 3.5 wpg but larger from 4.5 wpg (Figure 20A).

In summary, quantitative histology revealed cell expansion in differentiated tissues during radial growth and revealed changes in these dynamics in the absence of *PXY* as well as subtle differences between *pxy-2* and *pxy-4* mutants.

3.4.2.2. Cell perimeter, major and minor axes

Another way to estimate cell growth is measuring cell perimeter. This descriptor is very similar to the cell area. The differences appear when cells acquire complex shapes. Indeed, cell perimeter followed the same variations over time and genotypes as cell area with a couple of exceptions for cambium and phloem parenchyma (Figure 20, 21). These subtle differences appeared more often at 5 wpg when cells acquired complex shapes (Figure 20A, B, E, F, Figure 21A, B, E, F). Perimeter heat maps appeared less contrasted than area heat maps (Figure 19, 22). This contrast was also observed in the shape of violin dot plots. For perimeter, the quantiles were more equilibrated than for area (Figure 20, 21).

Major and minor axes are other measures to estimate cell size. Major and minor axes are the length of the longest and shortest sectors respectively fitting into the cell and passing through the cell centre. They followed the same trends as cell perimeter but with some rare exceptions. The heat maps of these two measures are almost indistinguishable. Therefore, I estimate that cell major and minor axes provide very similar information as cell perimeter in the context of radial hypocotyl growth.

In summary, cell perimeter measures confirmed the results obtained by cell area measures. Cell perimeter shows gradual changes in cell growth, while cell area shows its contrast.

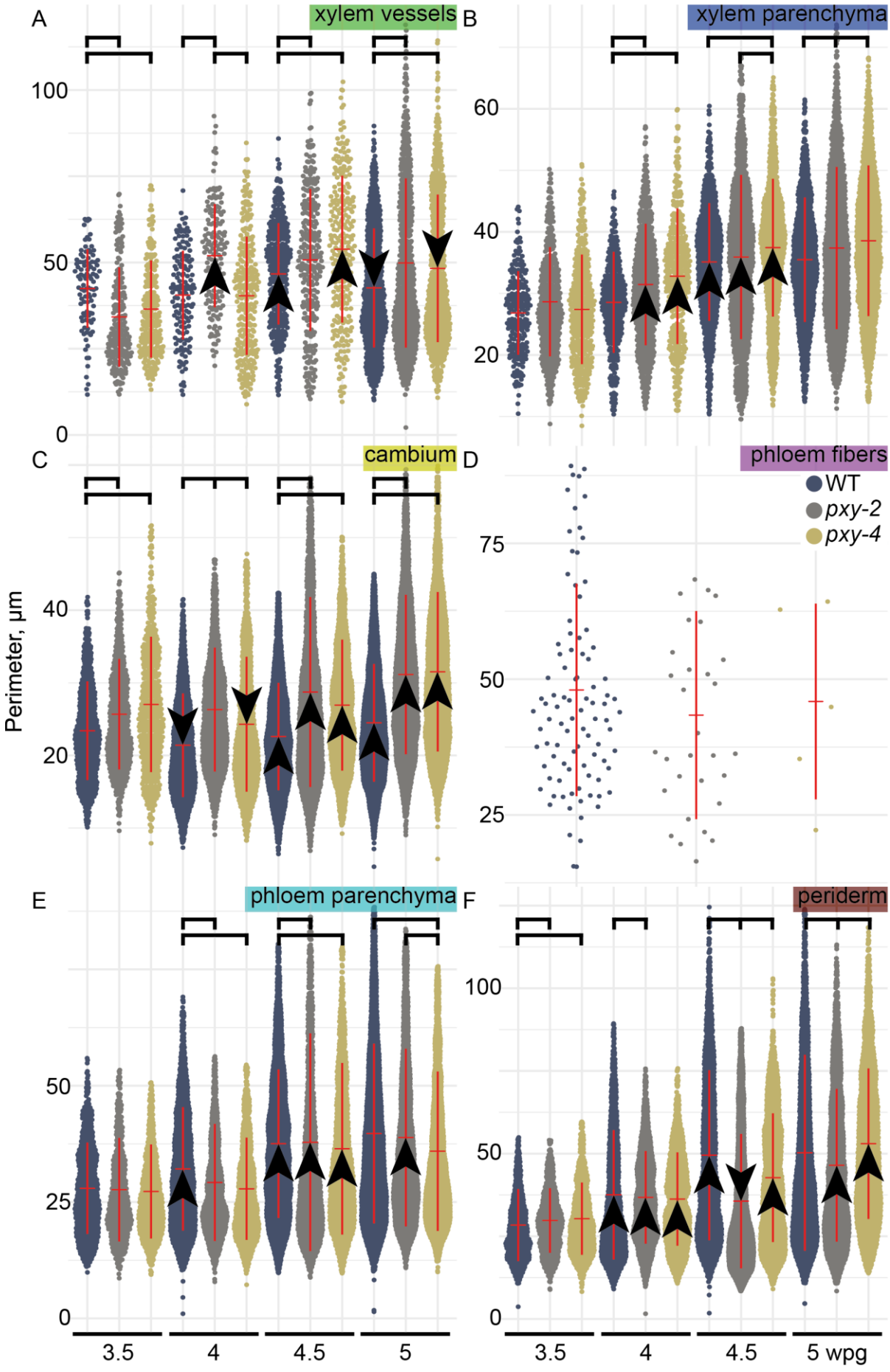
A
xylem vessels
B
xylem parenchyma
C
cambium
D
phloem fibers
WT
pxy-2
pxy-4
E
phloem parenchyma
F
periderm
Perimeter, µm
3.5
4
4.5
5
5 wpg

Figure 21. <u>Quantification of cell perimeter</u>. Xylem vessels (**A**), xylem parenchyma cells (**B**), cambium cells (**C**), phloem fibers (**D**), phloem parenchyma cells (**E**) and periderm cells (**F**) were extracted from image segmentations and the perimeter was measured. The time points are indicated in the lower part of the image. The y-axa correspond to perimeter as indicated in the left part of the Figure. The genotypes are colour-coded and the legend is in the right part of the Figure. Cell types are indicated in the upper-right corners of every graph. Red horizontal bar in the middle of a violin-shaped dot plot indicates the mean, the vertical red bar indicates +/- standard deviation from the mean. The outliers were removed from the dotplot but were included into the calculation of the mean and the standard deviation. Arrows pointing up and down indicate a significant increase and decrease respectively in mean degree for the corresponding genotype compared to the previous time point (p-value < 0.05 after Kruskal-Wallis test on a single genotype group followed by a post-hoc pairwise Dunn test with Bonferroni correction and p-value < 0.05). Square brakets indicate a significant difference after a Kruskal-Wallis test on the single time point group followed by a post-hoc pairwise Dunn test with Bonferroni correction and p-value < 0.05. In the absence of arrows or square brakets, the difference is not significant with p-value > 0.05.

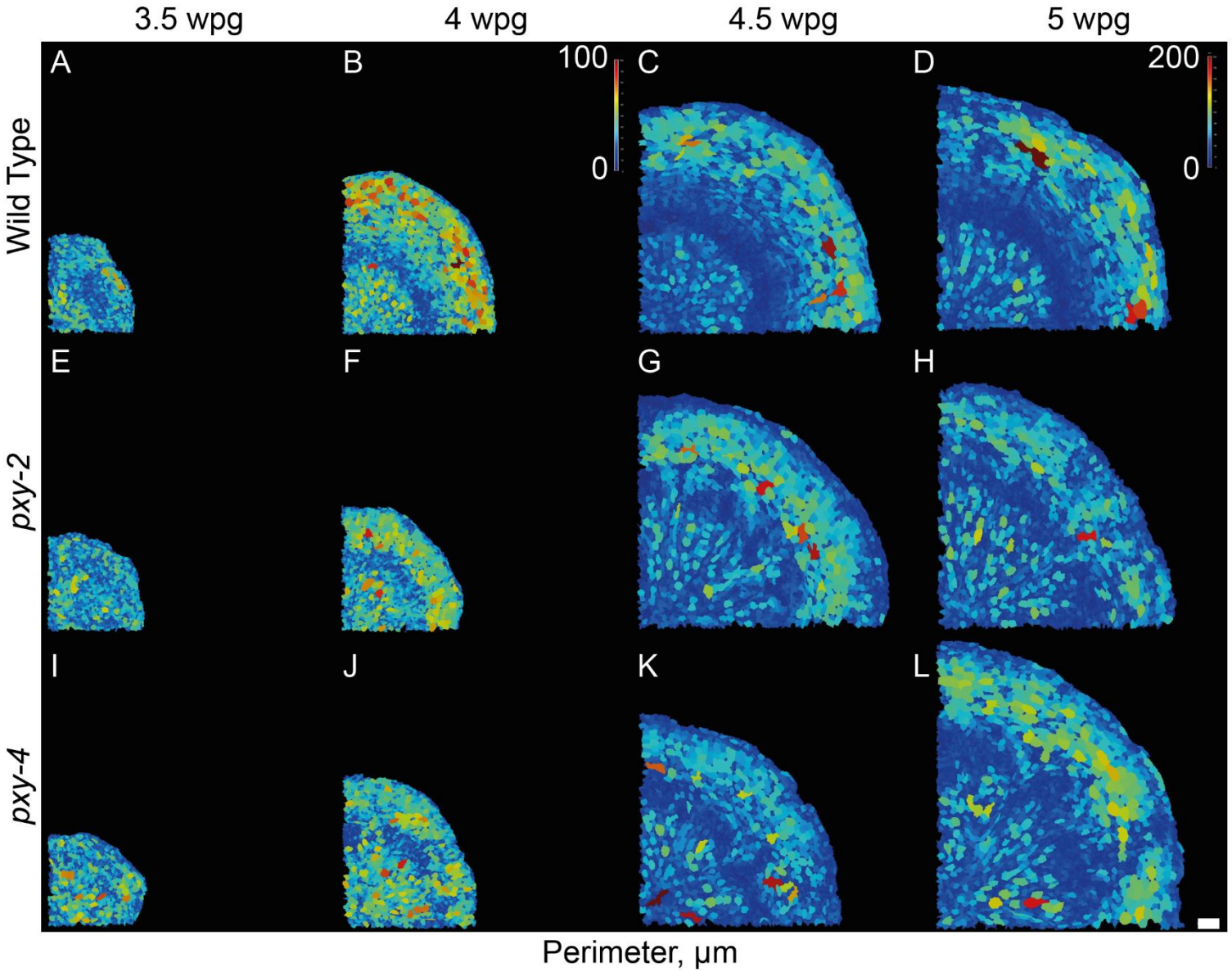

Figure 22. <u>Cell perimeter in wild type and *pxy* mutants hypocotyls during radial growth</u>. A-D. Wild type. **E-H.** *pxy*-2. **I-L.** *pxy-4*. **A, E, I.** 3.5 weeks post-germination (wpg). **B, F, J.** 4 wpg. **C, G, K.** 4.5 wpg. **D, H, L.** 5 wpg. The calibration bar in **B** gives the color code for **A, B, E, F, I** and **J**. The calibration bar in **D** gives the color code for **C, D, G, H, K** and **L**. The values of the calibration bars are indicated in µm. The scale bar in **L** corresponds to 50 µm and applies to the whole figure.

3.4.2.3. Aspect ratio

The ratio between cell major and minor axa gives cell aspect ratio. It represents the isotropy of a cell. A perfectly isotropic cell takes a value of 1 for aspect ratio. The more a cell is anisotropic, the higher is its aspect ratio.

The aspect ratio of hypocotyl cells fluctuated between 1 and 3 except for the cells in *pxy-4* hypocotyl at 4.5 wpg reaching higher values (Figure 23). The peculiar cell population with high values for aspect ratio in *pxy-4* could not be confirmed by the corresponding heat map (Figure 24K). No such anomaly was observed for major or minor axa heat maps. Therefore, I suspect that these high values are the results of an error that occurred during descriptors extraction with MGX and I decided to not consider it in my interpretation of the results.

During hypocotyl development, cells became more anisotropic in all tissues. It was expectable for xylem parenchyma cells to increase in anisotropy at 5 wpg (Figure 23B), for phloem parenchyma cells to increase in anisotropy at 4 and 4.5 wpg (Figure 23E) and for periderm cells to increase in anisotropy at 4.5 wpg (Figure 23F). Unexpectedly proliferating cambium cells decreased in their anisotropy at 5 wpg (Figure 23C). Differentiated xylem vessels maintained the same aspect ratio over time except for the last time-point when the aspect ratio increased (Figure 23A). Highest and lowest values of aspect ratio look like randomly distributed across tissues (Figure 24A-D). Although there is an exception: a radial front of cells having a medium aspect ratio in distal phloem from 4.5 wpg (Figure 24C, D).

pxy-2 phloem parenchyma cells and xylem vessels followed the same trend as WT for aspect ratio variation over time (Figure 23A, E). But *pxy-2* cambium cells became more anisotropic with time at 4 and 5 wpg (Figure 23C), while xylem parenchyma and periderm cells kept the same aspect ratio at all time points (Figure 23B, F). *pxy-4* xylem vessels, cambium and periderm cells did not change in isotropy between 3.5 and 4 wpg (Figure 23A, C, F) but *pxy-4* xylem parenchyma cells increased in aspect ratio at 4 wpg (Figure 23B).

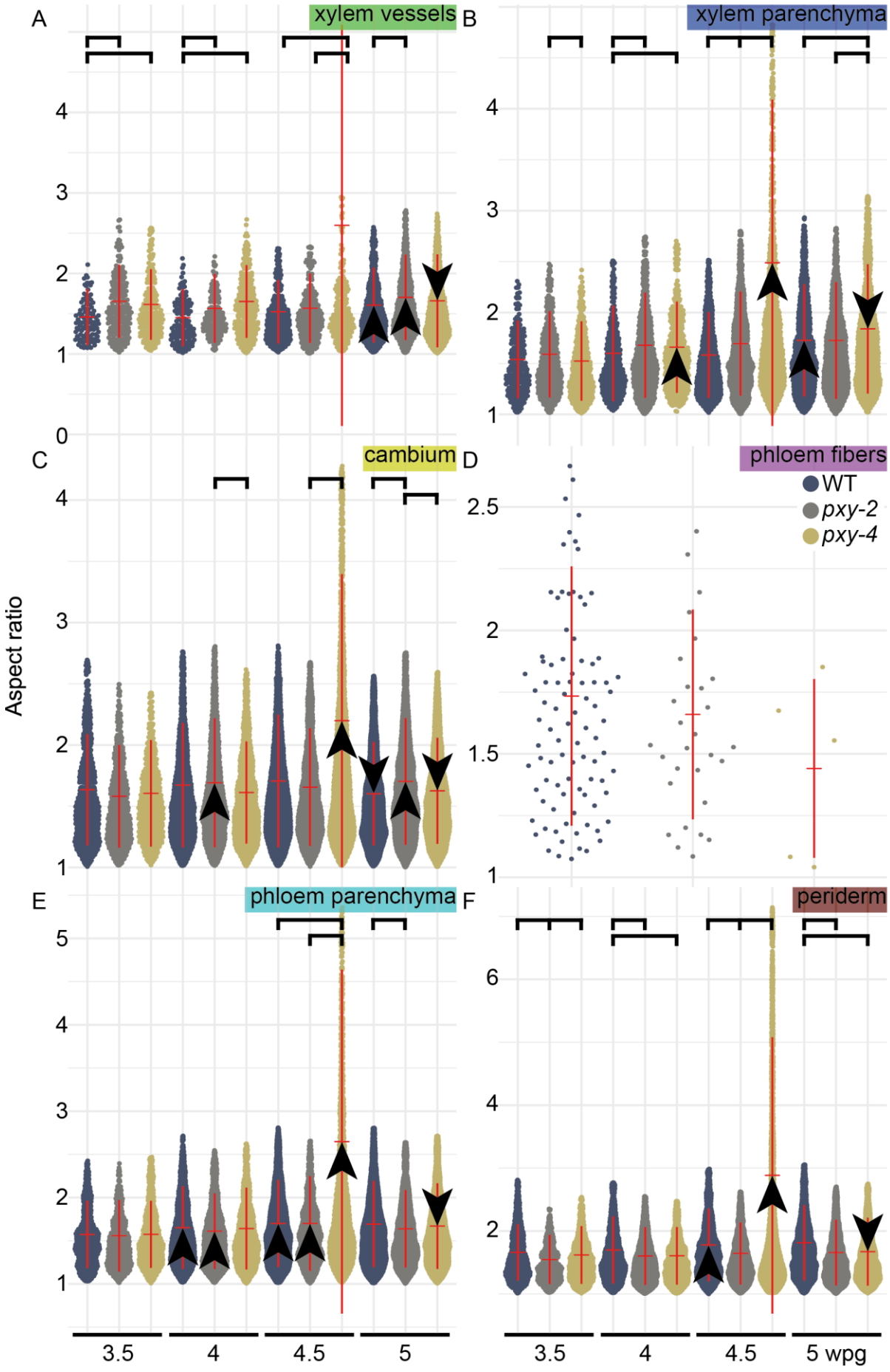
A
xylem vessels
B
xylem parenchyma
C
cambium
D
phloem fibers
WT
pxy-2
pxy-4
E
phloem parenchyma
F
periderm
Aspect ratio
3.5
4
4.5
5
3.5
4
4.5
5 wpg

Figure 23. <u>Quantification of cell aspect ratio</u>. Xylem vessels (**A**), xylem parenchyma cells (**B**), cambium cells (**C**), phloem fibers (**D**), phloem parenchyma cells (**E**) and periderm cells (**F**) were extracted from image segmentations and the aspect ratio was measured. The time points are indicated in the lower part of the image. The y-axa correspond to aspect ratio as indicated in the left part of the Figure. The genotypes are colour-coded and the legend is in the right part of the Figure. Cell types are indicated in the upper-right corners of every graph. Red horizontal bar in the middle of a violin-shaped dot plot indicates the mean, the vertical red bar indicates +/- standard deviation from the mean. The outliers were removed from the dotplot but were included into the calculation of the mean and the standard deviation. Arrows pointing up or down indicate a significant increase or decrease respectively in mean aspect ratio for the corresponding genotype compared to the previous time point (p-value < 0.05 after Kruskal-Wallis test on a single genotype group followed by a post-hoc pairwise Dunn test with Bonferroni correction and p-value < 0.05). Square brakets indicate a significant difference after a Kruskal-Wallis test on the single time point group followed by a post-hoc pairwise Dunn test with Bonferroni correction and p-value < 0.05. In the absence of arrows or square brakets, the difference is not significant with p-value > 0.05.

Cambium cells were more anisotropic in *pxy-2* than in *pxy-4* at 4 wpg and more anisotropic than both WT and *pxy-4* at 5 wpg (Figure 23C). Xylem parenchyma cells were more anisotropic in *pxy-2* compared to *pxy-4* at 3.5 wpg and compared to WT at 4 and 4.5 wpg. But at 5 wpg, WT xylem parenchyma cells reached the level of *pxy-2* aspect ratio while *pxy-4* had a higher value compared to both genotypes (Figure 23B). The aspect ratio of xylem vessels was higher in *pxy* mutants compared to WT at 3.5 and 4 wpg, but at 4.5 wpg, *pxy-2* reached the WT isotropy level then, at 5 wpg, *pxy-4* reached the WT isotropy level (Figure 23A). The aspect ratio of phloem parenchyma cells was similar between genotypes except for the last time-point when *pxy-2* cells were more isotropic than WT (Figure 23E). The aspect ratio of periderm cells was different between the three genotypes at 3.5 wpg while at 4 and 5 wpg, the aspect ratio of periderm cells was lower in *pxy* mutants than in WT but undistinguishable between *pxy-2* and *pxy-4*. The aspect ratio of periderm cells was also lower in *pxy-2* compared to WT at 4.5 wpg (Figure 23F). Indeed, more anisotropic cells were noticed in xylem region of *pxy* mutants compared to WT, while more isotropic cells were noticed in periderm region of *pxy* mutants compared to WT. This trend got more accentuated with time (Figure 24). The medium isotropy front in distal phloem is absent from *pxy* mutants (Figure 24G, H, K, L).

In summary, cell isotropy dynamics during radial growth were tissue-specific even though a broad intra-tissular variation was observed on heat maps. For some tissues, *pxy-2* followed WT trends in aspect ratio dynamics, for other tissues, *pxy-4* followed WT trends.

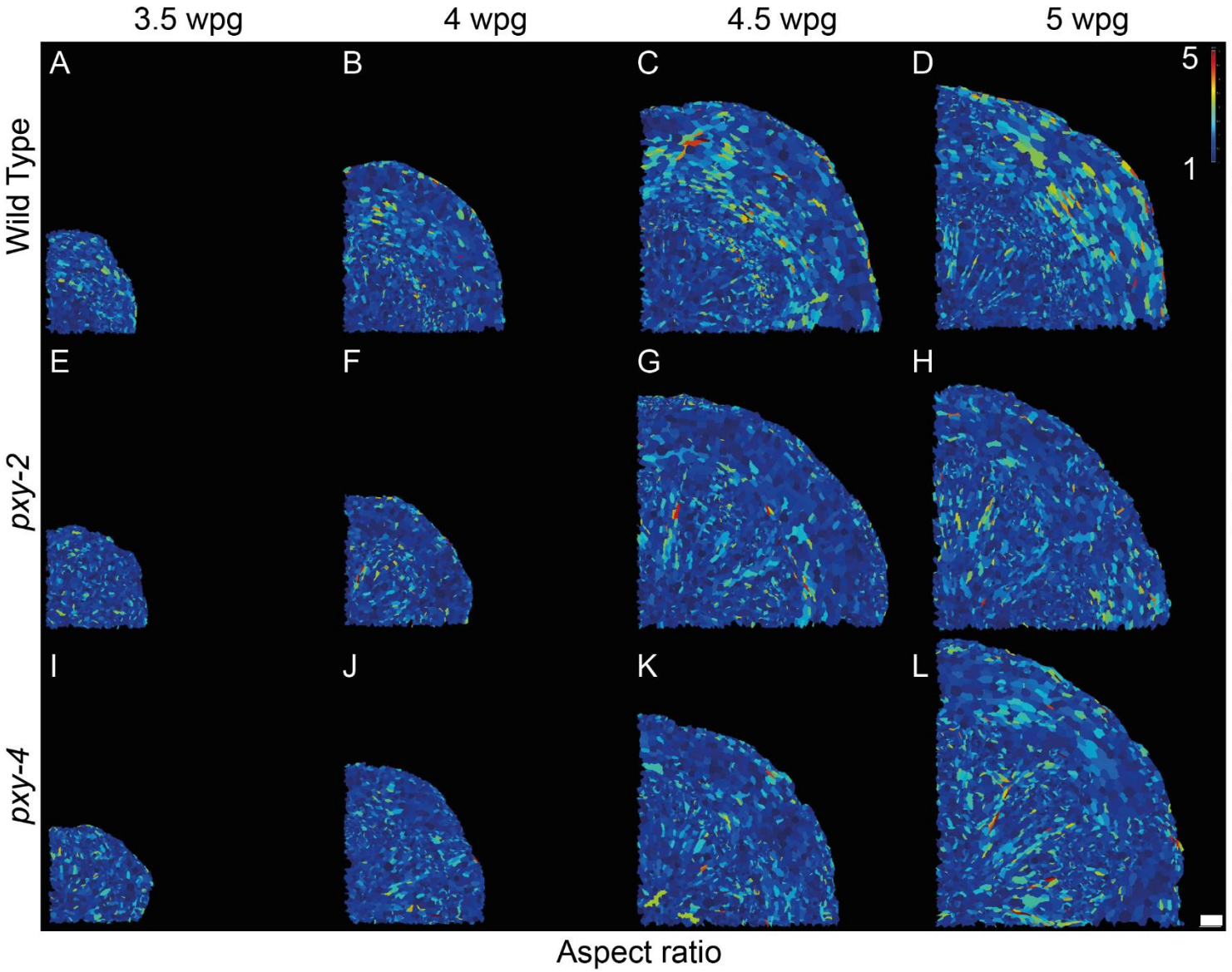

Figure 24 . <u>Cell aspect ratio in wild type and *pxy* mutants hypocotyls during radial growth</u>. **A-D.** Wild type. **E-H.** *pxy-2*. **I-L.** *pxy-4*. **A, E, I.** 3.5 weeks post-germination (wpg). **B, F, J.** 4 wpg. **C, G, K.** 4.5 wpg. **D, H, L.** 5 wpg. The values of the calibration bar in **D** correspond to the ratio between cell major axis and cell minor axis. The scale bar in **L** corresponds to 50 µm and applies to the whole figure.

3.4.2.4. Circularity

The first way to estimate cell shape is to look at its circularity. Circularity takes a value of 1 for a perfect circle and higher values for more oval and complex shapes. Hypocotyl cells circularity fluctuated between 1.2 and 2.5 (Figure 25).

The heat maps showed more hot spots of increased circularity with time across all tissues (Figure 26A-D). During hypocotyl development, cambium cells and xylem vessels circularity increased only at 4.5 wpg (Figure 25A, C), while xylem parenchyma cells circularity increased at 4.5 and even further at 5 wpg (Figure 25B). Circularity of phloem parenchyma and periderm cells increased at 4 and 4.5 wpg then, dropped at 5 wpg (Figure 25E, F).

Circularity of *pxy-2* cambium cells increased then dropped again at 4 and 4.5 wpg, respectively. Cambium cells in *pxy-4* followed the same trend as in *pxy-2* with a half of a week delay (Figure 25C). The circularity of xylem parenchyma cells in *pxy-2* mutants increased at 4 wpg. In *pxy-4* mutants, the circularity of xylem parenchyma cells increased at 4 wpg and even further at 4.5 wpg (Figure 25B). At 5 wpg, the circularity of xylem vessels increased in *pxy-2* mutants and decreased in *pxy-4* mutants (Figure 25A). The circularity of phloem parenchyma cells in *pxy* mutants followed the same trend over time as in WT except for *pxy-2* at 4.5 wpg when the circularity of phloem parenchyma cells did not increase (Figure 25E). The circularity of periderm cells in *pxy* mutants followed the same trend over time as in WT except for *pxy-4* at 4 and 5 wpg when the circularity of periderm cells did not increase and did not decrease respectively (Figure 25F).

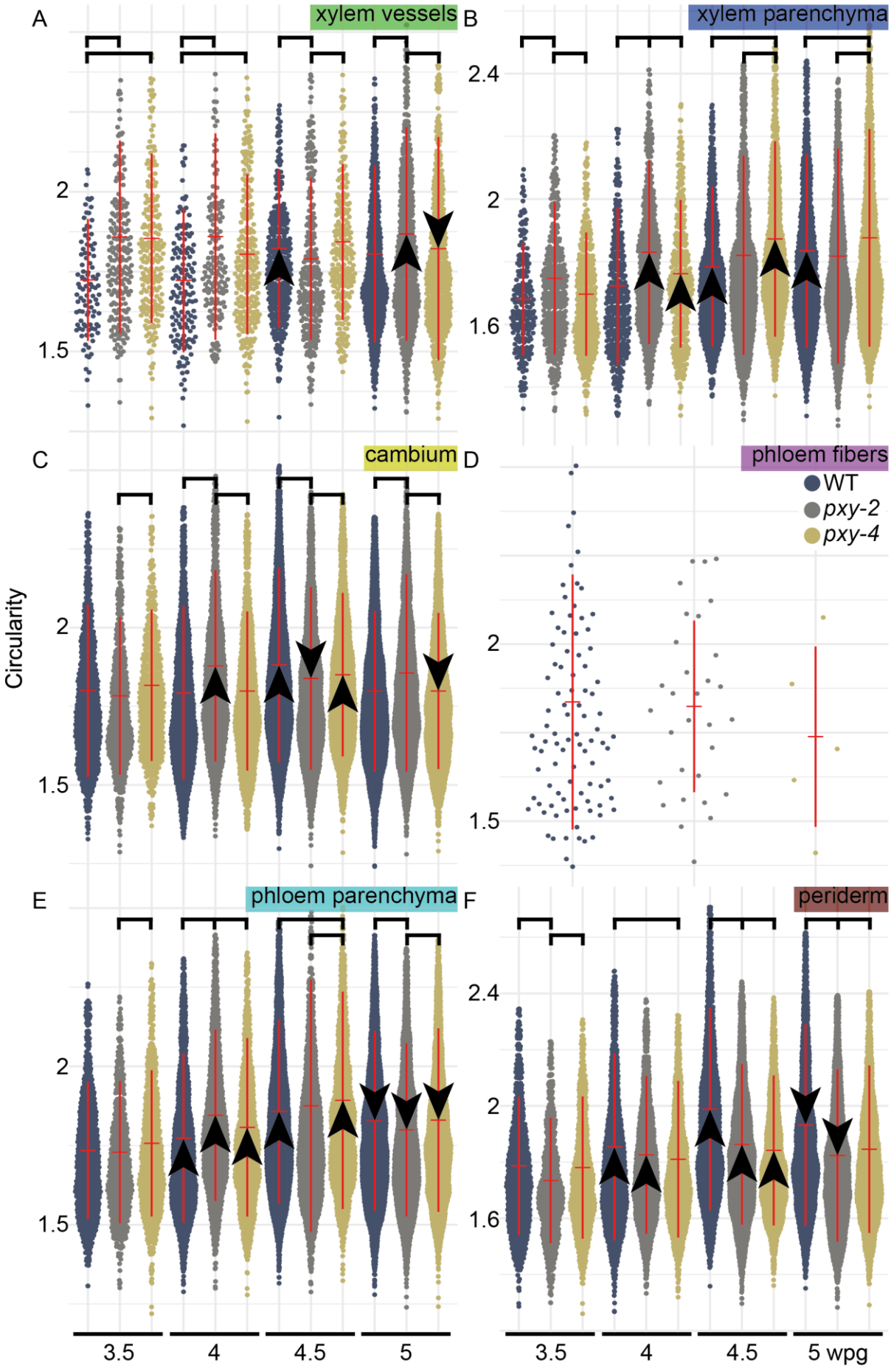
A
xylem vessels
B
xylem parenchyma
C
cambium
D
phloem fibers
WT
pxy-2
pxy-4
E
phloem parenchyma
F
periderm
Circularity
2.4
2
1.6
1.5
3.5
4
4.5
5
5 wpg

Figure 25. Quantification of cell circularity. Xylem vessels (**A**), xylem parenchyma cells (**B**), cambium cells (**C**), phloem fibers (**D**), phloem parenchyma cells (**E**) and periderm cells (**F**) were extracted from image segmentations and the circularity was measured. The time points are indicated in the lower part of the image. The y-axa correspond to circularity as indicated in the left part of the Figure. The genotypes are colour-coded and the legend is in the right part of the Figure. Cell types are indicated in the upper-right corners of every graph. Red horizontal bar in the middle of a violin-shaped dot plot indicates the mean, the vertical red bar indicates +/- standard deviation from the mean. The outliers were removed from the dotplot but were included into the calculation of the mean and the standard deviation. Arrows pointing up and down indicate a significant increase and decrease respectively in mean circularity for the corresponding genotype compared to the previous time point (p-value < 0.05 after Kruskal-Wallis test on a single genotype group followed by a post-hoc pairwise Dunn test with Bonferroni correction and p-value < 0.05). Square brakets indicate a significant difference after a Kruskal-Wallis test on the single time point group followed by a post-hoc pairwise Dunn test with Bonferroni correction and p-value < 0.05. In the absence of arrows or square brakets, the difference is not significant with p-value > 0.05.

The circularity of cambium cells in *pxy-2* mutant alternated between being inferior to the circularity of cambium cells in *pxy-4* at 3.5 wpg, in WT and *pxy-4* at 3.5 and 4.5 wpg or superior at 4 and 5 wpg (Figure 25C). At 3.5 and 4 wpg, the circularity of xylem parenchyma cells in *pxy-2* mutant was higher than the one in WT and *pxy-4* mutant but at later time-points, xylem parenchyma cells in *pxy-4* had a higher circularity than WT and *pxy-2*. The circularity of xylem parenchyma cells was also higher in *pxy-4* than in WT at 4 wpg (Figure 25B). At 3.5 and 4 wpg, the circularity of xylem vessels in both *pxy* mutants was higher than the one in WT. At 4.5 wpg, the circularity of xylem vessels of WT reached the same value as *pxy-4* while the circularity of xylem vessels in *pxy-2* was lower compared to WT. At 5 wpg, the circularity of *pxy-2* xylem vessels got highest between the three genotypes (Figure 25A). The differences between the circularity of phloem parenchyma cells in different genotypes changed at every time-point. At 3.5 wpg, the circularity of phloem parenchyma and periderm cells was higher in *pxy-4* than in *pxy-2*. At 4 wpg, the circularity of phloem parenchyma cells was higher in *pxy-4* compared to WT and even higher in *pxy-2* compared to *pxy-4*. At 4.5 wpg, the circularity of phloem parenchyma cells was higher in *pxy-4* mutant compared to WT and *pxy-2* mutant. At 5 wpg, the circularity of phloem parenchyma cells was lower in *pxy-2* mutant compared to WT and *pxy-4* mutant (Figure 25E). At 3.5 wpg, the circularity of periderm cells was lower in *pxy-2* mutant compared to WT and *pxy-4* mutant. At 4 wpg, the circularity of periderm cells was lower in *pxy-2* mutant than in WT. At 4.5 wpg, the circularity of periderm cells was lower in *pxy-2* mutant than in WT and even lower in *pxy-4*. At 5 wpg, the circularity of periderm cells was lower in *pxy-4* mutant than in WT and even lower in *pxy-2* mutant (Figure 25F). Indeed, the heat maps of circularity showed less high value hot spots in periderm of *pxy* mutants compared to WT from 4.5 wpg (Figure 26C, D, G, H, K, L).

In summary, I observed a highly fluctuating data on cell circularity in WT and *pxy* mutants. However, one consistent observation was made: periderm cells were more circular in *pxy* mutants compared to WT at late developmental stages.

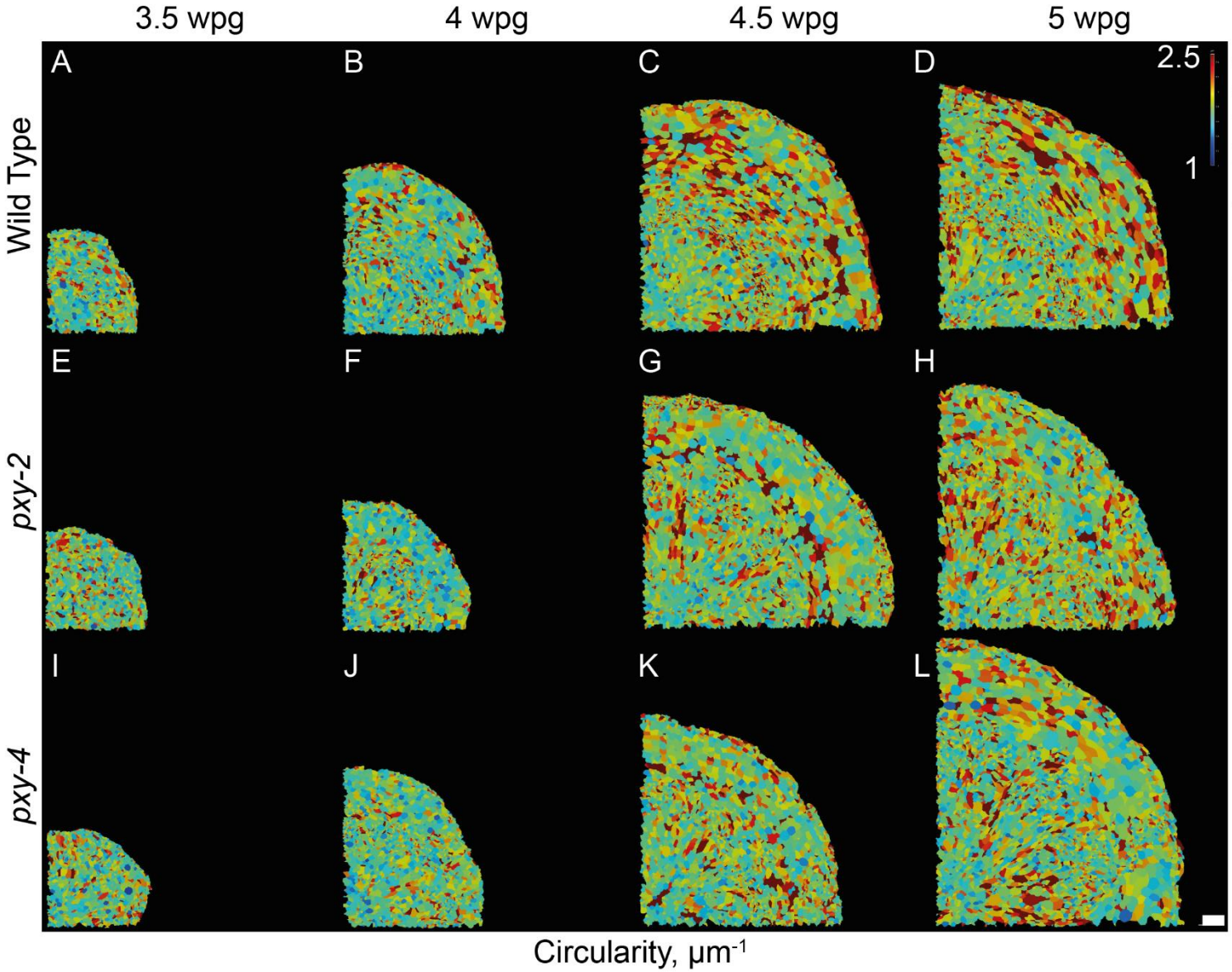

Figure 26. <u>Cell circularity in wild type and *pxy* mutants hypocotyls during radial growth</u>. A-D. Wild type. **E-H.** *pxy-2*. **I-L.** *pxy-4*. **A, E, I.** 3.5 weeks post-germination (wpg). **B, F, J.** 4 wpg. **C, G, K.** 4.5 wpg. **D, H, L.** 5 wpg. The values in the calibration bar in **D** correspond to 4 * π * cell area / (cell perimeter)². The scale bar in **L** corresponds to 50 µm and applies to the whole figure.

3.4.2.5. Rectangularity

Another way to estimate cell shape is measuring its rectangularity. Rectangularity can take a maximum value of 1 which would correspond to a perfect rectangle or lower values corresponding to smoother, less orthogonal or more complex shapes. The rectangularity of hypocotyl cells fluctuated between 0.5 and 0.9 (Figure 27). The distribution of the most or least rectangular cells across tissues looked mostly random. I only noticed hotspots of the lowest values in distal phloem. I did not observe any flagrant qualitative differences in this regard between different tissues, developmental stages or genotypes (Figure 28).

When the mean values of cell types were considered, the rectangularity of cambium cells decreased at 4 and 4.5 wpg (Figure 27C). For xylem and phloem parenchyma cells, the rectangularity decreased only at 5 wpg (Figure 27B, E). For xylem vessels, the rectangularity increased at 4 wpg then, decreased at 4.5 wpg (Figure 27A).

For xylem vessels in *pxy-2* mutant, the rectangularity followed the same trend as in WT, but the decrease was delayed to 5 wpg (Figure 27A). Cambium cells in *pxy-2* increased in rectangularity first at 4.5 wpg then, decreased at 5 wpg (Figure 27C). The rectangularity of phloem parenchyma cells in *pxy-2* mutant decreased at 4 wpg then, increased at 5 wpg (Figure 27E) while the rectangularity of xylem parenchyma cells in *pxy-2* mutant did not change over time (Figure 27B). The rectangularity of periderm cells in *pxy-2* mutant decreased at 4 wpg and decreased even more at 4.5 wpg (Figure 27F). The rectangularity of hypocotyl cells in *pxy-4* mutant remained the same over time (Figure 27) except for the rectangularity of periderm cells that decreased at 4.5 wpg (Figure 27F).

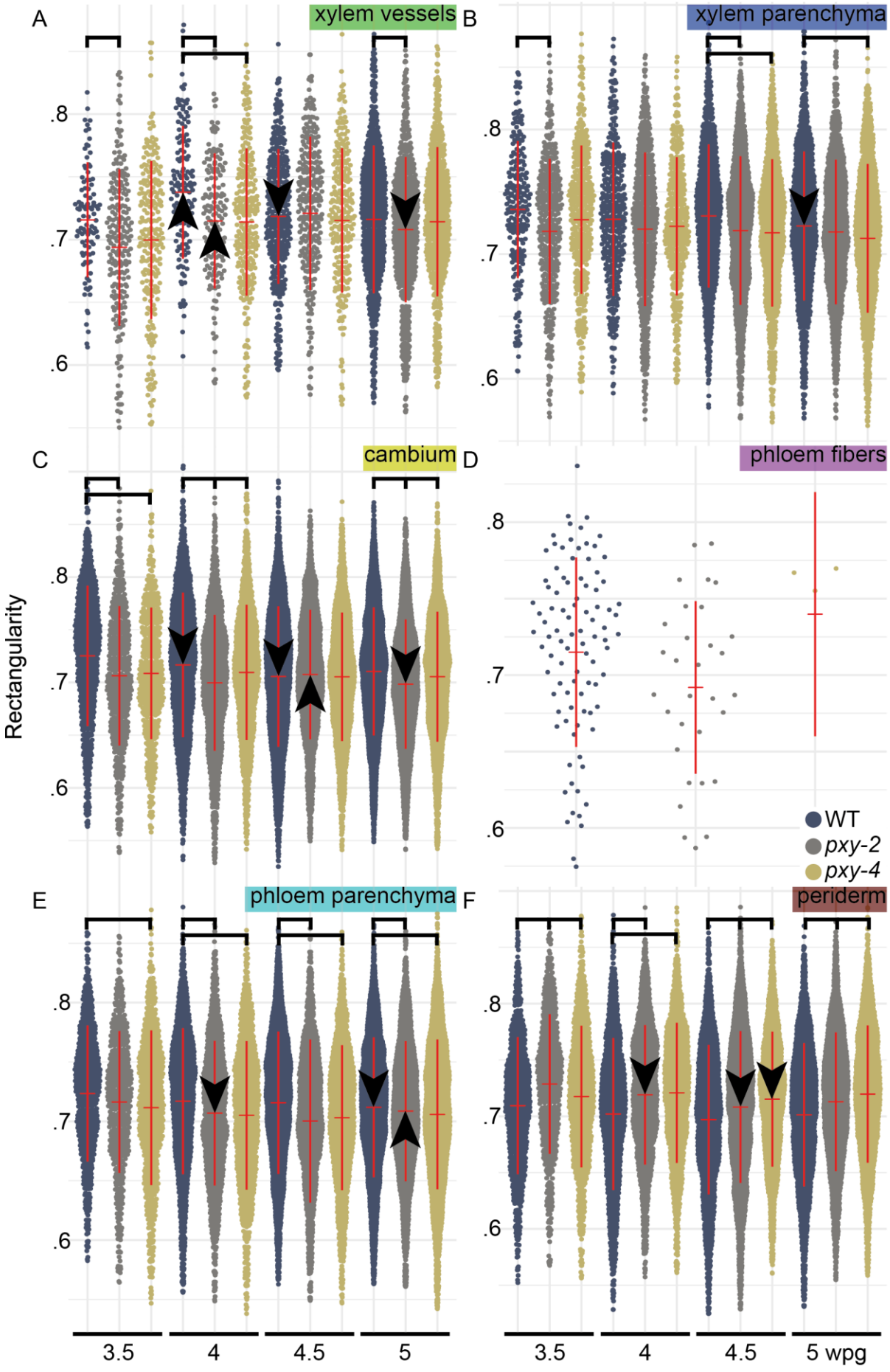
A
xylem vessels
B
xylem parenchyma
C
cambium
D
phloem fibers
E
phloem parenchyma
F
periderm
Rectangularity
.8
.7
.6
WT
pxy-2
pxy-4
3.5
4
4.5
5
5 wpg

Figure 27. <u>Quantification of cell rectangularity</u>. Xylem vessels (**A**), xylem parenchyma cells (**B**), cambium cells (**C**), phloem fibers (**D**), phloem parenchyma cells (**E**) and periderm cells (**F**) were extracted from image segmentations and the rectangularity was measured. The time points are indicated in the lower part of the image. The y-axa correspond to rectangularity as indicated in the left part of the Figure. The genotypes are colour-coded and the legend is in the right part of the Figure. Cell types are indicated in the upper-right corners of every graph. Red horizontal bar in the middle of a violin-shaped dot plot indicates the mean, the vertical red bar indicates +/- standard deviation from the mean. The outliers were removed from the dotplot but were included into the calculation of the mean and the standard deviation. Arrows pointing up and down indicate a significant increase and decrease respectively in mean rectangularity for the corresponding genotype compared to the previous time point (p-value < 0.05 after Kruskal-Wallis test on a single genotype group followed by a post-hoc pairwise Dunn test with Bonferroni correction and p-value < 0.05). Square brakets indicate a significant difference after a Kruskal-Wallis test on the single time point group followed by a post-hoc pairwise Dunn test with Bonferroni correction and p-value < 0.05. In the absence of arrows or square brakets, the difference is not significant with p-value > 0.05.

The rectangularity of cambium cells was lower in *pxy* mutants compared to WT except for the time-point 4.5 wpg when it was equal. The rectangularity of cambium cells was lower in *pxy-2* than in *pxy-4* at 4 and 5 wpg (Figure 27C). The rectangularity of xylem parenchyma cells was lower in *pxy-2* than in WT at 3.5 and 4.5 wpg while the rectangularity of xylem parenchyma cells got lower in *pxy-4* than in WT from 4.5 wpg on (Figure 27B). The rectangularity of xylem vessels was lower in *pxy-2* than in WT all the time except for 4.5 wpg. The rectangularity of xylem vessels was lower in *pxy-4* than in WT at 4 wpg (Figure 27A). The rectangularity of phloem parenchyma was always lower in *pxy-2* than in WT except for 3.5 wpg and it was always lower in *pxy-4* than in WT (Figure 27E). At 3.5 wpg, the rectangularity of periderm cells was higher in *pxy-4* mutant than in WT and even higher in *pxy-2* mutant. At 4 wpg, *pxy* mutants reached the same level of periderm cells rectangularity but it remained higher than the WT one. From 4.5 wpg on, the rectangularity of periderm cells was higher in *pxy-2* mutant than in WT and even higher than that in *pxy-4* mutant (Figure 27F).

In summary, WT hypocotyl cells became less rectangular over time except for xylem vessels that first, increase then, drop in rectangularity. *pxy* hypocotyl cells followed a less straightforward fluctuation in rectangularity or even none during plant development. They were less rectangular than WT hypocotyl cells except for periderm cells that were more rectangular in *pxy* than in WT. Some slight differences were also found between *pxy-2* and *pxy-4* but I did not observe any consistent trend.

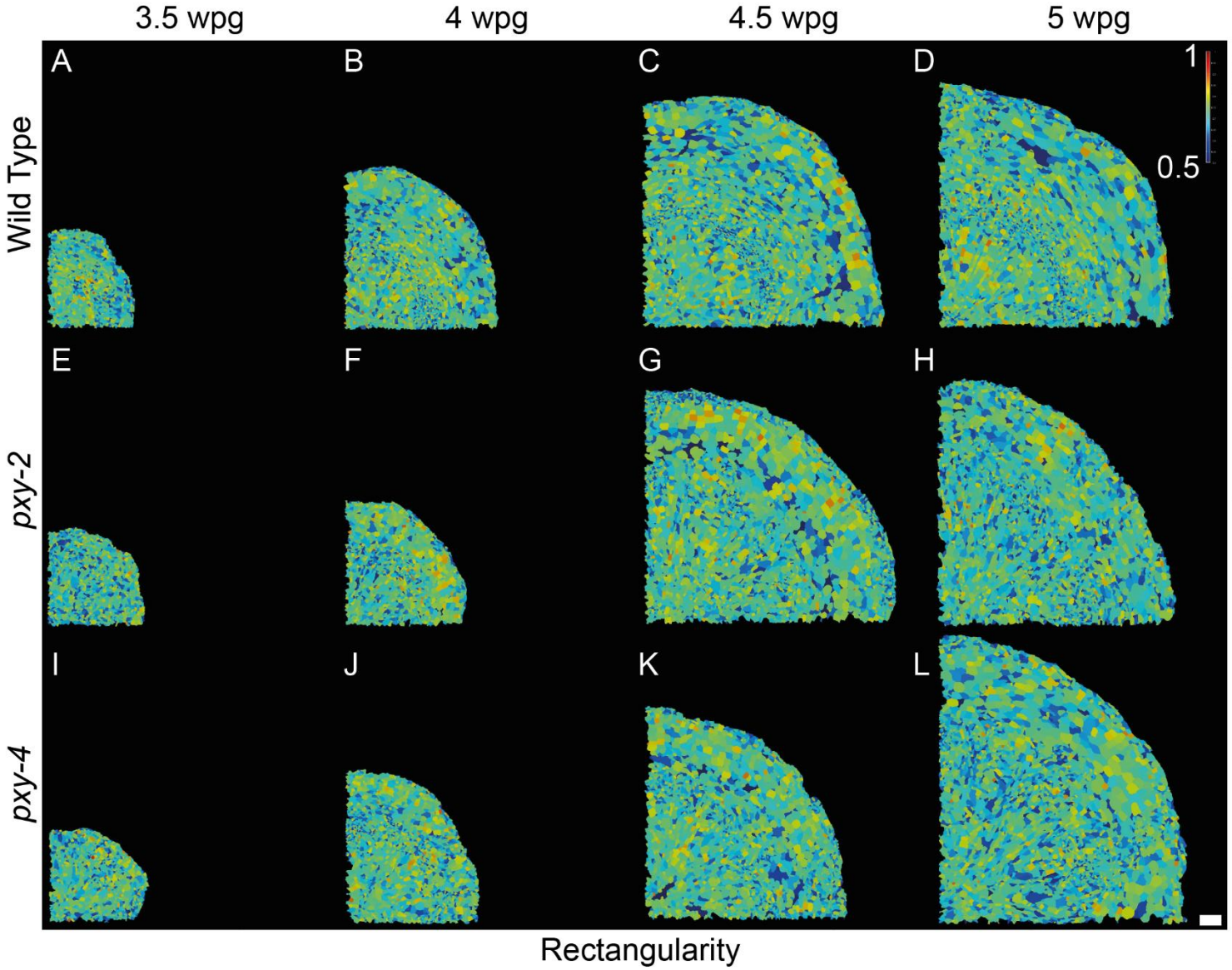

Figure 28. <u>Cell rectangularity in wild type and *pxy* mutants hypocotyls during radial growth</u>. A-D. Wild type. **E-H.** *pxy-2*. **I-L.** *pxy-4*. **A, E, I.** 3.5 weeks post-germination (wpg). **B, F, J.** 4 wpg. **C, G, K.** 4.5 wpg. **D, H, L.** 5 wpg. The values in the calibration bar in **D** correspond to cell area / (cell major axis * cell minor axis). The scale bar in **L** corresponds to 50 µm and applies to the whole figure.

3.4.2.6. Lobeyness

Lobeyness represents how much a cell is covered with lobes. The minimum value is 1 that corresponds to a non-lobeyed cell. The highest value observed in plants is 1.5 in leaf epidermis for puzzle cells [12]. Hypocotyl cells lobeyness ranged between 1 and 1.4 (Figure 29). The distribution of cell lobeyness across tissues looked random at first sight (Figure 30). But I observed some hotspots of the most lobeyed cells in phloem parenchyma at late stages of plant development. Lobeyness took a checkboard pattern in differentiated tissues with highly lobbeyed cells surrounded by low lobbeyed ones at late developmental stages (Figure 30C, D, G, H, K, L).

When looking at average values, WT hypocotyl cells increased in lobeyness at 4.5 wpg then, decreased at 5 wpg (Figure 29). Cambium cells additionally dropped in lobeyness at 4 wpg before following the general up and down trend (Figure 29C). *pxy-4* hypocotyl cells followed the same trend in lobeyness variability over plant development as WT ones (Figure 29) except for xylem parenchyma and periderm cells increasing in lobeyness already at 4 wpg (Figure 29B, F). For *pxy-2* mutant, the first increase in lobeyness took place earlier at 4 wpg, followed by the decrease at 4.5 wpg for xylem vessels, xylem and phloem parenchyma cells (Figure 29A, B, E). This decrease was delayed for periderm cells (Figure 29C) and never happened for cambium cells (Figure 29F).

The lobeyness of xylem vessels was higher in *pxy-2* at 4 wpg then, lower at 4.5 wpg compared to other genotypes (Figure 29A). The lobeyness of xylem parenchyma cells was lower in *pxy-4* than in *pxy-2* at 3.5 wpg. It was higher in *pxy-4* compared to WT and higher than that in *pxy-2* at 4 wpg. The lobeyness of xylem parenchyma cells was lower in *pxy-2* compared to other genotypes at 4.5 wpg. At 5 wpg, this measure was only lower in *pxy-2* when compared to WT (Figure 29B). The lobeyness of cambium cells was higher in *pxy-4* than in other genotypes at 3.5 and 4.5 wpg, at 4 wpg, it was higher only compared to WT. At 4 and 5 wpg, the lobeyness of *pxy-2* cambium cells was higher compared to other genotypes (Figure 29C). The lobeyness of *pxy-2* phloem parenchyma cells was higher than other genotypes at 4 wpg then, lower at 4.5 wpg. The lobeyness of *pxy-4* phloem parenchyma cells was higher than WT at 4.5 wpg then, lower at 5 wpg (Figure 29E). The lobeyness of *pxy-2* periderm cells was higher than WT at 4 wpg than, lower compared to both genotypes from 4.5 wpg on. Compared to WT, the lobeyness of *pxy-4* periderm cells was higher at 4 wpg then, lower at 4.5 wpg (Figure 29F).

In summary, hypocotyl cells got more lobeyed at around half of the considered developmental period and then decreased in lobeyness later. In *pxy-2*, it happened earlier than in WT or *pxy-4*. Cambium presented an exception from this trend with an additional decrease in cell lobeyness in the beginning. These subtle changes were not noticeable qualitatively on heat maps except for some extreme values.

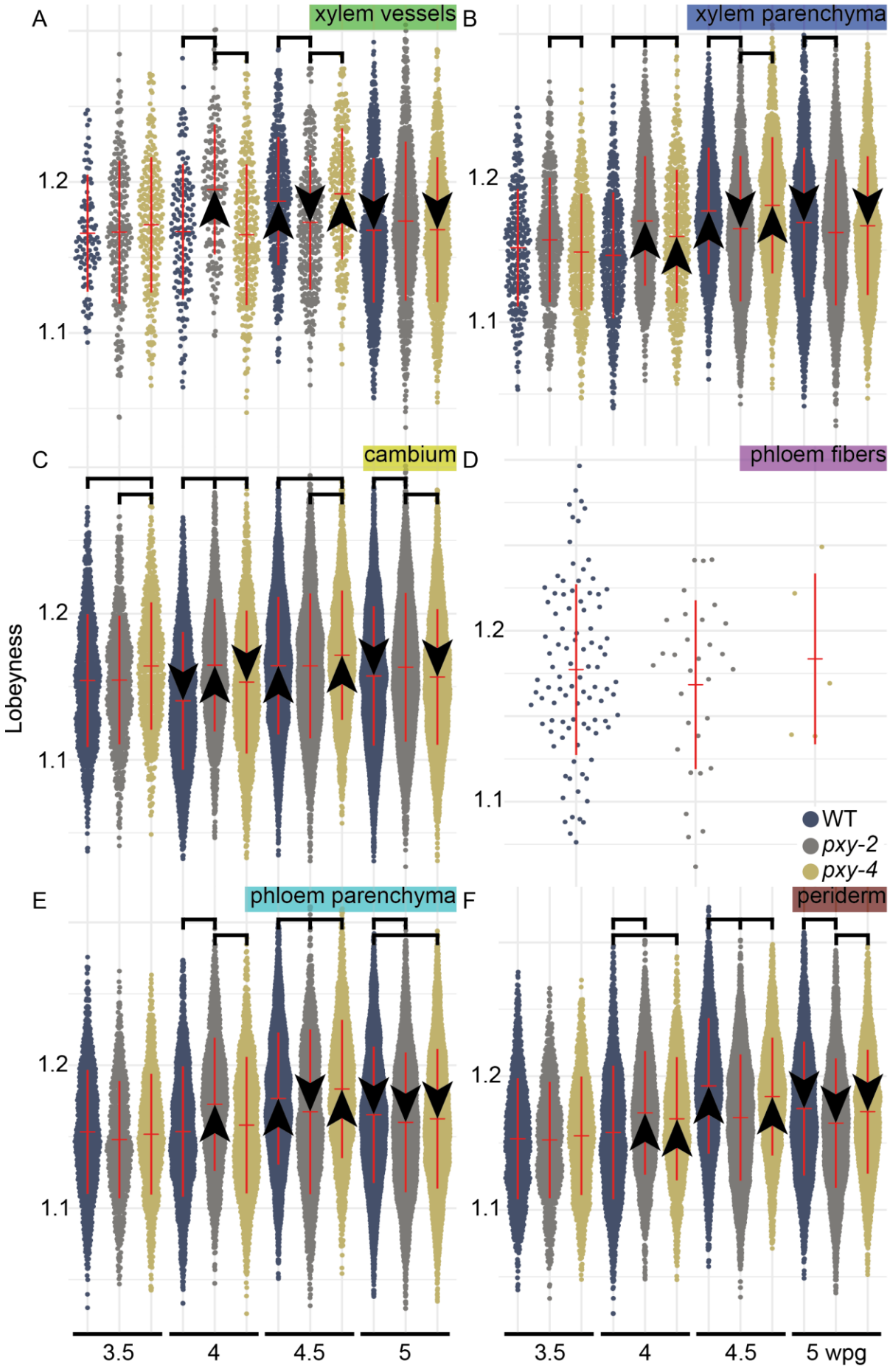
A
xylem vessels
B
xylem parenchyma
C
cambium
D
phloem fibers
E
phloem parenchyma
F
periderm
Lobeyness
1.2
1.1
WT
pxy-2
pxy-4
3.5
4
4.5
5
5 wpg

Figure 29. <u>Quantification of cell lobeyness</u>. Xylem vessels (**A**), xylem parenchyma cells (**B**), cambium cells (**C**), phloem fibers (**D**), phloem parenchyma cells (**E**) and periderm cells (**F**) were extracted from image segmentations and the lobeyness was measured. The time points are indicated in the lower part of the image. The y-axa correspond to lobeyness as indicated in the left part of the Figure. The genotypes are colour-coded and the legend is in the right part of the Figure. Cell types are indicated in the upper-right corners of every graph. Red horizontal bar in the middle of a violin-shaped dot plot indicates the mean, the vertical red bar indicates +/- standard deviation from the mean. The outliers were removed from the dotplot but were included into the calculation of the mean and the standard deviation. Arrows pointing up and down indicate a significant increase and decrease respectively in mean lobeyness for the corresponding genotype compared to the previous time point (p-value < 0.05 after Kruskal-Wallis test on a single genotype group followed by a post-hoc pairwise Dunn test with Bonferroni correction and p-value < 0.05). Square brakets indicate a significant difference after a Kruskal-Wallis test on the single time point group followed by a post-hoc pairwise Dunn test with Bonferroni correction and p-value < 0.05. In the absence of arrows or square brakets, the difference is not significant with p-value > 0.05.

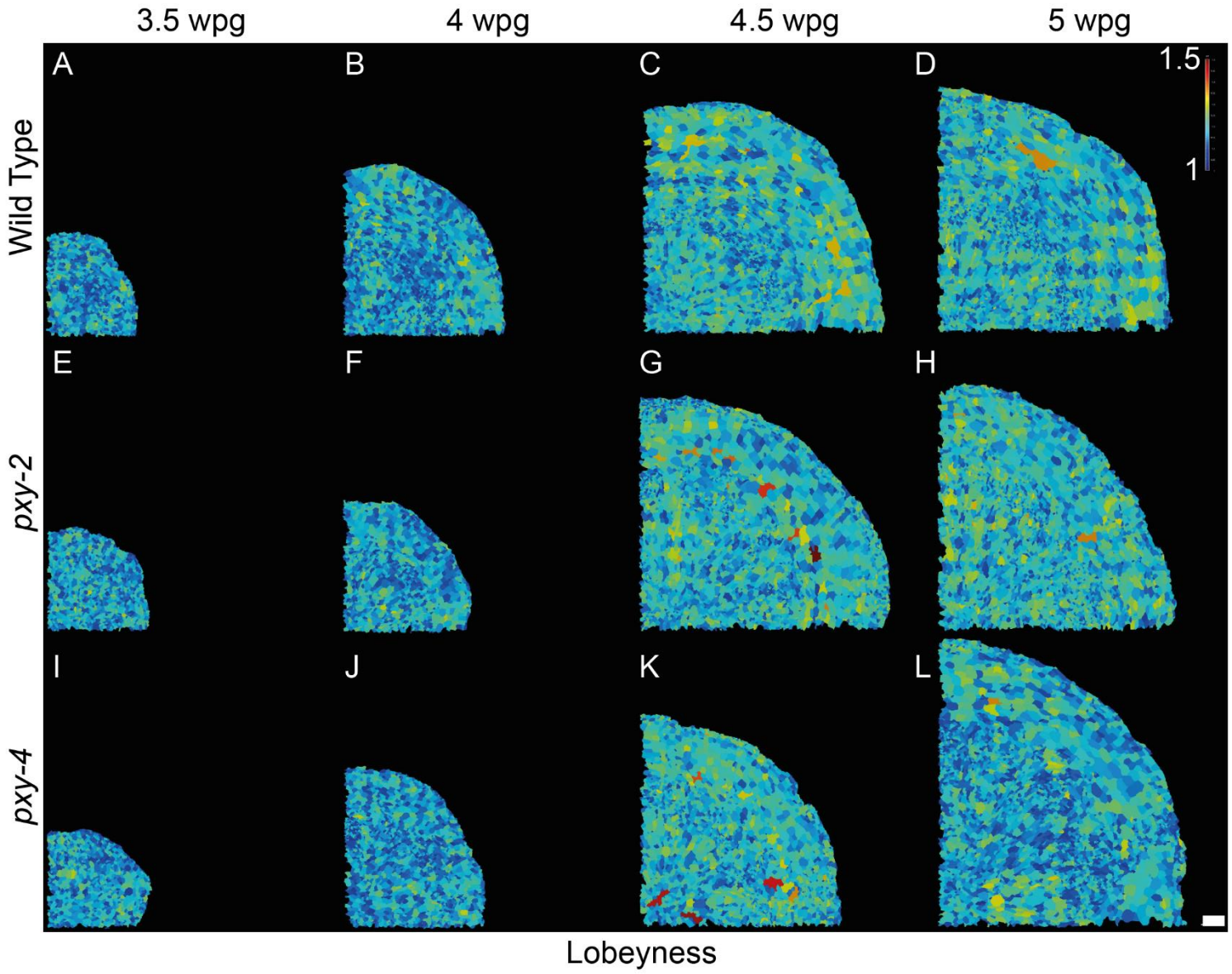

Figure 30. <u>Cell lobeyness in wild type and *pxy* mutants hypocotyls during radial growth</u>. A-D. Wild type. **E-H.** *pxy-2*. **I-L.** *pxy-4*. **A, E, I.** 3.5 weeks post-germination (wpg). **B, F, J.** 4 wpg. **C, G, K.** 4.5 wpg. **D, H, L.** 5 wpg. The values in the calibration bar in **D** correspond to cell perimeter / perimeter of convex hull. The scale bar in **L** corresponds to 50 µm and applies to the whole figure.

To summarise the analysis of hypocotyl cells morphology, the quantification and averaging of primary and secondary geometrical measures of cell morphology revealed subtle differences in cell morphology between WT, *pxy-2*, *pxy-4* and between different developmental stages. Heat maps are useful to reveal some topological patterns in cell morphology variation across tissues.

3.4.3. Tissue topology

Every single cell can be considered not just as an isolated tissue unit but also as a cell network unit. This has already been partially analysed higher when cells were represented as points of a graph with polar coordinates plotted in Euclidian space (Figure 16). But more elaborate measures are possible. By using cell major axis orientation and its polar coordinates, I calculated cell incline angle. I also calculated cell degree and betweenness centrality – two measures used in graph theory to estimate cell connectivity.

3.4.3.1. Incline angle

Incline angle is the angle formed between the major axis of the cell and the radial axis crossing the cell centre. In other words, it represents how much the cell is tilted from the radial axis [47]. Low values correspond to the alignment according to the radial axis, while high values – to the circumferential one.

While looking at the heat maps of incline angle, I noticed that xylem cells aligned to the radial axis, phloem and periderm cells – to the circumferential one, while cambium showed a mixed population (Figure 31A-D). This polarity was not respected in *pxy* mutants until 4.5 wpg (Figure 31E, F, I, J) when phloem and xylem cells partially reached their tilting position similar to the WT one (Figure 31G, H, K, L).

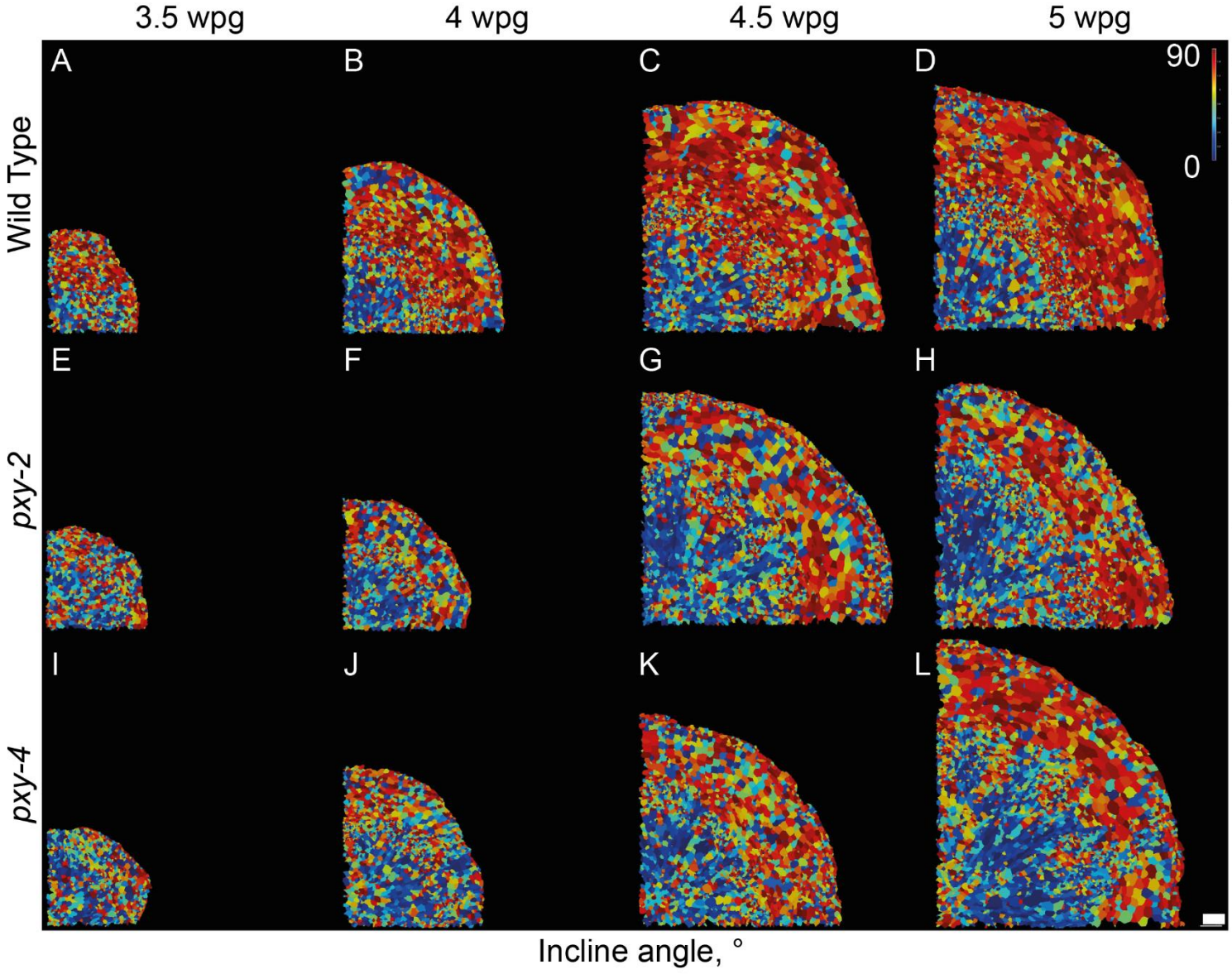

Figure 31. <u>Cell incline angle in wild type and *pxy* mutants hypocotyls during radial growth</u>. A-D. Wild type. **E-H.** *pxy-2*. **I-L.** *pxy-4*. **A, E, I.** 3.5 weeks post-germination (wpg). **B, F, J.** 4 wpg. **C, G, K.** 4.5 wpg. **D, H, L.** 5 wpg. The values in the calibration bar in **D** correspond to the angle between the cell major axis and the radial axis. The scale bar in **L** corresponds to 50 µm and applies to the whole figure.

This observation is supported by the shapes of violin plots for cell incline angle in different tissues. Indeed, for all genotypes, the plots are wide at low values for xylem tissues (Figure 32A, B), at high values for phloem ones (Figure 32E, F), while the violin plots are almost flat for cambium cells (Figure 32C). All of the violin plots with the exception of phloem fibers' ones (Figure 32D) show long tails towards the value opposite to the high-density value (Figure 32). This quantification explains the highly contrasted heat maps of incline angle not only between tissues, but also the salt-and-pepper contrasted pattern within the tissues (Figure 31). Interestingly the violin plots of incline angle look flatter for cambium, phloem parenchyma and periderm cells at 3.5 wpg in *pxy* mutants compared to the ones in WT (Figure 32C, E, F). This might be an artefact of cell type misclassification, because as mentioned higher, it was more tedious to distinguish cell types in *pxy* mutants at such an early developmental stage.

When I looked at the quantitative dynamics of cell incline angle in WT hypocotyl tissues, I saw that at 5 wpg, cambium and xylem parenchyma cells became more aligned to the radial axis than before (Figure 32B, C), while xylem vessels remained unchanged (Figure 32A) and phloem parenchyma cells got more aligned to the circumferential axis (Figure 32E). Periderm cells aligned more to the radial axis at 4 wpg then, tilted back towards the circumferential one at 4.5 wpg (Figure 32F).

The cell incline angle in hypocotyl tissues of *pxy* mutants followed different dynamics. Xylem parenchyma cells in *pxy-2* mutants started tilting towards radial axis earlier than WT – from 4.5 wpg on. This happened even earlier than that in *pxy-4* mutant – from 4 wpg on. This premature tilting explains the significantly lower incline angle of xylem parenchyma cells in *pxy-4* compared to *pxy-2* at 4 wpg. The incline angle additionally got lower in *pxy-2* compared to WT at 4.5 wpg. Interestingly the incline angle of xylem parenchyma cells reached the same value for all genotypes at 5 wpg (Figure 32B). The cell incline angle in *pxy* mutants was often inferior compared to WT in the case of cambium, phloem parenchyma and periderm cells except for a couple of cases like *pxy-4* phloem parenchyma cells at 4.5 wpg or *pxy-4* periderm cells when their incline angle was similar to WT (Figure 32C, E, F). Sometimes the incline angle of *pxy-4* cells got even lower that *pxy-2* like for cambium cells at 4 and 4.5 wpg (Figure 32C) or for periderm cells at 4.5 wpg (Figure 32F). The incline angle of xylem vessels was inferior in *pxy-2* compared to WT at 3.5 and 5 wpg, as well as inferior in *pxy-4* compared to WT at 4.5 and 5 wpg (Figure 32A). Phloem fibers were more radially aligned in *pxy-4* compared to the phloem fibers in WT and *pxy-2* (Figure 32D).

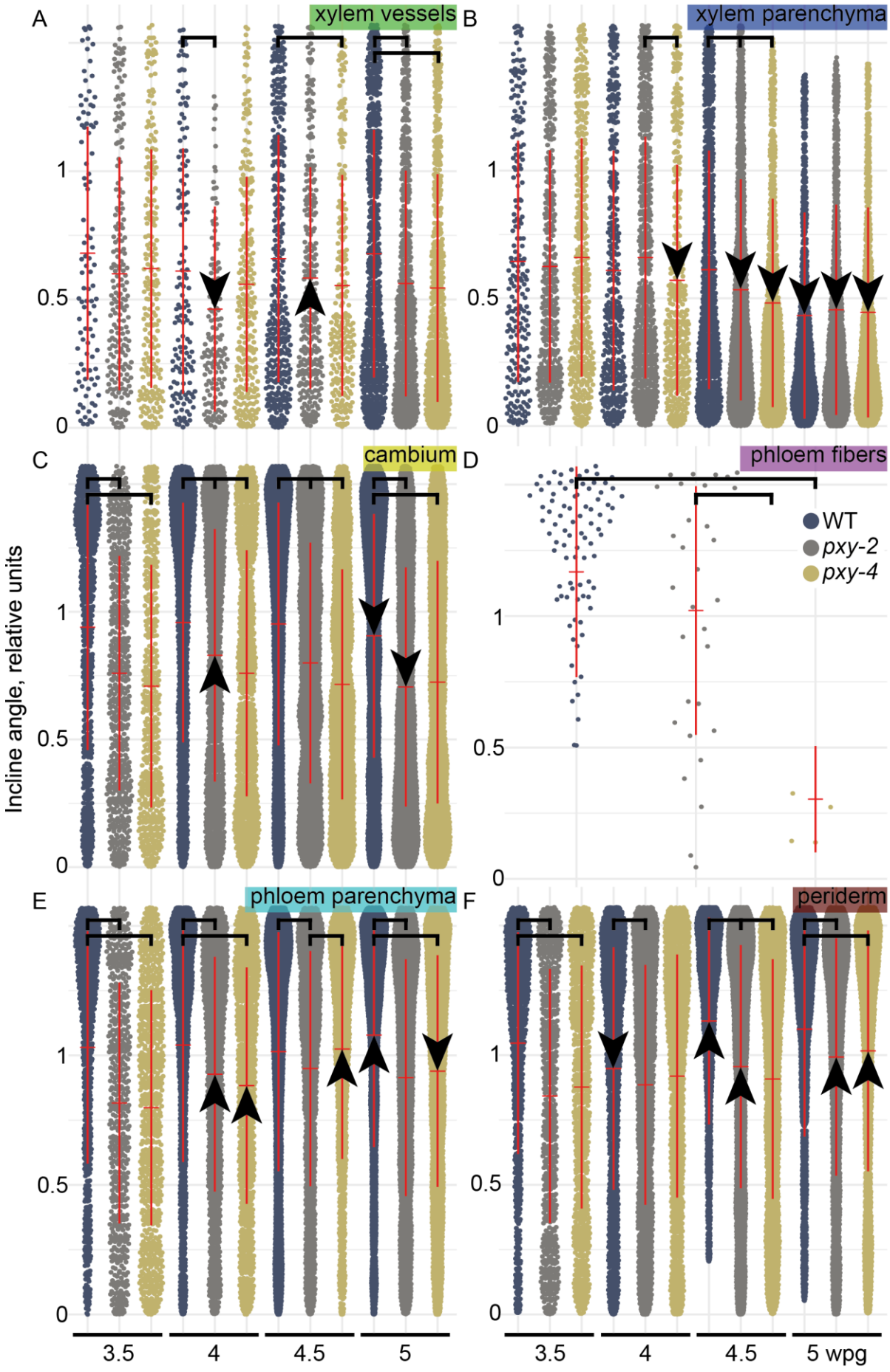
A
xylem vessels
B
xylem parenchyma
C
cambium
D
phloem fibers
E
phloem parenchyma
F
periderm
Incline angle, relative units
0
0.5
1
WT
pxy-2
pxy-4
3.5
4
4.5
5
5 wpg

Figure 32. Quantification of cell incline angle. Xylem vessels (**A**), xylem parenchyma cells (**B**), cambium cells (**C**), phloem fibers (**D**), phloem parenchyma cells (**E**) and periderm cells (**F**) were extracted from image segmentations and the incline angle was measured. The time points are indicated in the lower part of the image. The y-axa correspond to incline angle as indicated in the left part of the Figure. The genotypes are colour-coded and the legend is in the right part of the Figure. Cell types are indicated in the upper-right corners of every graph. Red horizontal bar in the middle of a violin-shaped dot plot indicates the mean, the vertical red bar indicates +/- standard deviation from the mean. The outliers were removed from the dotplot but were included into the calculation of the mean and the standard deviation. Arrows pointing up and down indicate a significant increase and decrease respectively in mean incline angle for the corresponding genotype compared to the previous time point (p-value < 0.05 after Kruskal-Wallis test on a single genotype group followed by a post-hoc pairwise Dunn test with Bonferroni correction and p-value < 0.05). Square brakets indicate a significant difference after a Kruskal-Wallis test on the single time point group followed by a post-hoc pairwise Dunn test with Bonferroni correction and p-value < 0.05. In the absence of arrows or square brakets, the difference is not significant with p-value > 0.05.

In summary, the incline angle shows a striking bimodal distribution across the radial axis of the WT hypocotyl. In *pxy* mutants, this polarisation is disturbed: cells are more tilted towards radial axis in tissues distal to xylem compared to WT. Xylem parenchyma follows a similar trend in *pxy* mutants as other tissues but reaches WT-like cell incline angle values at the last time point. The incline angle is also highly contrasted within the tissues at heat maps even though the quantification showed the presence of diagonally tilted cells. This might be an optical bias masked by cell size.

3.4.3.2. Cell degree

Cell degree corresponds to the number of adjacent cells (neighbours) to the considered cell. It depends on cell size of the considered and surrounding cells but also on the local arrangement of cells resulting from cell division and expansion [50]. The average degree of hypocotyl cells fluctuated between 5 and 7 in all genotypes (Figure 33).

The degree of WT cambium and periderm cells did not change over time (Figure 33C, F), while it decreased at 4 and 5 wpg for xylem vessels (Figure 33A), at 4.5 wpg for phloem parenchyma cells (Figure 33E) and increased at 4 wpg for xylem parenchyma (Figure 33B).

pxy mutants showed a different dynamic for the cell degree of hypocotyl cells over time. Cambium cells in *pxy-2* hypocotyls dropped in cell degree at 5 wpg while *pxy-4* hypocotyl cells increased in degree at 4.5 wpg then, dropped at 5 wpg (Figure 33C). Periderm cells degree rose at 4 wpg in *pxy-2* and at 5 wpg in *pxy-4* (Figure 33F). The degree of xylem vessels increased at 4 wpg and dropped at 4.5 wpg in *pxy-2*, while it dropped at 5 wpg in *pxy-4* (Figure 33A). The cell degree of phloem parenchyma cells remained unchanged over time in *pxy-2*, while it increased at 4.5 wpg and dropped at 5 wpg for *pxy-4* (Figure 33E). The cell degree of xylem parenchyma cells decreased at 4 wpg in *pxy-2* while it remained unchanged over time in *pxy-4* (Figure 33B).

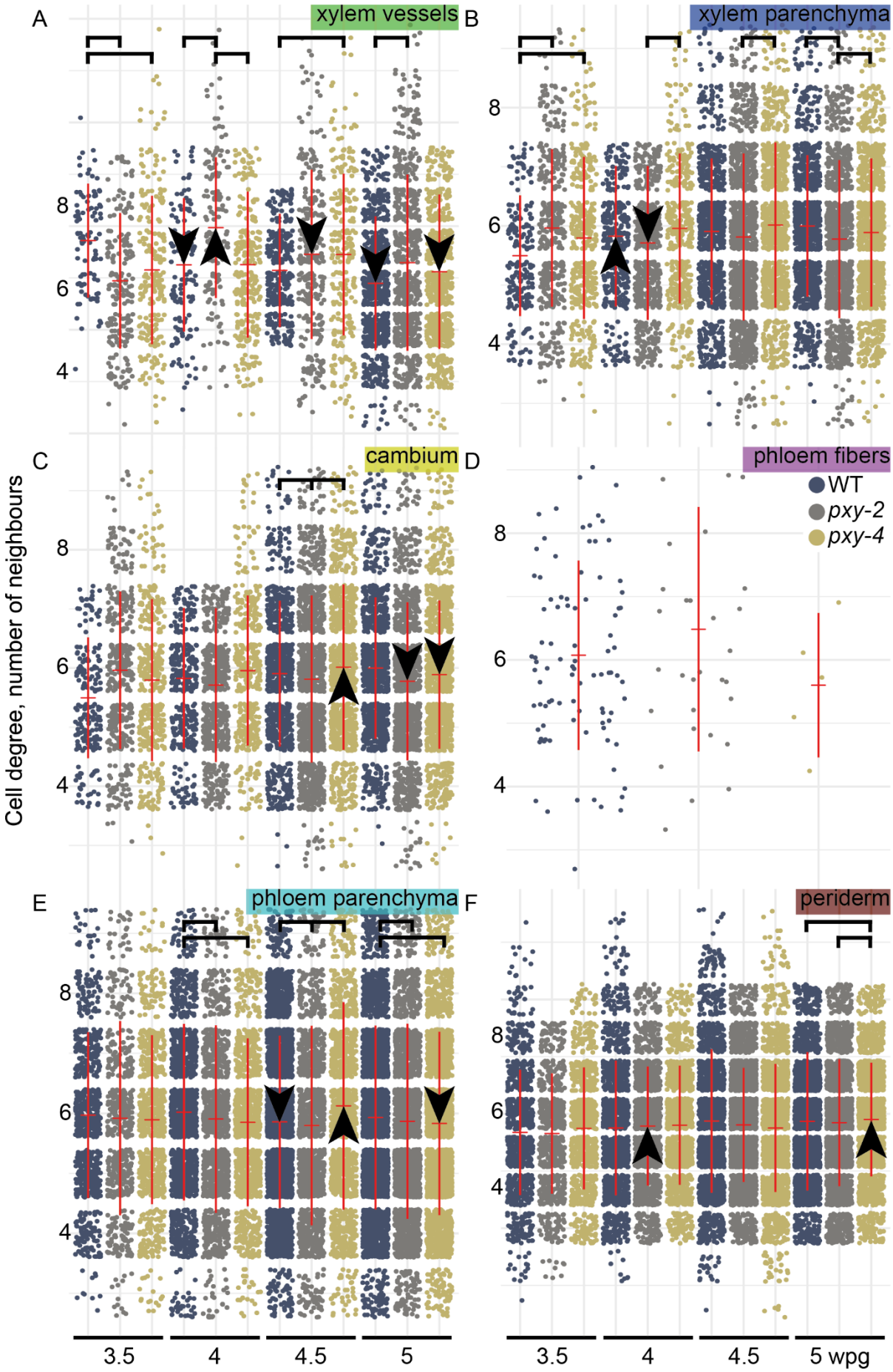
A
xylem vessels
B
xylem parenchyma
C
cambium
D
phloem fibers
WT
pxy-2
pxy-4
E
phloem parenchyma
F
periderm
Cell degree, number of neighbours
8
6
4
3.5
4
4.5
5
5 wpg

Figure 33. Quantification of cell degree. Xylem vessels (**A**), xylem parenchyma cells (**B**), cambium cells (**C**), phloem fibers (**D**), phloem parenchyma cells (**E**) and periderm cells (**F**) were extracted from image segmentations and the degree was measured. The time points are indicated in the lower part of the image. The y-axa correspond to minor axis as indicated in the left part of the Figure. The genotypes are colour-coded and the legend is in the right part of the Figure. Cell types are indicated in the upper-right corners of every graph. Red horizontal bar in the middle of a dot plot indicates the mean, the vertical red bar indicates +/- standard deviation from the mean. The outliers were removed from the dotplot but were included into the calculation of the mean and the standard deviation. Arrows pointing up and down indicate a significant increase and decrease respectively in mean degree for the corresponding genotype compared to the previous time point (p-value < 0.05 after Kruskal-Wallis test on a single genotype group followed by a post-hoc pairwise Dunn test with Bonferroni correction and p-value < 0.05). Square brakets indicate a significant difference after a Kruskal-Wallis test on the single time point group followed by a post-hoc pairwise Dunn test with Bonferroni correction and p-value < 0.05. In the absence of arrows or square brakets, the difference is not significant with p-value > 0.05.

At 4.5 wpg, the degree of cambium cells was the lowest in *pxy-2* and the highest in *pxy-4* (Figure 33C). At 5 wpg, the cell degree of periderm cells was higher in *pxy-4* than in WT or *pxy-2* (Figure 33F). At 3.5 wpg, the degree of xylem vessels was lower in *pxy* mutants compared to WT. At 4 wpg, *pxy-2* xylem vessels got the highest degree compared to WT and *pxy-4*. At 4.5 wpg, *pxy-4* xylem vessels degree was lower than the WT. Finally at 5 wpg, the degree of *pxy-2* xylem vessels was higher than in WT (Figure 33A). At 4 and 5 wpg, the degree of phloem parenchyma cells was lower in *pxy* mutants than in WT. At 4.5 wpg, it got higher in *pxy-4* than in other genotypes while the *pxy-2* level was still lower than the WT one (Figure 33E). At 3.5 wpg, the degree of xylem parenchyma cells in WT was lower than in *pxy* mutants while at 5 wpg, it was higher than the degree of xylem parenchyma cells in *pxy-2*. From 4 wpg on, the degree of xylem parenchyma cells was higher in *pxy-4* than in *pxy-2* (Figure 33B).

The heat maps confirm that most of hypocotyl cells had 5 to 7 neighbours in all genotypes (Figure 34). Unexpectedly the cell degree heat map (Figure 34) did not correlate with the area (Figure 19), perimeter (Figure 22) or aspect ratio (Figure 24) heat maps. Huge cells made an exception reaching 10 to 12 neighbours (Figure 19, Figure 34). These cells were mostly observed in the phloem of WT hypocotyls from 4 wpg on (Figure 34B-D) while in *pxy* mutants, cells with the highest degree were observed both in xylem and phloem at all developmental stages (Figure 34E-L).

In summary, I observed very subtle but significant variations of cell degree across developmental stages and all genotypes. This variation was higher in differentiating tissues than in proliferating ones. Qualitative data suggests that cell degree of hypocotyl cells depends on cell expansion at extremely high values but not at medium level. *pxy* mutants showed more high-degree-cells in phloem and xylem than in WT.

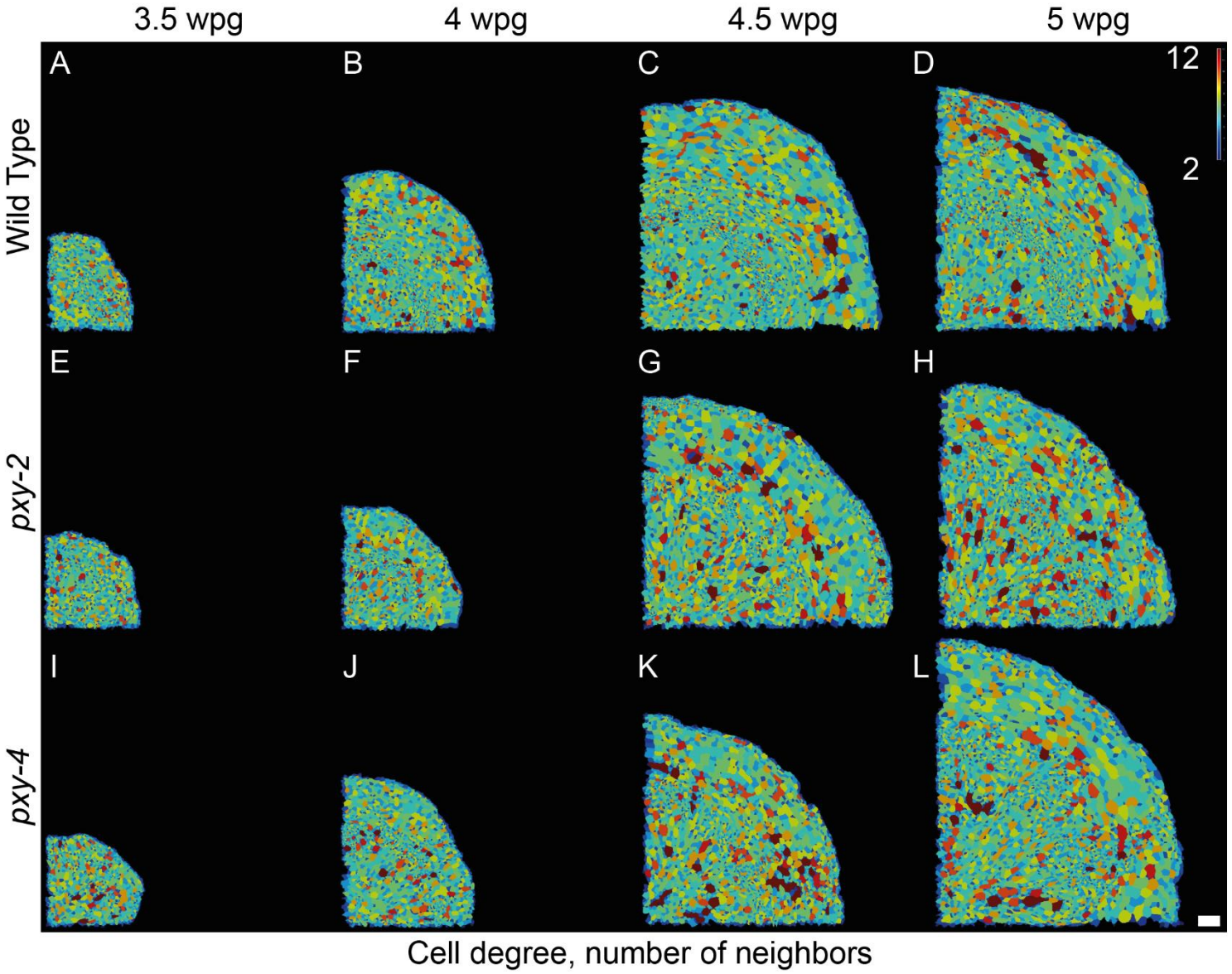

Figure 34. <u>Cell degree in wild type and *pxy* mutants hypocotyls during radial growth</u>. **A-D.** Wild type. **E-H.** *pxy-2*. **I-L.** *pxy-4*. **A, E, I.** 3.5 weeks post-germination (wpg). **B, F, J.** 4 wpg. **C, G, K.** 4.5 wpg. **D, H, L.** 5 wpg. The values in the calibration bar in **D** correspond to the number of adjacent cells. The scale bar in **L** corresponds to 50 µm.

3.4.3.3. Betweenness centrality

The betweenness centrality (BC) represents how many paths can be taken through the considered cell while "travelling" between all the possible couples of cells. Used as a connectivity measure in graph theory, it can predict the probability that the considered cell will serve as a transport hub for a molecule passively diffusing between cells [46]. The BC of most of hypocotyl cells in all genotypes tended to 0 especially with age. This could be observed with the flattening of BC violin plots towards 0 (Figure 35).

In WT, the BC decreased at every time point for cambium and phloem parenchyma cells (Figure 35C, E), at 4 and 5 wpg for periderm cells (Figure 35F), at 5 wpg for xylem vessels and xylem parenchyma cells (Figure 35A, B).

BC of cambium cells followed the same trend at 4 and 4.5 wpg in *pxy* mutants as in WT, but at 5 wpg, the BC of *pxy* cambium cells stopped decreasing (Figure 35C). At 4 wpg, the BC of *pxy* phloem parenchyma cells followed the same trend as WT, but at 4.5 wpg, it reversed towards an increase. At 5 wpg, the BC of *pxy-4* phloem parenchyma cells followed again the same trend as WT, but the BC of *pxy-2* phloem parenchyma cells remained the same as at 4.5 wpg (Figure 35E). The BC of *pxy-4* xylem parenchyma cells followed the same trend over time as in WT but in *pxy-2*, it gradually decreased starting from 4 wpg and stabilised at 5 wpg (Figure 35B). The BC of periderm cells in *pxy-2* hypocotyls followed the same trend as in WT at 4 and 5 wpg but additionally decreased at 4.5 wpg, while the BC of *pxy-4* periderm cells decreased only at 4.5 wpg (Figure 35F). The BC of *pxy-2* xylem vessels increased at 4 wpg then, decreased at 4.5 and 5 wpg, while the BC of *pxy-4* xylem vessels followed the same trend as in WT (Figure 35A).

The BC of cambium cells was higher in *pxy-2* than in WT and lower in *pxy-4* than in WT at 4.5 wpg, while it was lower in *pxy-2* compared to both WT and *pxy-4* (Figure 35C). The BC of phloem parenchyma cells was lower in *pxy* mutants than in WT at 3.5 wpg while the BC of *pxy-2* phloem parenchyma cells was higher than the BC in WT and *pxy-4* at 4.5 wpg (Figure 35E). The BC of xylem parenchyma cells was higher in *pxy-2* than in WT or *pxy-4* at 3.5 wpg, while it got lower in *pxy-2* than in WT or *pxy-4* from 4 wpg on (Figure 35B). The BC of periderm cells was lower in *pxy* mutants than in WT at 4 wpg then, it was lower in WT and *pxy-2* compared to *pxy-4* (Figure 35F). The BC of xylem vessels was lower in *pxy* mutants than in WT at 3.5 wpg. At 4 wpg, it was higher in *pxy-2* compared to WT and *pxy-4*. At 4.5 wpg, it was higher in *pxy-4* than in *pxy-2* (Figure 35A).

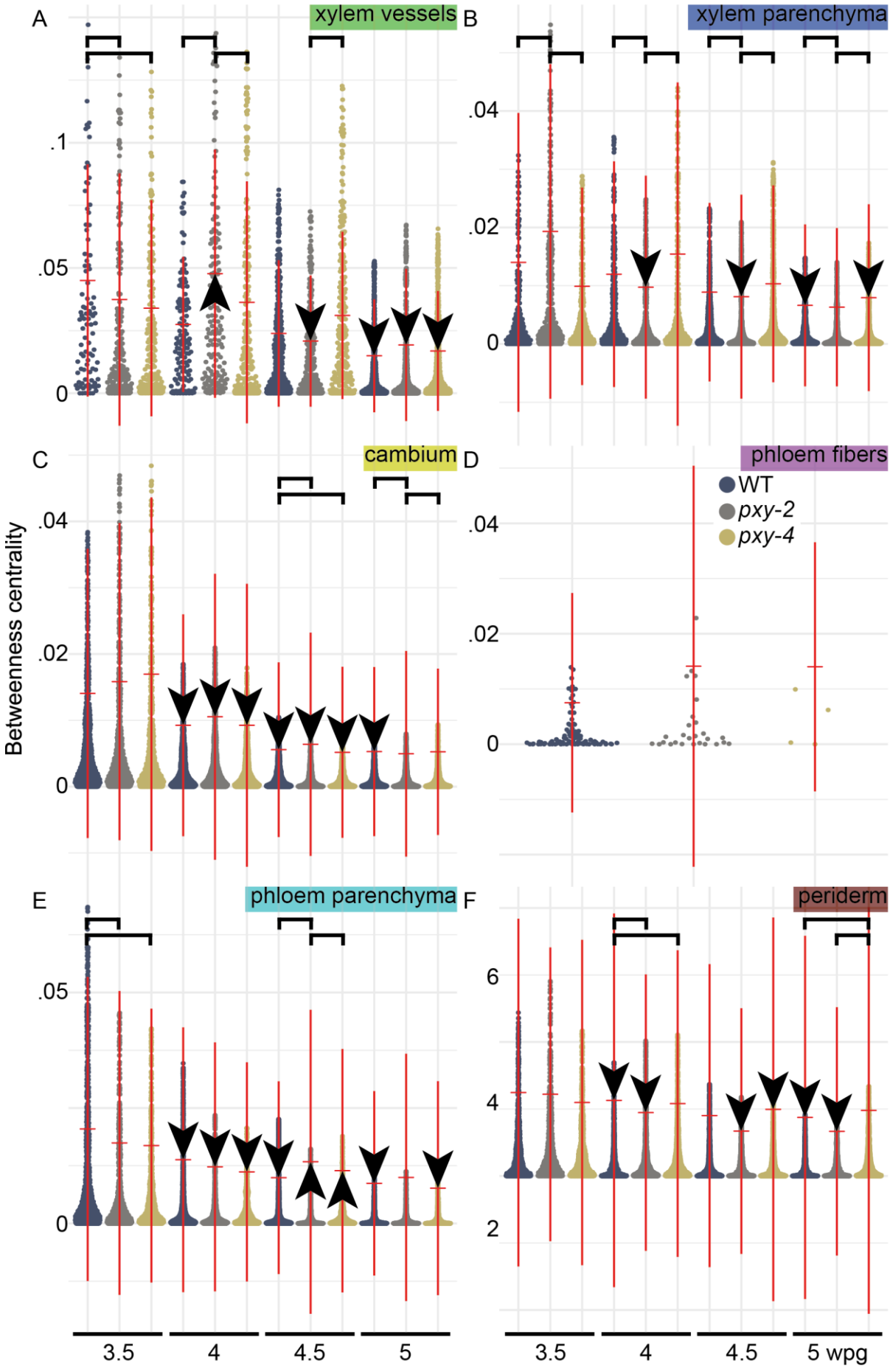
A
xylem vessels
B
xylem parenchyma
C
cambium
D
phloem fibers
E
phloem parenchyma
F
periderm
Betweenness centrality
WT
pxy-2
pxy-4
0
.05
.1
.02
.04
2
4
6
3.5
4
4.5
5
5 wpg

Figure 35. Quantification of cell betweenness centrality. Xylem vessels (**A**), xylem parenchyma cells (**B**), cambium cells (**C**), phloem fibers (**D**), phloem parenchyma cells (**E**) and periderm cells (**F**) were extracted from image segmentations and the betweenness centrality was measured. The time points are indicated in the lower part of the image. The y-axa correspond to betweenness centrality as indicated in the left part of the Figure. The genotypes are colour-coded and the legend is in the right part of the Figure. Cell types are indicated in the upper-right corners of every graph. Red horizontal bar in the middle of a violin-shaped dot plot indicates the mean, the vertical red bar indicates +/- standard deviation from the mean. The outliers were removed from the dotplot but were included into the calculation of the mean and the standard deviation. Arrows pointing down indicate a significant decrease in mean betweenness centrality for the corresponding genotype compared to the previous time point (p-value < 0.05 after Kruskal-Wallis test on a single genotype group followed by a post-hoc pairwise Dunn test with Bonferroni correction and p-value < 0.05). Square brakets indicate a significant difference after a Kruskal-Wallis test on the single time point group followed by a post-hoc pairwise Dunn test with Bonferroni correction and p-value < 0.05. In the absence of arrows or square brakets, the difference is not significant with p-value > 0.05.

The BC heat maps represent this contrasted distribution of numerous hypocotyl cells with null BC and only a few of them with low, medium and high BC values observed in violin plots previously. But the most interesting and unexpected pattern I observed during the quantitative histology analysis was the reticulate pattern of high BC values formed in hypocotyl tissues (Figure 36). In WT, the highest BC values were observed in distal phloem aligned circumferentially. I observed medium BC values in cambium aligned radially and interspersed by zones of cells with null BC values. Towards the centre of hypocotyl, this pattern lost its radial alignment and looked like a spider web. The number of cambium "cell roads" of medium BC was around 2-3 regardless of plant age (Figure 36A-D). The cambium roads amount of low BC was 1-2 at 3.5 and 4 wpg (Figure 36A, B), while it increased to 5-7 from 4.5 wpg on (Figure 36C, D). The space between the cambium roads looked stable over plant development (Figure 36A-D).

The BC in *pxy* mutants maintained a reticulate pattern but lost its proximal-distal polarity pattern with *PXY* at 3.5 wpg (Figure 36A, E, F). From 4 wpg on, the circumferential alignment of phloem cell roads, the radial alignment of cambium cell roads and the xylem "spider web" patterns were restored to WT resemblance (Figure 36B-D, F-H, J-L). Strikingly the high BC values occurred more often in cambium and xylem of *pxy* mutants than in WT (Figure 36).

In summary, the BC of hypocotyl cells showed surprising results in terms of average values and heat map patterning. The BC decreased with plant age for all genotypes except for some anomalies in *pxy* mutants. I observed some subtle and unique differences in BC level of hypocotyl cells between *pxy-2* and *pxy-4* mutants. The non-null BC values agglomerated into circumferential cell roads in phloem, radial cell roads in cambium and spider webs in xylem regularly interspersed by zones of null BC. In WT, the phloem cell roads had the highest BC values, cambium cell roads had medium and low BC values, xylem spider web – medium and low BC values. In *pxy* mutants, the highest BC values appeared also in cambium and xylem (Figure 36).

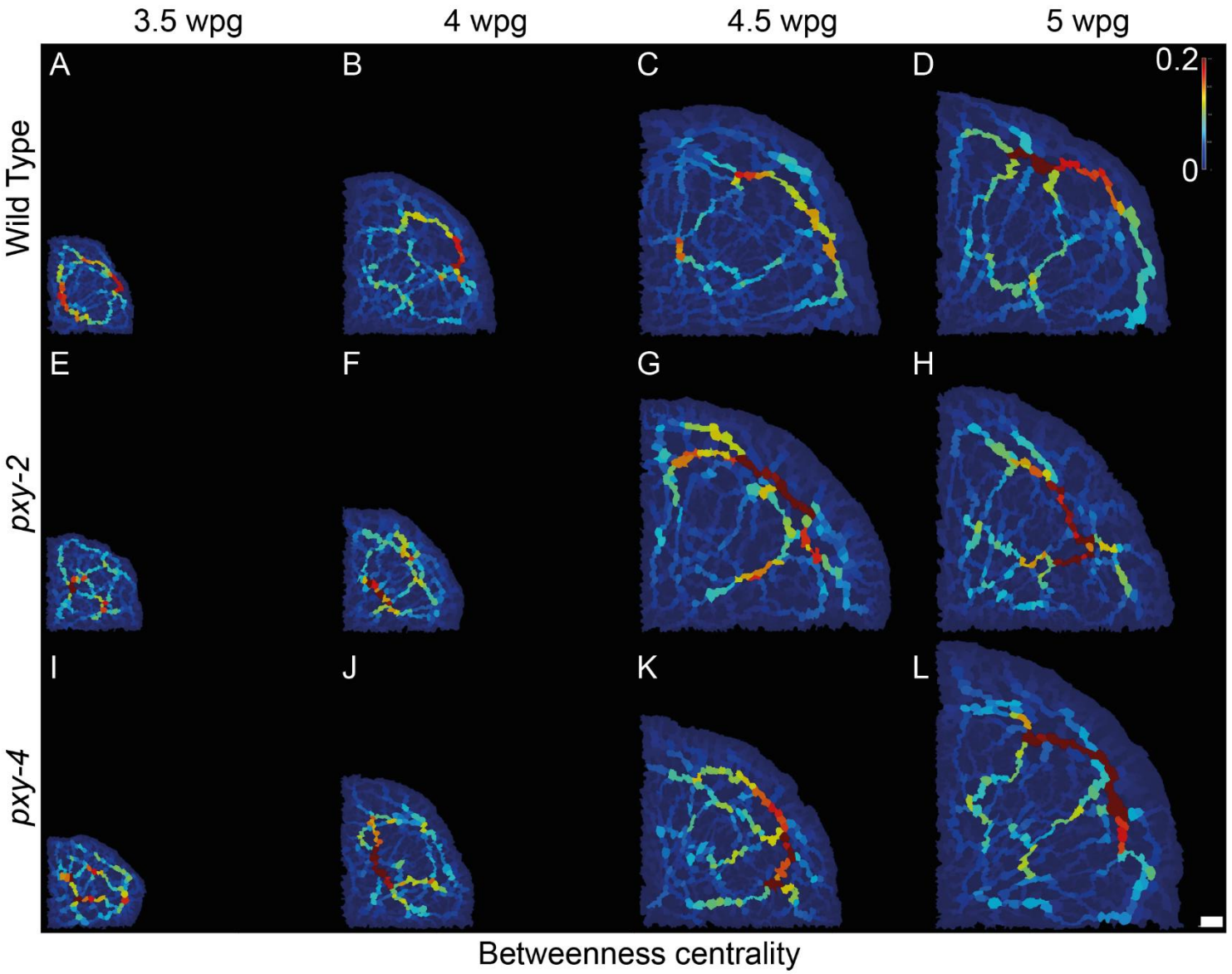

Figure 36. **<u>Cell betweenness centralty in wild type and *pxy* mutants hypocotyls during radial growth</u>**. **A-D.** Wild type. **E-H.** *pxy-2*. **I-L.** *pxy-4*. **A, E, I.** 3.5 weeks post-germination (wpg). **B, F, J.** 4 wpg. **C, G, K.** 4.5 wpg. **D, H, L.** 5 wpg. The values in the calibration bar in **D** correspond to the sum of the ratios between the number of the shortest paths between two other cells containing the cell and the number of the shortest paths between the two other cells. The scale bar in **L** corresponds to 50 µm.

To summarize the analysis of the topology of hypocotyl tissues, the three measurements revealed various properties of hypocotyl tissues at different developmental stages and genotypes. These topological properties are unique to adult hypocotyl tissues considering the huge number of cells, the diversity of their morphology and the radial symmetry of the whole organ. Therefore, hypocotyl appears as a perfect organ model to reveal the power of topological measurements as incline angle, cell degree and BC.

3.5. Quantification of tissue production

One of the most important information to get from radial growth analysis is the estimation of tissue production. It can be measured at different time points of plant development as thickness or surface of the considered tissues. In quantitative histology, the sum of the area for all cells of a specific cell type corresponds to the respective tissue size.

All tissues of all genotypes increased in surface at 4 and 4.5 wpg which promoted the increase of the whole hypocotyl diameter. At 5 wpg, WT and *pxy-2* cambium, phloem parenchyma and xylem vessels tissue grew larger while in *pxy-4*, all tissues increased in size promoting an additional growth of hypocotyl diameter (Figure 37). Interestingly cell production analysis showed a significant increase in cell number only at 4.5 wpg (Figure 15M) suggesting that cell expansion plays as much important role in radial growth as cell division. However, three plants used in the current quantitative histology analysis might not be enough to identify the precise time points when cell expansion contributes more to radial growth than cell division. At every time point, the tissue sizes were similar in all genotypes except for 3.5 wpg when *pxy-4* xylem vessels tissue was larger than WT (Figure 37).

In summary, quantitative histology is efficient to reveal radial growth over time as well as subtle differences in radial growth dynamics between *pxy-2* and *pxy-4*.

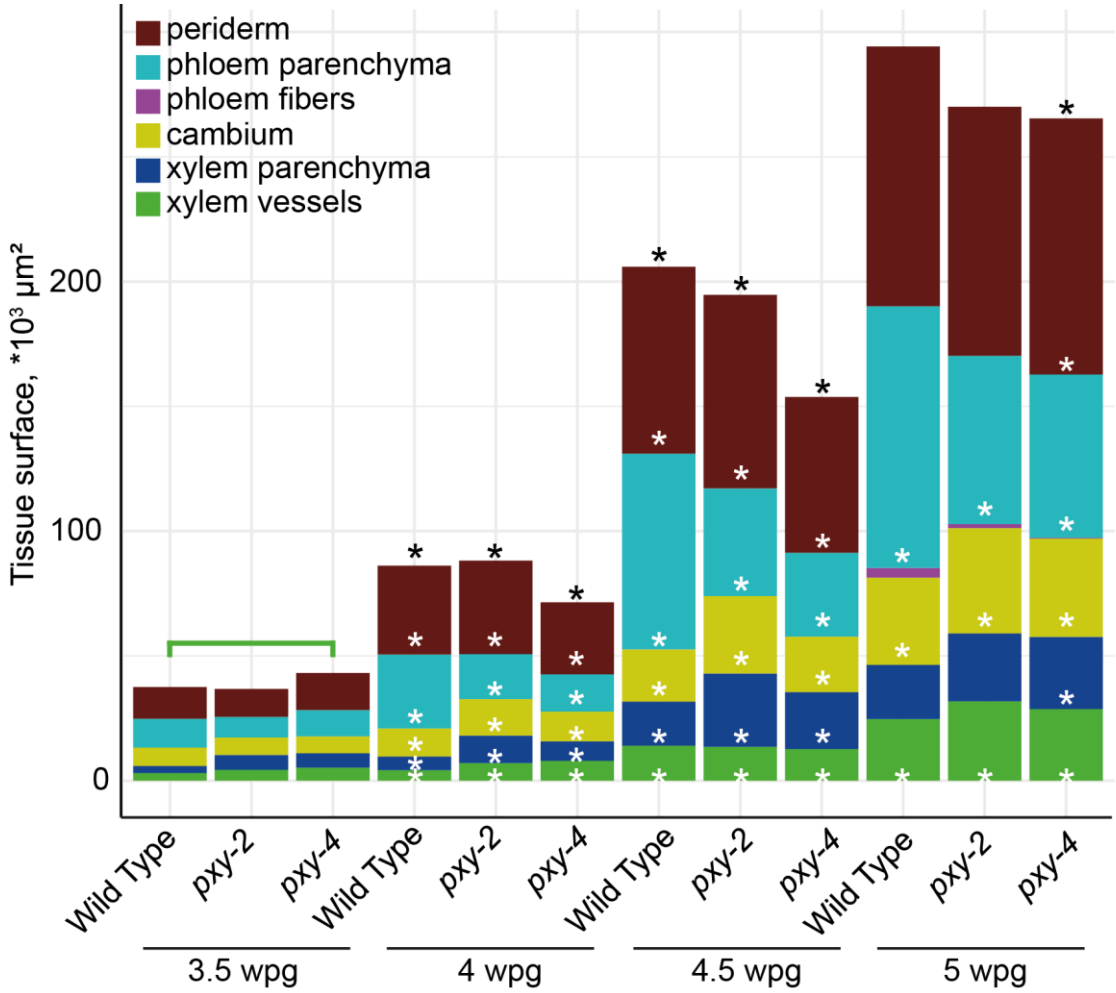

Figure 37. <u>Tissue surface quantification in wild type and *pxy* mutants hypocotyls during radial growth</u>. Tissue surface per time point, genotype and tissue type with n = 3 plants for each. White "*" indicate a significant increase for the corresponding tissue ($p < 0.05$ after Kruskal-Wallis test) compared to the previous time point (Dunn post-hoc test). Black "*" indicate a significant increase for the whole hypocotyl surface ($p < 0.05$ after Kruskal-Wallis test) compared to the previous time point (Dunn post-hoc test). The square bracket shows a significant differrence in tissue surface between WT and *pxy-4* xylem vessels tissue at 3.5 wpg. No more significant differences were observed between genotypes for other tissues at other time points.

Summarising the time-course analysis of radial growth in WT and *pxy* mutants with quantitative histology, I managed to obtain novel unbiased information on tissue production, cell morphology and tissue topology. Morphogenesis of hypocotyl cells and tissues was quantified. Quantitative histology revealed subtle differences between *pxy-2* and *pxy-4*. The limits of this technique lay in automated cell type classification that is hard to quality check in an unbiased way as well as in the level of noise due to the analysis of the total cell pool of a quarter of a hypocotyl.

Summarising all the results, I obtained a first insight of the effect of cell wall modifying proteins on hypocotyl morphogenesis, established a quantitative histology pipeline and demonstrated its power on classical *pxy* mutants. Ectopic vascular tissues-specific expression of cell wall modifying proteins or mutations in cell wall-related genes generates vascular tissues-specific but also pleiotropic phenotypes. The quantitative histology pipeline is based on commonly used tools like confocal microscopy, FIJI and R but as well as on cutting edge methods like plant tissues clearing with ClearSee, deep learning image segmentation with PlantSeg and their multidimensional analysis with MGX. With this method, I automatically quantified the differences between WT, *pxy-2* and *pxy-4* mutants in hypocotyl tissues morphogenesis for the first time. These results bring new insights into cell and tissue morphogenesis in the context of radial growth.

Discussion

The focus of this research project was the morphometric analysis of radial growth in *Arabidopsis thaliana* at tissue and cell level in the context of ubiquitous or inducible genetic alterations. For this, I used qualitative, semi-quantitative analysis as well as quantitative histology protocol. One of the questions was how cell wall properties affect cell and tissue morphogenesis in the context of radial growth. I investigated it with ectopic tissue-specific expression of genes coding for cell wall modifying proteins. I established a novel quantitative histology method based on cutting edge morphometric tools. This allowed me to discover new morphological and topological properties of hypocotyl tissues unseen by a naked eye.

Cell wall modifying proteins impact cell and tissue morphogenesis

In the context of investigating cell wall effect on cell and tissue morphogenesis, I used ectopic expression of genes coding for cell wall modifying proteins. I was interested in exploring the mechanical aspect of morphogenesis. Pectin was targeted as one of the key components of the cell wall influencing its mechanical properties. I ectopically expressed genes coding for pectin modifying proteins (called “effectors”) in a tissue-specific (with the help of “drivers”) and inducible manner (using Dex).

First, I tested the potency of the effectors by continuously inducing their expression in major plant tissues. My aim was to identify the effectors that induced substantial morphogenic defects that would be easily noticeable after a long induction. HAE-IDA receptor ligand module and VGD1 PME appeared to be the most potent ones among the tested effectors. Before going into radial growth specific phenotypes, I would like to discuss the results of continuous tissue-specific expression of these effectors.

I expected that ectopic expression of *HAE* and *IDA* would make the cell wall softer. After a constitutive expression of *HAE* and *IDA* in the cambium together with developing phloem (*pSMXL5>>)*, or the cambium together with xylem parenchyma tissues (*pPXY>>*), I observed various morphological phenotypes at plant, organ, and tissue levels. Counterintuitively cell wall loosening module induced a stunned plant development and a reduced radial growth. *HAE;IDA* was expressed in vascular tissues that follow the main axes of plant growth like roots, stems and leaf veins. Probably continuous loosening of cell walls disrupted mechanical polarities needed for anisotropic cell growth resulting in reduced tissue, organ and plant growth. Additional experiments demonstrating the effect of this receptor-ligand module are needed, because IDA could activate other receptors like HSLs [51]. To test

that transgenic *HAE* and *IDA* act in *cis* but not in *trans*, *HAE* or *IDA* could be expressed alone in the same tissue. For example, four transgenic lines could be analysed under Dex induction in the same time: *pPXY>>* driver, *pPXY>>HAE, pPXY>>IDA* and *pPXY>>HAE;IDA* driver-effector lines. If *pPXY>>HAE* and *pPXY>>IDA* show the same phenotype compared to *pPXY>>* driver, transgenic *HAE* and *IDA* would act only in cis. The other possibility to avoid endogenous receptors recognising transgenic IDA is to design an active version of HAE that would not need IDA to modify the cell wall.

I expected that ectopic expression of *VGD1* demethylesterifies pectin in the cell wall. This could result in stiffening or softening of the cell wall depending on the tissue context. Previous studies showed a strong potency of VGD1 as a PME resulting in stunt and stiff plants [26]. My experiments are in line with this observation. Ectopic continuous expression of *VGD1* in cambium and xylem parenchyma produced stunned plants with poorly proliferating and disorganised hypocotyl tissues. With a qualitative and semi-quantitative analysis, I observed a reduction in cell and tissue production suggesting that VGD1 indeed stiffens cells so much that radial growth could not occur neither via cell proliferation, nor via cell expansion.

After evaluating the drastic effects of HAE-IDA and VGD1 on plants upon their constitutive tissue-specific expression, I finally proceeded to their inducible tissue-specific expression during radial growth. Cambium together with xylem parenchyma zone was sensitive to these ectopic expressions.

HAE-IDA affected cell identity suggesting that potential cell wall loosening could have feedback on gene expression. However, the issue of IDA activating other intrinsic receptors remains and the effect of the induction could result not from cell wall modifications but from the activation of intrinsic HSL receptors by the transgenic IDA. In any case, after ectopic HAE-IDA expression, cambium together with xylem parenchyma zone lost their *PXY* activity highlighting the proximal cambium identity. It is tempting to speculate that these tissues changed their functional identity. It would be hard to test this hypothesis though.

VGD1 affected cell morphology of xylem parenchyma when expressed in cambium and xylem parenchyma zone. If VGD1 indeed has a stiffening effect, it would make sense that it prevented xylem parenchyma cell expansion. No flagrant phenotype was observed in cambium suggesting that cell wall mechanical properties did not affect cambium proliferation. This would also suggest that ubiquitous expression of VGD1 in my previous experiments and in previous reports had affected mostly cell expansion that consequently prevented the creation of space for proliferating cells. The other possibility is that in more differentiated tissues, VGD1 would promote acceleration of cell differentiation before allowing its sufficient expansion.

This idea was supported by the results I obtained from *VGD1* expression in xylem parenchyma that are on the way to differentiate into xylem fibres – *NST3* zone. After the induction of this

expression, these cells acquired a thicker cell wall resembling xylem fibres in xylem-II while in WT-like situation, this developmental stage was not achieved yet. One might argue that VGD1 had only cell wall level effect without any feedback on gene expression level. To counteract this argument, I suggest comparing this phenotype to the one acquired after ectopic expression of *VGD1* in cambium together with xylem parenchyma zone. *PXY* and *NST3* zones of expression overlap in xylem parenchyma. *VGD1* expression in the *PXY* zone did not result in thickening of cell walls the same way as it did in *NST3* zone suggesting that this phenotype is exclusive to ectopic expression of *VGD1* in xylem parenchyma differentiating into xylem fibers. That is why I would argue in favour of faster differentiation of xylem parenchyma into xylem fibers after ectopic expression of *VGD1* in *NST3* zone.

Cell identity is debatable. Different cell types can be defined by cell position, neighbours, morphology, subcellular characteristics, function, or gene expression. For example, the intersection of *PXY* and *SMXL5* zones of expression corresponds to cambium [31], *NST3* zone corresponds to xylem fibers [52] while *APL* to phloem poles [53]. However, *NST3* was also expressed in hypocotyl xylem parenchyma before plant flowering and formation of xylem II with xylem fibers (Figure 9E). In this case, functional cell type definition becomes more reasonable by looking at the properties of the cell walls with cell wall specific dyes or with the help of electron microscopy. Together with cell wall properties, cell position, neighbours and morphology served as reliable parameters for cell type definition and tissue ontology estimation in multitude of tree species [54]. I used this latter approach for cell type definition in the case of *Arabidopsis* (Figure 11, 15) that is discussed in the following chapter. When looking for an experimental approach to identify cell types, it becomes cumbersome to monitor all the cited criteria. In the case of this study, I investigated only the potential of changing hypocotyl tissues' identity with genetic methods. Future experiments to confirm these supposed identities will depend on the addressed scientific question. In the case of tissues ontology determination, pulse-chase experiments with induction and arrest of ectopic expression of *HAE-IDA* or *VGD1* could be realised to identify if the affected cells follow a differentiation or dedifferentiation pattern. In the case of transcriptomic cell identity definition, the expression of previously discovered tissue-specific genes could be visualised after the induction of effectors expression. In the case of functional tissue identity definition, electron microscopy could help to identify the subcellular structures after the induction of effectors expression.

The confirmation of cell wall modifications after effectors expression is still lacking in this study. Brillouin microscopy would help to remedy this issue. This cutting-edge method of biophysics and confocal microscopy allows to measure mechanical modulus of the biological material in a spatially resolved manner [55].

Even if the changes in mechanical properties of cell wall are monitored, the feedback mechanism towards genes expression should still be established. Three main mechano-transduction theories are offered. The first one consists in fluctuations in calcium content within the cell or the cell wall which would activate calcium signalling or Receptor-like kinases respectively [56]. The second theory is the signalling via FERONIA receptor that would sense mechanical stress exerted on the cell wall [57]. The third theory is mechano-transduction via microtubules. CMTs serve as a platform for CSCs. But they could also serve as a mechano-sensing mesh [57]. How microtubules would transform a mechanical message into a gene expression pattern is still unknown. What could be done to unveil this process is to investigate the cell wall-to-genes mechano-transduction pathway in real time. Inducible tissue specific expression of genes coding for cell wall modifying proteins can be done in a pulse-chase manner. This approach will allow to understand if normal morphogenesis is rescued when the effector expression is stopped. Brillouin microscopy of the modified cell walls will confirm these mechanical modifications. Confocal microscopy of microtubules labelled with fluorescent proteins will show how the microtubules react to these changes in cell wall mechanical properties. Finally, promoter-reporter expression of the key genes will give an insight on the cell identity changes. All these methods are already available, but the real challenge will be to combine them while keeping a high temporal resolution.

In the context of the current study, the achievement consists in identifying two morphogenic effectors: HAE-IDA receptor-ligand module and the PME VGD1. I tried other PMEs and PMEIs as effectors and have not observed any strong effect. This might be due to the silencing of the transgenes or to the fact that PME3, PME5, PMEI3 or PMEI5 alone cannot induce substantial changes in the cell wall chemical structure. Indeed, PME and PMEIs are large families of proteins consisting of dozens of members [27]. Their enzymatic activity has been studied in vitro, but due to the complex cell wall composition, cannot be easily estimated in vivo. Previous studies showed some significant morphogenic effects from an ectopic expression of these PMEs and PMEIs in the epidermis of a young hypocotyl [24], but they did not have such an effect in the context of the vasculature. VGD1 was a surprising exception in my study showing a strong morphogenic effect. This effector could be used in further investigations.

The morphogenic effects caused by loss-of-function or gain-of-function mutations in genes coding for cell wall modifying proteins were analysed here only qualitatively or in a semi-quantitative way. So, I proceeded then with the establishment of a quantitative histology tool. This tool was not firstly tested on the preliminary results I obtained from cell wall modifications, but on vascular mutants that had already been previously investigated. This way, the quantitative histology protocol gained a more reliable proof-of-principle confirmation.

Quantitative histology is a powerful phenotyping method

Cell segmentation with the help of neural networks was used for the first time on the confocal images of hypocotyl sections. Previously, it was possible with bright field imaging of extremely high quality to get a proper segmentation with only a few needed corrections [47]. Confocal microscopy is preferable nowadays because it can be combined with a large diversity of fluorescent labelling. But before this study, proper cell segmentations were only possible on young hypocotyls [46] or xylem [58]. In old hypocotyls, there is more heterogeneity in cell size and mechanical properties of different tissues, making the imaging noisier and the segmentation more challenging. The CNN used for segmentation in PlantSeg clearly solved this issue.

I had to generate 25 images of ground truth to train the CNN. Interestingly the same boundary prediction model was trained on the images of different organs: ovule, SAM and hypocotyl sections. The input from different organs improved the model in segmenting hypocotyl sections. So, the example of this study shows that the boundary prediction CNN models can be crossed over different organs. It is interesting to test how the model I trained would perform on other organs previously unseen by it. On one hand, a highly trained model could get only better in segmenting any similar image. On the other hand, this model could recognise the details in hypocotyl that would not be important in another organ. Still, a general segmentation workflow capable of recognising boundaries and shapes in any context in the same way as a human eye remains the goal of modern image analysis.

In the case of the old hypocotyl, one of the details that I struggled to deal with while correcting the segmentations were intercellular spaces. They are not visible in cambium but very prominent in distal phloem for example. Taking them into account resulted in teaching the boundary prediction model to not omit cambium cells that are of a similar size but positioned at another point of the tissue. At the same time, including intercellular spaces into the cell pools increased the noise in the subsequent cell morphology analysis. In future, one could apply cell size and polar coordinates filters to sort the intercellular spaces out of the analysis. Alternatively this filtering at the very first step of analysis could be another goal for the design of boundary prediction models.

As mentioned above, the cell type classification is prone to specialist bias. I suppose that a bias for cell boundaries identification exists too because of imaging artefacts. This is not only an issue of modern imaging. Before the introduction of cameras in microscopy, scientists would make sketches of their observations. When these observations are reproduced nowadays the real microscopy images can differ from the old hand drawn pictures. When an expert must generate ground truth for boundary prediction models, he or she comes back to the sketching technique and can be prone to the same biases as scientists had hundred years ago. In computer sciences, this can be avoided by

proofreading the ground truths by several users. However, this is too cumbersome in workload for the academic level. Perhaps citizen science and science gamification could afford the workforce to at least estimate how strong this observation bias is.

The segmentation scores showed a high improvement of the boundary prediction model after every round of training. This was also confirmed by the reduction of time I spent on correcting the segmentations at every training iteration. However, a set of three images showed that the distribution of cell size (area) is different between the segmentations produced by the boundary prediction model and the ones that I corrected. This might be due to the intercellular spaces and the imaging biases unrecognisable by human eye but recognisable by the machine. The other possibility is that the model is not trained enough. It could be trained further and with different computational methodology. My collaborator Lorenzo Cerrone (supervised by Fred Hamprecht) tried different methodologies for boundary prediction models. As with most of modern computational models, the main hurdle consists in parameters adjustment. Even if some unbiased methodologies of parameters adjustment were offered by the scientific community [59], CNNs usually have an unpredictable, a “black box” behaviour requiring manual settings [37]. From the biologists’ side, more ground truth can be generated for further training of the model.

There is the general opinion that a specialist of the field would do a better cell type classification than less specialised people [36]. After asking my colleagues who have different levels of expertise in plant vasculature, I realised that there is no such issue. Different experts chose more or less broad set of cell types but respected a general subdivision into five classes of tissues that could be also recognised automatically by the machine: xylem vessels, xylem parenchyma, cambium, phloem, periderm. It would be interesting to do a similar social study on biologists from other fields, as well as on random users to see if they would also choose a set of five tissue classes. I suspect that the results will be close to the ones obtained from my colleagues. In the future, cell type classification could be also realised by citizen science and science gamification if the users would read a short introduction in the field of plant vasculature.

Another way to do cell type classification is to omit automated SVM classification of all cells and choose a filtering approach. A user could select cells at specific polar coordinates range with specific morphology and fluorescent staining for example. This could be a more targeted approach depending on the scientific question. Additionally, selecting only a couple of measurements for cell type classification, the user could avoid the misclassification artefacts that I met when analysing *pxy* mutants. Radial coordinate appeared as one of the most important cell attributes for the classification in my study but also in a previous report [58]. In the case of *pxy* mutants, the radial symmetry is disrupted which would motivate to omit radial coordinates from the classification. SVM classifier has

a set of parameters that can be manually adjusted. Hopefully in future, it would be possible to grade the "importance" of every cell descriptor in its classification. Tissue-specific fluorescent markers will also improve the classification like lignin staining did in the current study.

I applied the quantitative histology method on hypocotyl sections of different plants, genotypes and developmental stages. I decided to pool all the cells from three plants per genotype and developmental stage. This might have added some noise when I analysed the mean values of the 13 quantitative measures. The standard deviation bars were too large. It would also be possible to analyse plants separately to stay more statistically rigorous. Alternatively, one could apply stronger filters for selecting homogeneous cells for the quantitative analysis. This latter approach would help to eliminate intercellular spaces but would also add a bias in the analysis. A potential future improvement of the quantitative histology protocol would be to generate a KNIME (knime.com) protocol to facilitate the exchange of files at different image processing steps.

A cutting-edge technology often meets unpredictable technological and conceptual issues. Despite them, neural networks showed their strength in improving computational tools in different fields. The segmentation protocol I developed here with the help of the computational tools from our collaborators has shown its power and can be used for future projects.

Quantitative histology reveals new properties of *pxy* mutants

I grew *Arabidopsis* plants with WT, *pxy-2* and *pxy-4* genetic backgrounds and analysed their radial growth. For this, I collected their hypocotyls at different time points, sectioned and stained them with cell wall specific dyes. I imaged the sections with confocal microscopy and segmented the images with the quantitative histology protocol described above. Previously, *pxy* alleles were analysed only in a qualitative or semi-quantitative manner describing their phenotype as "stronger" or "weaker" [43]. Here, I managed to quantify these differences in an unbiased manner. Quantitative histology clearly revealed significant differences between *pxy-2* and *pxy-4*. For some measurement, one mutant allele was even comparable to WT while the other one was very different. However, I could not identify any consistent trends between the two mutant alleles. Meanwhile several differences were observed between different developmental stages as well as between WT and *pxy* mutants.

On the single cell level, cell wall composition and cell morphology were affected in *pxy* mutants compared to WT. On the tissue level, tissue topology changed with the loss of *PXY* but not total radial growth on itself. Therefore, *PXY* is responsible for cell and tissue morphogenesis in hypocotyl but not for cell or tissue production. This is a counterintuitive observation, but it shows that cell division orientation and/or cell expansion rate can be affected without impeding the radial growth. This is in

line with the recent study showing that only multiple *pxy* and *pxy*-like loss-of-function mutants can result in the reduction of radial growth [16].

For the first time, the phenotype of *pxy* periderm was presented here. At late developmental stages, *pxy* periderm cells are more circular than WT ones while *pxy* phloem is overcompressed. This phenotype might have resulted from a failure of phloem cells to expand. In this case, phelloderm cells would not have any mechanical obstacle to expand more isotropically and acquire a circular shape. *PXY* could be responsible for phloem expansion. No reports of such a role for *PXY* were suggested so far. To confirm such hypothesis *pxy* mutants could be complemented with *PXY* expressed under the control of a phloem-specific promoter. The promoters of *SMXL*s family genes could serve for this purpose. Unveiling such a subtle phenotype as the cell shape is one of the strengths of the quantitative histology protocol developed here.

With the loss of phloem expansion in *pxy* mutants, the neighbouring phelloderm was affected probably due to the absence of the pressure from the phloem. This idea suggests that changes in mechanical properties of a neighbouring tissue affected phelloderm cells morphogenesis. But phellogen cell division orientation was not affected, because phelloderm was still organised in proper cell files. It would be interesting to express genes coding for cell wall loosening proteins in phellem in an inducible manner and visualise its effect on phellogen cell division orientation. Periderm might be a more suitable meristem model than cambium for testing the relation between cell wall mechanical properties and cell division orientation for two reasons. Firstly, periderm is positioned at the periphery of hypocotyl and is not affected by geometrical biases of the centre of the cylinder. In other words, periderm is less affected by topological restrictions by covering a distal ring of hypocotyl, while vascular tissues cover a full inner disk of hypocotyl and are restricted by this geometry (Figure 1A). All cork tissues can thus be approximated to two dimensions with less biases than vascular tissues. Secondly, phellem produces exclusively one type of tissue in every radial direction which simplifies the modelling of mechanical processes.

The analysis of *pxy* mutants in the context of radial growth was discussed here in the gene-focused manner. But quantitative histology revealed more generalist questions of developmental biology.

New insights in cell and tissue morphogenesis

Hypocotyl serves as a unique organ model to study cell and tissue morphogenesis in all its diversity. Thousands of cells composing it show a huge diversity of shapes, cell wall composition and spatial arrangement resulting in peculiar tissue shapes. Comparing hypocotyl cells and tissues

morphology at different moments of development and between different genotypes challenged some generalist assumptions of developmental biology.

Counterintuitively cell volume and surface (respectively area and perimeter in the 2D context) show different distribution within tissues even though these two measures are correlated by geometric definition. In biological context, cell surface gets out of correlation with cell volume when cells develop more irregular shapes. This looks to be specifically the case for phloem cells that expand anisotropically. Another unexpected loss of correlation is between cell size and cell degree. Previous studies showed that with the increase in the cell size, the cell degree increases too [50]. But this is not the case for hypocotyl cells that show a randomly distributed cell degree across tissues with the exception of some huge cells reaching the highest cell degree. Interestingly these spots of high degree cells were more numerous in *pxy* mutants suggesting that the cell degree measure is an indicator of tissue organisation.

The orientation pattern of hypocotyl cells according to the radial axis reported previously was confirmed in the current study [47]. The major axis of xylem cells aligned with the radial axis, the major axis of phloem cells aligned with the circumferential one, while the major axis of cambium oscillated between both. The loss of radial symmetry in *pxy* mutants, can be visualised in the loss of this patterning. Therefore, the incline angle representing this alignment is an important measure to use in other mutants' analysis.

A peculiar property was observed for lobeyness distribution across tissues. It acquired a unique checkboard pattern of highly lobeyed cells surrounded by medium lobeyed ones (Figure 30). The other interesting property of lobeyness is its variation over time. It showed a sinusoidal variation for differentiated tissues in all genotypes (Figure 29). It is difficult to speculate the origin of these patterns with the data at hand. It would be helpful to compare hypocotyl tissues with abstract geometrical structures. For example, a sector subdivided in regularly spaced geometric forms mimicking cells but bringing the morphological complexity to a minimum would be a perfect control for a quantitative analysis of hypocotyl sections. This approach will show if the lobeyness checkboard pattern and sinusoidal variation over time are intrinsic topological properties or developmental properties of specific tissues. For example, a molecular signalling could regulate the lobeyness patterning while fluctuations in radial growth could define the fluctuations in lobeyness.

Betweenness centrality of old hypocotyl cells was measured for the first time (Figure 35, 36). This measure is a more powerful estimation of tissue topology and cell connectivity than cell degree [40]. BC is particularly relevant for vascular tissues because BC is supposed to estimate the intercellular flow of molecules – the main function of plant vasculature. It looks coherent that "cell roads" are oriented circumferentially in phloem and radially in cambium, because the photosynthates would flow

across phloem circumferentially and towards cambium and xylem radially. Unexpectedly this transport is predicted by BC in cell roads pattern rather than in radial fronts. Future experiments with fluorescent molecules travelling from phloem or xylem towards other tissues will elucidate if this prediction is true. This tissue topology might have been selected during evolution because it provides a more efficient radial and circumferential transport of molecules than another tissue topology. There is a huge diversity of vascular morphologies across species [54]. It would be interesting to calculate the BC of their cells and realise the transport experiments with labelled molecules too. This approach would bring an insight into how molecular transport evolved and how plant tissues topology adapted to different environmental challenges.

The radial patterning of hypocotyl tissues forming bands of xylem, cambium, phloem and periderm is exceptionally consistent between individuals of *Arabidopsis*. This cannot be said about the circumferential patterning of xylem vessels and phloem fibers. From one individual to another, there is more or less xylem parenchyma between xylem vessels sectors. These sectors have more or less branching. Phloem fibers not only appear at precise developmental stages but also seem to respond to environmental stimuli like it happens in trees. Their circumferential pattern looks even more asymmetric that the circumferential pattern of xylem vessels tissue. Most of the time, phloem fibers are gathered in islands at the distal phloem but the cell number per island highly fluctuates. Nevertheless, xylem vessels still organise in sectors and phloem fibers are still more or less interspersed between each other. This is a clear sign of Turing's reaction-diffusion mathematical prediction when self-promotion of two factors and their mutual inhibition are sufficient to create regular patterns [60]. The break from a "perfect" regularity in xylem vessels and phloem fibers patterning might be due to the involvement of additional factors.

With the loss of *PXY*, if one analyses hypocotyl tissues at a later developmental stage when the flowering occurs, xylem vessels sectors get even further from each and are interspaced in a more regular way. At earlier stages that I analysed, *PXY* loss induced a "wavering" of cambium. So, interestingly *PXY* is involved in maintaining the regular radial patterning while disrupting the regular circumferential patterning of hypocotyl tissues. The former has already been extensively studied in the context of PXY-CLE41 signalling but analysed always in a flowering stage [42]. At the stage of the formation of these xylem vessels sectors in *pxy* mutants, cambium gets circumferentially fragmented together with xylem. Interestingly the patterning of cellulose content across middle-aged hypocotyls I analysed reminded this cambium fragmentation at the hypocotyls of the flowering plants (Figure 17). Therefore, differences in cell wall properties between genotypes might indicate earlier circumferential fragmentation of tissue in *pxy* mutants than reported before. It would be interesting to see if this fragmentation happens before the flowering stage by using cambium specific promoter-reporter

markers. PXY might inhibit some morphogen within xylem to prevent the xylem vessel regular sectors appearing in *pxy* mutants. The adjustment of the patterning with the help of a morphogen reminds Wolpert's theory on positional information which was reinterpreted later as "French flag" theory [61].

Historically Wolpert was opposed to Turing but in recent decades their theories were combined [62]. This can be observed in various organisms like for example, human fingers that are perfectly spaced one from another but have different morphologies. The spacing of fingers is regulated by the reaction-diffusion system while each finger's morphology is regulated by the positional information system. I suppose that a similar process exists in hypocotyls. Xylem vessel sectors are interspaced regularly by a couple of morphogens according to the reaction-diffusion system while PXY "smooths" this regularity according to the positional information system. Phloem fiber islands are interspaced regularly by a couple of morphogens (reaction-diffusion) while another morphogen regulates the cell number within these islands (positional information). The nature of these morphogens can be different: mRNAs, cell wall components, small peptides or hormones [17].

The combination of the reaction diffusion and the positional information theories of patterning can be also observed in BC distribution across hypocotyl tissues. Indeed, these cell roads are regularly interspersed in cambium but also have several "fractal levels" of connectivity. There are cell roads of high BC and cell roads of medium BC interspersed by zones of null BC. The number of cell roads for each "fractal level" seems to follow a constant pattern. This suggests that there is a consistent fractal patterning of hypocotyl cells' connectivity.

These ideas bring the quantitative analysis to a general questioning of the organisation of biological structures at different scales. On micro and macro level, the structures are very stereotypical like the components of a plant cell or the plastochron of leaves in rosettes respectively [9]. However, at mesoscale, the tissue level, there is more or less heterogeneity [50]. For example, the radial organisation of hypocotyl tissues is stereotypical, while the circumferential organisation of hypocotyl sub-tissues is more heterogeneous. By looking at higher level morphometric calculations like BC, one might scale up the mesoscale and find stereotypical patterns again.

This vision of combined reaction-diffusion and positional information mechanism can be applied to other plant organs and developmental processes. The geometry and topology of the analysed tissues should be taken in consideration. For example, cambium is a bipolar meristem producing two different tissues in opposed directions [63]. This is connected to the cylindric geometry of organs it composes like hypocotyl, stem, root or leaf veins. RAM and SAM are unipolar meristems producing tissues in one direction and limited by the dome morphology of root or shoot apex respectively [13]. The morphogenesis of meristematic tissues depends not only on the gradients of morphogens but also on the directionality of tissue production and the organ geometry.

To summarise the ideas generated and discussed in this thesis and to integrate them in the previously discovered molecular signalling regulating radial growth, I suggest that the unique cell and tissue morphology of *Arabidopsis* hypocotyl is acquired thanks to: (i) the expression of genes regulating vascular tissues development, (ii) the reaction-diffusion and positional information mechanisms involving hypocotyl morphogens, (iii) the intracellular, intercellular and intertissular mechanical interactions, (iv) the balance between stereotypic and heterogeneous organisation of the plant tissue mesoscale and (v) the cylindric geometry of hypocotyl. Every factor should be investigated with a proper choice of controls. Quantitative histology is a generalist method that can be efficiently applied in any research question targeting these factors of morphogenesis.

Conclusion

This study aimed to describe cell and tissue morphogenesis in the context of plant radial growth. Hypocotyl anatomy was described with quantitative histology in different genotypes in a timely resolved manner. New morphological and topological features were discovered. From now on, the phenotyping of vascular mutants can be done in a non-biased, quantitative way allowing to connect genes to their morphogenic function. The combination of reaction-diffusion and positional information mechanisms regulating tissue patterning was proposed for vascular tissues for the first time. Computational modelling of the proposed theory will bring a further understanding of vascular tissues morphogenesis and give ideas for future research in molecular signalling. Mechanical feedback from cell walls to cells is yet to be further explored. Hopefully the combination of quantitative experimental techniques and computational modelling in the field of developmental biology will bring a more integrated understanding of stereotypic and heterogenic organisation in plants.

References

1. Kaiser, D., *Building A Multicellular Organism.* Annu Rev Genet, 2001. **35**: p. 103-123.
2. Coppe, J.P., et al., *The senescence-associated secretory phenotype: the dark side of tumor suppression.* Annu Rev Pathol, 2010. **5**: p. 99-118.
3. Taguchi, A. and M.F. White, *Insulin-like signaling, nutrient homeostasis, and life span.* Annu Rev Physiol, 2008. **70**: p. 191-212.
4. Shimada, T., et al., *Plant Vacuoles.* Annu Rev Plant Biol, 2018. **69**: p. 123-145.
5. Tonn, N. and T. Greb, *Radial plant growth.* Curr Biol, 2017. **27**(17): p. R878-R882.
6. Chiang, M.H. and T. Greb, *How to organize bidirectional tissue production?* Curr Opin Plant Biol, 2019. **51**: p. 15-21.
7. Spicer, R. and A. Groover, *Evolution of development of vascular cambia and secondary growth.* New Phytol, 2010. **186**(3): p. 577-92.
8. Pace, M.R., L.G. Lohmann, and V. Angyalossy, *The rise and evolution of the cambial variant in Bignonieae (Bignoniaceae).* Evol Dev, 2009. **11**(5): p. 465-79.
9. Hong, L., et al., *Heterogeneity and Robustness in Plant Morphogenesis: From Cells to Organs.* Annu Rev Plant Biol, 2018. **69**: p. 469-495.
10. Merks, R.M.H. and J.A. Glazier, *A cell-centered approach to developmental biology.* Physica A: Statistical Mechanics and its Applications, 2005. **352**(1): p. 113-130.
11. Willis, L., et al., *Cell size and growth regulation in the Arabidopsis thaliana apical stem cell niche.* PNAS, 2016: p. E8238-E8246.
12. Sapala, A., et al., *Why plants make puzzle cells, and how their shape emerges.* Elife, 2018. **7**.
13. Greb, T. and J.U. Lohmann, *Plant Stem Cells.* Curr Biol, 2016. **26**(17): p. R816-21.
14. Lebovka, I., et al., *Computational modelling of cambium activity provides a regulatory framework for simulating radial plant growth.* bioRxiv, 2020.
15. Ragni, L. and T. Greb, *Secondary growth as a determinant of plant shape and form.* Semin Cell Dev Biol, 2017.
16. Wang, N., et al., *Organ-specific genetic interactions between paralogues of the PXY and ER receptor kinases enforce radial patterning in Arabidopsis vascular tissue.* Development, 2019.
17. Fischer, U., et al., *The Dynamics of Cambial Stem Cell Activity.* Annu Rev Plant Biol, 2019. **70**: p. 293-319.
18. Kierzkowski, D., et al., *A Growth-Based Framework for Leaf Shape Development and Diversity.* Cell, 2019.
19. Lopez-Salmeron, V., et al., *The Phloem as a Mediator of Plant Growth Plasticity.* Curr Biol, 2019. **29**(5): p. R173-R181.
20. Gerttula, S., et al., *Transcriptional and Hormonal Regulation of Gravitropism of Woody Stems in Populus.* Plant Cell, 2015. **27**(10): p. 2800-13.
21. Anderson, C.T. and J.J. Kieber, *Dynamic Construction, Perception, and Remodeling of Plant Cell Walls.* Annu Rev Plant Biol, 2020. **71**: p. 39-69.
22. Lucas, W.J. and J.Y. Lee, *Plasmodesmata as a supracellular control network in plants.* Nat Rev Mol Cell Biol, 2004. **5**(9): p. 712-26.
23. Kamon, E. and M. Ohtani, *Xylem vessel cell differentiation: A best model for new integrative cell biology?* Curr Opin Plant Biol, 2021. **64**: p. 102135.
24. Peaucelle, A., R. Wightman, and H. Hofte, *The Control of Growth Symmetry Breaking in the Arabidopsis Hypocotyl.* Curr Biol, 2015. **25**(13): p. 1746-52.

25. Ramakrishna, P., et al., *EXPANSIN A1-mediated radial swelling of pericycle cells positions anticlinal cell divisions during lateral root initiation.* Proc Natl Acad Sci U S A, 2019. **116**(17): p. 8597-8602.
26. Wolf, S. and S. Greiner, *Growth control by cell wall pectins.* Protoplasma, 2012. **249 Suppl 2**: p. S169-75.
27. Senechal, F., et al., *Homogalacturonan-modifying enzymes: structure, expression, and roles in plants.* J Exp Bot, 2014. **65**(18): p. 5125-60.
28. Meents, M.J., Y. Watanabe, and A.L. Samuels, *The cell biology of secondary cell wall biosynthesis.* Ann Bot, 2018. **121**(6): p. 1107-1125.
29. Gorshkova, T., et al., *Plant 'muscles': fibers with a tertiary cell wall.* New Phytol, 2018. **218**(1): p. 66-72.
30. Zhu, Q., et al., *A MAPK cascade downstream of IDA-HAE/HSL2 ligand-receptor pair in lateral root emergence.* Nat Plants, 2019. **5**(4): p. 414-423.
31. Shi, D., et al., *Bifacial cambium stem cells generate xylem and phloem during radial plant growth.* Development, 2019. **146**(1).
32. Wunderling, A., et al., *A molecular framework to study periderm formation in Arabidopsis.* New Phytol, 2018.
33. Schurholz, A.K., et al., *A Comprehensive Toolkit for Inducible, Cell Type-Specific Gene Expression in Arabidopsis.* Plant Physiol, 2018. **178**(1): p. 40-53.
34. Shi, D., et al., *Tissue-specific transcriptome profiling of the Arabidopsis inflorescence stem reveals local cellular signatures.* Plant Cell, 2021. **33**(2): p. 200-223.
35. Barbier de Reuille, P., et al., *MorphoGraphX: A platform for quantifying morphogenesis in 4D.* Elife, 2015. **4**: p. 05864.
36. Berg, S., et al., *ilastik: interactive machine learning for (bio)image analysis.* Nat Methods, 2019. **16**(12): p. 1226-1232.
37. Wolny, A., et al., *Accurate and versatile 3D segmentation of plant tissues at cellular resolution.* Elife, 2020. **9**.
38. Bagdassarian, K.S., et al., *Versatile method for quantifying and analyzing morphological differences in experimentally obtained images.* Plant Signal Behav, 2020. **15**(1): p. 1693092.
39. Pound, M.P., et al., *CellSeT: novel software to extract and analyze structured networks of plant cells from confocal images.* Plant Cell, 2012. **24**(4): p. 1353-61.
40. Jackson, M.D.B., et al., *Global Topological Order Emerges through Local Mechanical Control of Cell Divisions in the Arabidopsis Shoot Apical Meristem.* Cell Systems, 2019.
41. Wunderling, A., et al., *Novel tools for quantifying secondary growth.* J Exp Bot, 2017. **68**(1): p. 89-95.
42. Etchells, J.P., et al., *A brief history of the TDIF-PXY signalling module: balancing meristem identity and differentiation during vascular development.* New Phytol, 2016. **209**(2): p. 474-84.
43. Fisher, K. and S. Turner, *PXY, a Receptor-like Kinase Essential for Maintaining Polarity during Plant Vascular-Tissue Development.* Curr Biol, 2007. **17**(12): p. 1061-6.
44. Ursache, R., et al., *A protocol for combining fluorescent proteins with histological stains for diverse cell wall components.* Plant J, 2018. **93**(2): p. 399-412.
45. Montenegro-Johnson, T.D., et al., *Digital Single-Cell Analysis of Plant Organ Development Using 3DCellAtlas.* Plant Cell, 2015. **27**(4): p. 1018-33.

46. Jackson, M.D., et al., *Topological analysis of multicellular complexity in the plant hypocotyl.* Elife, 2017. **6**.
47. Sankar, M., et al., *Automated quantitative histology reveals vascular morphodynamics during Arabidopsis hypocotyl secondary growth.* Elife, 2014. **3**: p. e01567.
48. Smetana, O., et al., *High levels of auxin signalling define the stem-cell organizer of the vascular cambium.* Nature, 2019. **565**(7740): p. 485-489.
49. Gursanscky, N.R., et al., *MOL1 is required for cambium homeostasis in Arabidopsis.* Plant J, 2016. **86**(3): p. 210-20.
50. Long, Y., et al., *Cellular Heterogeneity in Pressure and Growth Emerges from Tissue Topology and Geometry.* Curr Biol, 2020.
51. Aalen, R.B., et al., *IDA: a peptide ligand regulating cell separation processes in Arabidopsis.* J Exp Bot, 2013. **64**(17): p. 5253-61.
52. Mitsuda, N., et al., *NAC transcription factors, NST1 and NST3, are key regulators of the formation of secondary walls in woody tissues of Arabidopsis.* Plant Cell, 2007. **19**(1): p. 270-280.
53. Bonke, M., et al., *APL regulates vascular tissue identity in Arabidopsis.* Nature, 2003. **426**(6963): p. 181-186.
54. Larson, P.R., *The vascular cambium: development and structure*. Springer Series in Wood Science, ed. T.E. Timell. 1994, Berlin: Springer-Verlag.
55. Antonacci, G., et al., *Recent progress and current opinions in Brillouin microscopy for life science applications.* Biophys Rev, 2020. **12**(3): p. 615-624.
56. Landrein, B. and G. Ingram, *Connected through the force: mechanical signals in plant development.* J Exp Bot, 2019. **70**(14): p. 3507-3519.
57. Trinh, D.C., et al., *How Mechanical Forces Shape Plant Organs.* Curr Biol, 2021. **31**(3): p. R143-R159.
58. Hall, H.C., et al., *Precision Automation of Cell Type Classification and Sub-Cellular Fluorescence Quantification from Laser Scanning Confocal Images.* Front Plant Sci, 2016. **7**: p. 119.
59. Bergstra, J., D. Yamins, and D.D. Cox, *Making a Science of Model Search: Hyperparameter Optimization in Hundreds of Dimensions for Vision Architectures.* Proceedings of the 30 th International Conference on Machine Learning, 2013. **28**.
60. Turing, A.M., *The Chemical Basis of Morphogenesis.* Philosophical Transactions of the Royal Society of London. Series B, Biological Sciences, 1952. **237**(641): p. 37-72.
61. Wolpert, L., *Positional information and the Spatial Pattern of Cellular Differentiation.* J. Theoret. BIol., 1969. **25**: p. 1-47.
62. Green, J.B. and J. Sharpe, *Positional information and reaction-diffusion: two big ideas in developmental biology combine.* Development, 2015. **142**(7): p. 1203-11.
63. Shi, D., et al., *Bifacial stem cell niches in fish and plants.* Curr Opin Genet Dev, 2017. **45**: p. 28-33.